Astronomy Reports, Vol. 45, No. 5, 2001, pp. 331–338. Translated from Astronomicheskiĭ Zhurnal, Vol. 78, No. 5, 2001, pp. 387–395.

Mapping of Bipolar Outflows and Methanol Masers in the CS(2–1) Line

G. M. Larionov, V. G. Promyslov, and I. E. Val'tts

Astro Space Center, Lebedev Institute of Physics, Russian Academy of Sciences, Profsoyuznaya ul. 84/32, Moscow, 117810 Russia

Received July 3, 2000

Abstract—Eighteen regions (bipolar outflows and methanol masers) are mapped in the CS(2–1) line using the 20-m Onsala radio telescope. The coordinates of the CS emission peaks are refined. The sizes and masses of dense regions are estimated for 13 maps. Measurement of the angular sizes of regions of emission indicates that all the sources were resolved by the Onsala radio telescope. The lower limit for the linear dimensions of the CS condensations studied is 0.2–2.1 pc. The hydrogen densities and masses of the CS condensations are estimated to be $n(H_2) = (0.3–13.1) \times 10^4$ cm^{-3} and ($M \approx 7–2800 M_\odot$). Methanol masers are associated with denser and more massive regions, whether or not the maser condensation is connected with a bipolar outflow. © *2001 MAIK "Nauka/Interperiodica".*

1. INTRODUCTION

Physical parameters of interstellar matter derived from astronomical observations play a major role in modeling star formation regions. The improvement of these parameters enables the creation of more accurate scenarios for important physical phenomena accompanying star-forming processes, such as pumping of cosmic masers.

In collisional pumping models, the density of the matter is of primary importance. If the emission source is point-like, the density of the radiating material can be obtained directly from the observed intensities of molecular lines using appropriate formulas. However, most probably only the maser condensations themselves are point-like. The surrounding material, whose density can directly affect the maser pumping, is usually concentrated in some volume larger than that of the maser condensation. We can estimate the density of the matter surrounding a maser only if we know the actual size of the region in which the maser is embedded.

The formation of dense condensations that produce masers can be affected by dynamic processes in the interstellar medium, e.g., the powerful outflows of material (bipolar outflows) that accompany the birth of young stellar objects. It has been shown that bipolar outflows can lead to enhanced methanol maser [1–3] and thermal methanol emission [4].

The lines of the CS molecule are good tracers of the density of the gas surrounding maser condensations. The CS molecule is not excited in low-density gas, since its activation requires densities $n(H_2) \sim 10^4$–10^7 cm^{-3}. In 1995, we carried out a survey of a sample of bipolar outflows and Class I and II methanol masers (158 sources) in the CS(2–1) line; we observed part of this sample in the $C^{34}S$(2–1) line on the 20-m Onsala radio telescope [5]. At the same time, we mapped the sources that were brightest in the CS(2–1) line (>20 Jy km/s).

In the current paper, we report the results of our mapping and estimation of the sizes, densities, and masses of the gas at the centers of the bipolar outflows and in methanol maser condensations that are and are not associated with bipolar outflows. The purpose of this work is to use the estimated densities and masses to search for indications of possible connections between bipolar outflows and the regions in which the masers form.

2. OBSERVATIONS

The observations were carried out in May 1995 on the 20-m radio telescope in Onsala (Sweden). The beamwidth at 98 GHz is 39″. The antenna surface accuracy is 0.128 mm. The antenna surface efficiency at 98 GHz is (47 ± 3)%. The pointing accuracy is 3″ in azimuth and elevation. The observations were carried out in a frequency-switching regime with a frequency offset of 12 MHz. The frequency for the CS(2–1) transition, 97 980.968 MHz, was taken from [6]. We used a receiver with a cooled SIS mixer manufactured in the Institute of Radio Engineering and Electronics (Moscow) [7]. The system temperature ranged from 100 to 500 K, depending on the weather conditions and source elevation. The spectrometer had 256 channels; the bandwidth was 64 MHz and the resolution 250 kHz (0.7 km/s at 98 GHz). An antenna temperature T_A^* of 1 K corresponds to 18.7 Jy. We calibrated the data using the standard method of Kutner and Ulich [8].

1063-7729/01/4505-0331$21.00

Table 1. Sources with the CS(2–1) peak within the map

Source	R.A. (1950)	Δα	Dec. (1950)	Δδ	Source type
NGC 281–W	$00^h49^m27\overset{s}{.}8$	−1″	56°17′28″	0″	MMII, BO
IC 1805–W	02 25 14.5	−26	61 20 10	5	BO
S231	05 35 51.3	−25	35 44 16	−5	MMI, MMII
AFGL 5180	06 05 53.9	−35	21 38 57	0	BO
S254–258	06 09 57.9	−8	18 00 12	−10	MMII, BO
W48	18 59 13.8	−30	01 09 20	−30	MMII
G45.07 + 0.13	19 11 00.4	2	10 45 43	2	MMII
W75–N	20 36 51.1	−23	42 27 20	−19	MMI, MMII, BO
V645–Cyg	21 38 11.3	−1	50 00 45	6	BO
EL1–12	21 45 26.8	−22	47 18 08	−3	BO
L1204A	22 19 50.7	−24	63 36 33	6	BO
L1204B	22 19 55.7	−5	63 22 12	−4	BO
L1203	22 26 46.7	30	62 44 22	−16	BO

Table lists the map center coordinates, their corrections for the CS(2–1) peak position, and source types (BO: bipolar outflow, MMI and MMII: type I and type II methanol masers).

3. RESULTS

We have mapped 18 regions (bipolar outflows and Class I and II methanol masers) in the CS(2–1) line. The mapping was done at nine positions (3 × 3) separated by 39″, and the mapped region covered an area of ~2′ × 2′. Table 1 lists the sources whose emission peaks are in the region studied. The columns give the (1) source name; (2) and (4) position of the map center; (3) and (5) corrections to the coordinates, corresponding to the real position of the CS(2–1) emission peak; and (6) source type (BO: bipolar outflow, MMI: Class I methanol maser, MMII: Class II methanol maser). The maps of five sources (Table 2) showed their emission peaks to be outside the nine positions studied. Figure 1 presents the offset spectra. The spectra were processed using the CLASS package; the figures were plotted using the GREG graphics package. In some cases, we analyzed the maps using the maximum-entropy method. We derived the angular sizes of the emission regions (Table 3).

Table 2. Sources with the CS(2–1) peak outside the map

Source	R.A. (1950)	Dec. (1950)
S255	$06^h10^m01\overset{s}{.}0$	18°00′44″
NGC 2264(IR)	06 38 28.0	09 32 12
18497 + 0022	18 49 46.9	00 22 07
S140–N	22 17 51.1	63 17 50
L1211	22 45 23.3	61 46 07

4. MAXIMUM-ENTROPY METHOD

4.1. Theoretical Foundations for the Maximum-Entropy Method

In radio astronomy, the imaging process can be formulated as the problem of reconstructing the true image from the observed (so-called "dirty") image, which is the convolution of the true image with the beam in the presence of additive noise. In symbolic form,

$$g = f \otimes h + e, \tag{1}$$

where g is the dirty map, f the true image, $\otimes$ the convolution operator, h the beam, and e the additive Gaussian noise associated with the observation.

The problem of reconstructing the true image f from the observed dirty image g is ill-posed, since the presence of zero points in the beam and of noise results in the existence of a multitude of solutions [9]. To remove the ambiguity in the solution, we must make use of additional information. The maximum-entropy criterion removes the ill-posed nature of the image reconstruction, and ensures the uniqueness of the solution [9]. The maximum-entropy method (MEM) was proposed by Jaynes [10] in 1957; its application to radio astronomy was described by Burg [11]. Let us give a brief description of this method (a similar formulation is given by Wilczek *et al.* [12]).

Entropy is a measure of the indeterminacy associated with the occurrence of some event. In problems of image restoration, we use the fact [13] that the entropy

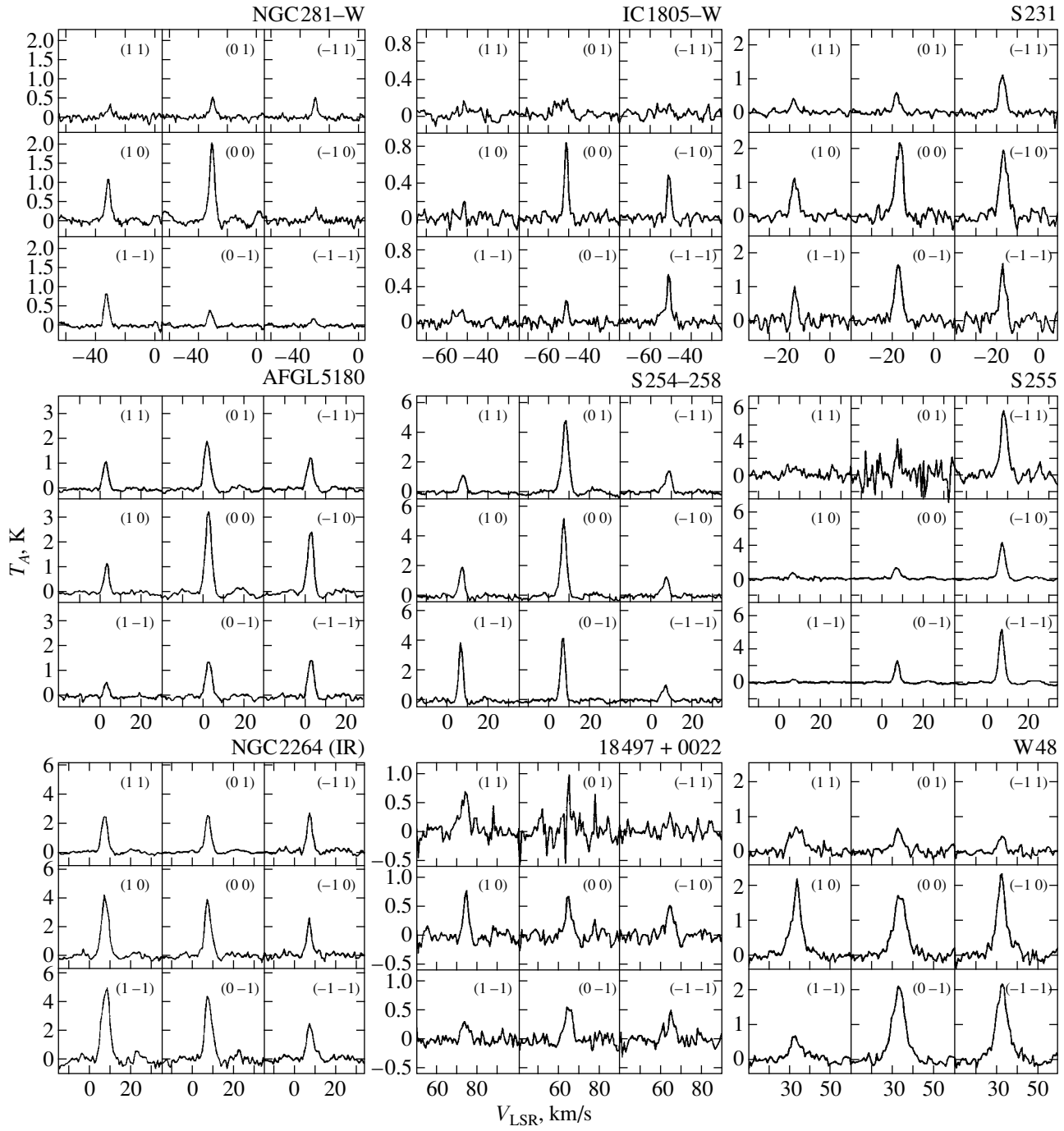

Fig. 1. Offset spectra for the sources observed.

$E(f)$ of a Gaussian process with zero mean is proportional to

$$E(f) \sim -\sum_{i=1}^{N} f_i \log f_i. \quad (2)$$

Here and below, a subscript denotes an element of a database, and N is the number of image pixels.

MEM is based on searching, among all possible radio brightness distributions, for the distribution f that maximizes the entropy (2) under the following restrictions on the image-formation process:

$$\sum_{i=1}^{N} f_i = \gamma, \quad (3)$$

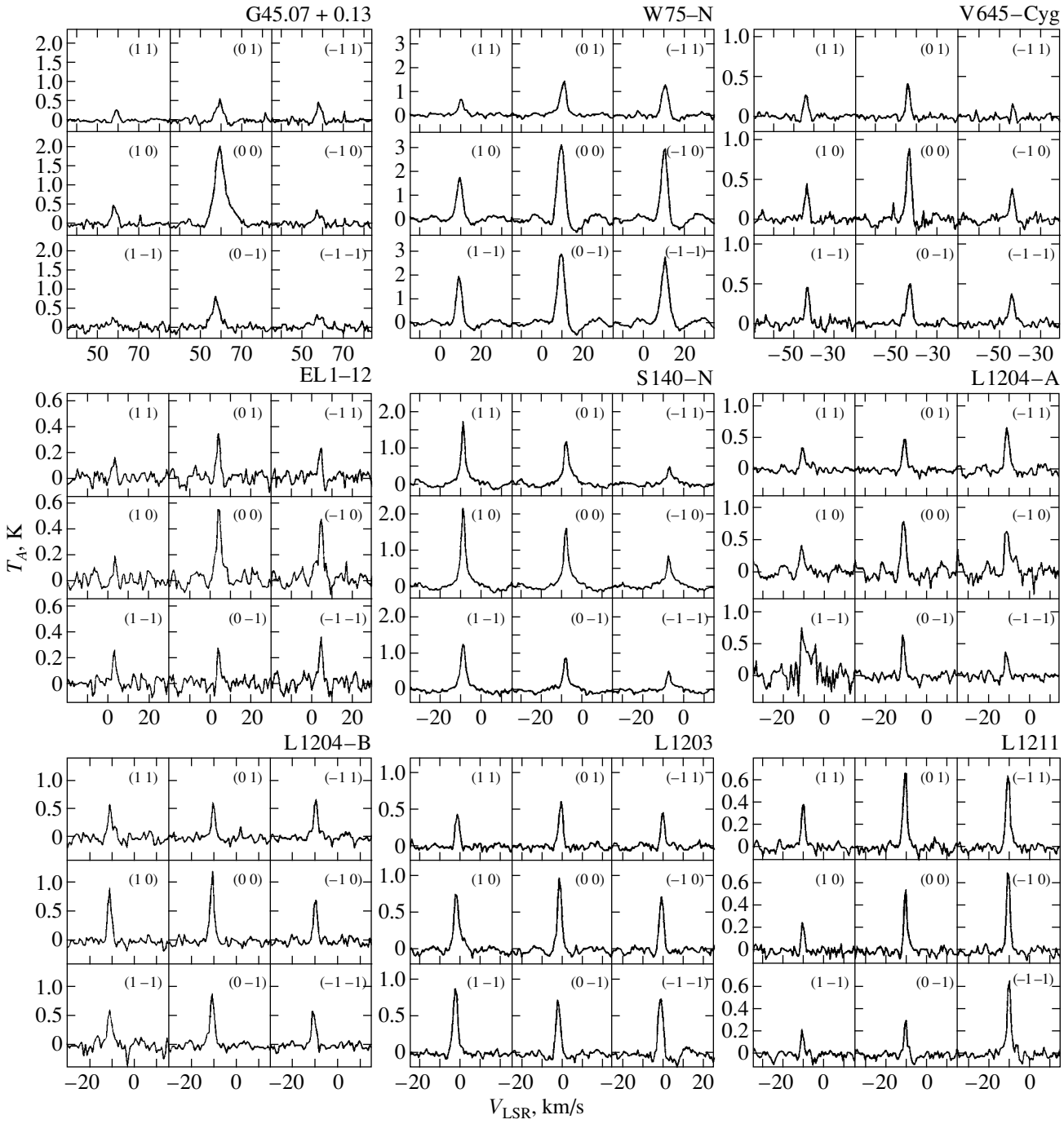

Fig. 1. (Contd.)

$$g_k + e_k = \sum_{i=1}^{N} h_{ik} f_i, \quad (4)$$

$$\sum_{k \in A} \frac{e_k^2}{\sigma_k^2} = \Omega, \quad (5)$$

where γ is the integrated flux, Ω the confidence level according to the χ^2 test, and A the domain on which the observational data are defined.

Formula (3) restricts the integrated flux in the restored image based on the integrated flux of an initial image; (4) determines the proximity of the restored and observed data in amplitude; and (5) means that the power of the error in the reconstruction and the power of the observational noise are consistent with the chi-squared criterion.

Physically, MEM is a search for the radio brightness distribution that forms the observed dirty map g under

Table 3. Source sizes, densities, and masses estimated from dirty and MEM maps (marked with asterisks)

Source	θ	*d*, kpc	*l*, pc	$n_{(H_2)}$, 10^4 cm^{-3}	*M*, $M_\odot$
NGC 281–W	70.″3 ± 24.″6	2.1	0.72 ± 0.26	4.3	≥550
IC 1805–W*	50.2 ± 14.2	2.3	0.56 ± 0.13	1.0	≥65
S231*	81.3 ± 21.4	1.8	0.71 ± 0.31	3.9	≥540
AFGL 5180*	69.8 ± 47.2	1.5	0.51 ± 0.24	3.7	≥200
S254–258	84.9 ± 33.8	2.5	1.03 ± 0.46	2.7	≥1030
G45.07 + 0.13	49.4 ± 21.2	8.3	1.99 ± 1.31	1.0	≥2800
W48*	53.1 ± 24.3	3.2	0.77 ± 0.28	13.1	≥2112
W75–N*	55.5 ± 40.8	2.0	0.54 ± 0.42	5.2	≥280
V645–Cyg	73.5 ± 42.0	6.0	2.14 ± 1.19	0.5	≥1710
EL1–12*	46.7 ± 23.5	0.9	0.20 ± 0.08	2.2	≥7
L1204–A*	143 ± 64.2	0.9	0.62 ± 0.26	0.3	≥29
L1204–B*	104 ± 42.3	0.9	0.45 ± 0.22	0.8	≥23
L1203*	123 ± 39.4	0.9	0.54 ± 0.24	1.6	≥90

the specified conditions for formation of the image; in this sense, MEM can be considered a maximum-likelihood method [9].

With (3)–(5), maximizing (2) using the Lagrange method yields the following relationship for the desired radio brightness distribution:

$$f = N\exp\lambda(h \otimes g - h \otimes h \otimes f), \quad (6)$$

where λ is a parameter of the reconstruction.

The statistical properties of MEM and the properties of maps restored using MEM have been considered in many works; the most complete review can be found in [14]. This method is most effective if the image contains compact sources embedded in a uniform background. The exponential dependence of *f* guarantees the non-negativity of the radio brightness solution. The functional (6) is essentially non-linear and—by virtue of this non-linearity—improves the map resolution in comparison with the dirty map [9]. The restored image can contain spatial frequencies that are absent in the dirty-map spectrum. We consider the results of [15] to be typical: MEM image processing yielded a resolution of about 20″ with a 45″ beam for the bipolar outflow L1551; i.e., about a factor of two improvement.

4.2. Image Reconstruction

We processed the initial (dirty) maps of nine sources using MEM, obtaining maps with somewhat higher resolution than that corresponding to the telescope beam. These maps are presented in Fig. 2. We used the iterative MEM algorithm of Promyslov [16] to optimize the non-linear equation (6). For the strongest features in the spectra, the effective beamwidth obtained using MEM was about 30″, whereas the radio telescope beamwidth was 39″. These MEM images are more reliable for derivation of the source parameters.

5. DATA ANALYSIS

5.1. Density of Material Emitting in the CS Line

We calculated the projected linear dimensions of the regions of CS emission from their angular sizes (derived from the maps) and the distances of the sources. The density of the condensations can be calculated as

$$n(H_2) = N(H_2)/l, \quad (7)$$

where *l* is the size of the emitting region and $N(H_2) = \frac{X(H_2)N(CS)}{X(CS)}$ is the column density of molecular hydrogen. We used the values of *N*(CS) found in our survey [5]. The ratio $X(CS)/X(H_2) = 4 \times 10^{-9}$ was taken from [17].

If we know the density in the emission region, we can find its mass

$$M = \mu m V n(H_2), \quad (8)$$

where *m* is the mass of an H_2 molecule, $\mu \approx 1.36$ is the ratio of the total gas mass to that of H_2, and $V = (1/6)\pi l^3$ is the volume of the emission region. Table 3 lists the results of these calculations. The columns give the (1) source name, (2) distance (taken from [18]; the distance to G45.07 + 0.13 was taken from [5], and that to W48 from [19]), (3) angular size of the region, (4) diameter of the CS-emission region, (5) H_2 density, and (6) mass of the CS condensation. Asterisks denote sources with MEM maps.

5.2. Comments for Individual Sources

NGC 281–W. This source is a bipolar outflow [18, 20] and Class II methanol maser [21], whose velocity coincides with the velocity of the center of the bipolar flow. The source IRAS 00494 + 5617 is observed in the direc-

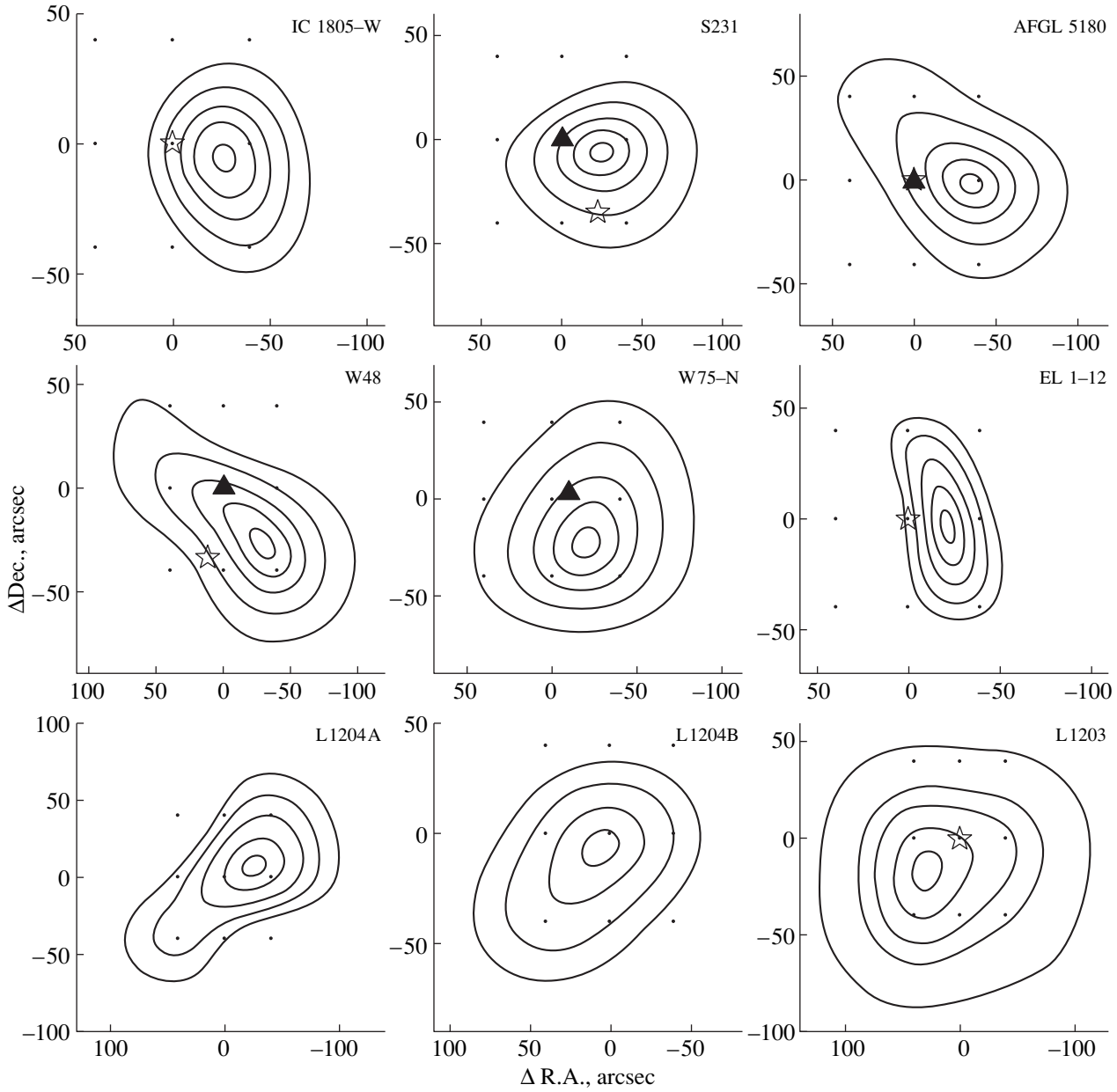

Fig. 2. MEM maps of IC 1805–W, S231, AFGL 5180, W48, W75N, EL 1–12, L1204–A, L1204–B, and L1203 in the CS(2–1) line. Contours are drawn at levels of 10, 25, 50, 75, and 90%. The asterisks show IRAS sources, and the triangles methanol masers (MMI and MMII).

tion of this object. According to [22], the mass of the cloud emitting the CS(2–1) line is $210M_\odot$. We estimate its mass to be $M \geq 550M_\odot$.

IC 1805–W. This source is a bipolar outflow [18]. The source IRAS 02252 + 6120 is observed at the same position (Fig. 2). The source was earlier observed in the CS(2–1) line by Larionov *et al.* [5]. We estimate the mass to be $M \geq 65M_\odot$.

S231. This source is known as a Class I methanol maser at 44 GHz [23] and strong Class II maser at 6.7 GHz [24]. The region contains the source IRAS 05358 + 3543 (Fig. 2). S231 was studied in the CS(2–1) line by Plume *et al.* [25], but was not mapped. We estimate the mass to be $M \geq 540M_\odot$.

AFGL 5180. This source is a bipolar outflow [26] and Class II methanol maser [21]. The region of IRAS 06058 + 2138, which is associated with AFGL 5180, was mapped earlier in the CS(2–1) line by Carpenter *et al.* [22] (Fig. 2), who derived a mass for the cloud emitting in the CS(2–1) line of $M = 270M_\odot$. We estimate this mass to be $M \geq 220M_\odot$.

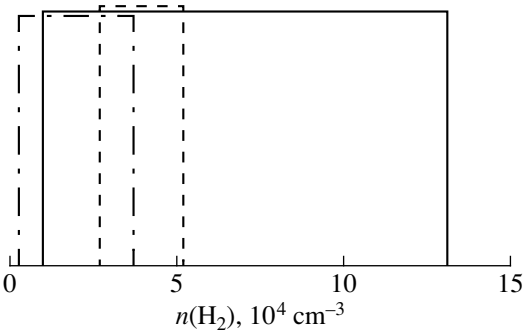

Fig. 3. Density distributions at bipolar-flow centers (dot–dash curve) in condensations containing methanol masers that are (dashed) and are not (solid) associated with bipolar outflows.

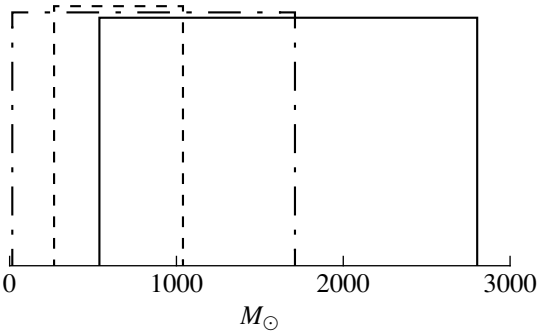

Fig. 4. Mass distribution in the regions around the bipolar-flow centers (dot–dash curve) in condensations containing methanol masers that are (dashed) and are not (solid) associated with bipolar outflows.

S254–258. A Class II methanol maser is observed at the position of S254–258, offset by $\Delta\delta = 30''$ [27]. The bipolar outflow S255 was studied in the CS(2–1) line by Zinchenko *et al.* [28], who derived the cloud size l = 2.2 pc, density of the region emitting in the CS(2–1) line $n(H_2) \approx 10^4$ cm^{-3}, and mass $M = 4270M_\odot$. The region was also studied in the CS(2–1) line by Carpenter *et al.* [29], who obtained a cloud mass of $M = 840M_\odot$. We find $l = 1.03$ pc, $n(H_2) = 2.7 \times 10^4$ cm^{-3}, and $M \geq 1050M_\odot$.

G45.07 + 0.13. This source is a faint Class II methanol maser [25]. The source IRAS 19110 + 1045 is observed at the same position. The region was mapped earlier in the CS(2–1) line by Hunter *et al.* [30], but no estimates of the density or mass were made. We estimate the mass to be $M \geq 2800M_\odot$.

W48. This source is a Class II methanol maser at 6.7 GHz [24]. The source IRAS 18592 + 0108 is observed at the same position (Fig. 2). We estimate the mass to be $M \geq 283M_\odot$.

W75N. This is one of the brightest methanol masers of Class I [2] and Class II [24], and simultaneously a bipolar outflow [31] (Fig. 2). We estimate the mass to be $M \geq 283M_\odot$.

V645–Cyg. This source is a bipolar outflow [18, 32]. The source IRAS 21381 + 5000 is observed at the same position. V645–Cyg was observed earlier in the CS(2–1) line by Larionov *et al.* [5]. We estimate the mass to be $M \geq 540M_\odot$.

EL1–12. This region is known as a bipolar outflow [33]. The source IRAS 21454 + 4718 is observed at the same position (Fig. 2). EL1–12 was observed earlier in the CS(2–1) line by Larionov *et al.* [5]. We estimate the mass to be $M \geq 7M_\odot$.

L1204–A, L1204–B. These sources are bipolar outflows [34] (Fig. 2). We estimate the masses for L1204–A and L1204–B to be $M \geq 13M_\odot$ and $M \geq 29M_\odot$, respectively.

L1203. This source is a bipolar outflow [18]. The source IRAS 22267 + 6244 is observed at the same position (Fig. 2). L1203 was observed earlier in the CS(2–1) line by Larionov *et al.* [5]. We estimate the mass to be $M \geq 90M_\odot$.

5.3. Discussion

Figure 3 shows the density distributions at the centers of bipolar outflows (dot–dash curve) in condensations containing methanol masers that are (dashed) and are not (solid) associated with bipolar outflows. We can see that methanol masers are observed in a rather wide range of densities, regardless of the presence of a bipolar outflow in the region. On the other hand, methanol masers are detected only in denser bipolar outflows.

Figure 4 presents the mass distributions in the regions around the bipolar-flow centers (dot–dash curve) in condensations containing methanol masers that are (dashed) and are not (solid) associated with bipolar outflows. The probability of methanol maser detection is higher in more massive regions.

6. CONCLUSIONS

(1) We have constructed nine-point maps of 18 regions (bipolar outflows and regions hosting methanol masers) in the CS(2–1) line.

(2) For 13 sources, the CS emission peak was within the region studied. For five sources, mapping showed the cloud center to be outside the region studied.

(3) Eight maps could be processed using the maximum-entropy method.

(4) We have refined the positions of the peaks of the CS condensations in the CS(2–1) line.

(5) All the sources were resolved to the beam of the Onsala radio telescope (39″).

(6) Our estimated linear dimensions for the emission regions (0.20–2.14 pc) proved to be typical for CS condensations.

(7) Our estimated densities of molecular hydrogen $n(H_2)$ are in the range $(0.3–13.1) \times 10^4$ cm^{-3}.

(8) The estimated masses M of the condensations are $\approx 7–2800 M_\odot$.

(9) There is some indication that methanol masers are associated with denser and more massive regions, regardless of whether the maser condensation is connected with a bipolar outflow.

ACKNOWLEDGMENTS

This work was supported in part by the Russian Foundation for Basic Research (project no. 98-02-16) and the INTAS (project no. 97-1451).

REFERENCES

1. R. L. Plambeck and K. M. Menten, Astrophys. J. **364**, 555 (1990).
2. A. D. Haschick, K. M. Menten, and W. A. Baan, Astrophys. J. **354**, 556 (1990).
3. S. V. Kalenskiĭ, R. Bachiller, I. I. Berulis, *et al.*, Astron. Zh. **69**, 1002 (1992) [Sov. Astron. **36**, 517 (1992)].
4. R. Bachiller, S. Liechti, C. M. Walmsley, and F. Colomer, Astron. Astrophys. **295**, L51 (1995).
5. G. M. Larionov, I. E. Val'tts, A. Winnberg, *et al.*, Astron. Astrophys., Suppl. Ser. **139**, 257 (1999).
6. F. J. Lovas, J. Phys. Chem. Ref. Data **21**, 181 (1992).
7. S. V. Shitov, V. P. Koshelets, S. A. Kovtonyuk, *et al.*, Supercond. Sci. Technol. **4**, 406 (1991).
8. M. L. Kutner and B. L. Ulich, Astrophys. J. **250**, 341 (1981).
9. B. R. Levin, *Theoretical Foundations of Statistical Radio Engineering* [in Russian] (Radio i Svyaz', Moscow, 1989).
10. E. T. Jaynes, Proc. IEEE **70**, 952 (1982).
11. J. Burg, PhD Thesis (Stanford Univ., 1975).
12. R. Wilczek and S. Drapatz, Astron. Astrophys. **142**, 9 (1985).
13. S. L. Marple, Jr., *Digital Spectral Analysis with Applications* (Prentice-Hall, Englewood Cliffs, 1987; Mir, Moscow, 1990).
14. R. Narayan and R. Nityanada, Ann. Rev. Astron. Astrophys. **24**, 597 (1986).
15. G. H. Moriarty-Schieven, R. L. Snell, S. E. Strom, *et al.*, Astrophys. J. **319**, 742 (1987).
16. V. G. Promislov, in *Advances in Soft Computing*, Ed. by R. Roy, T. Furuhashi, and P. K. Chawdhry (Physica-Verlag, New York, 1998), p. 421.
17. W. M. Irvine, P. F. Goldsmith, and A. Hjalmarson, in *Interstellar Processes*, Ed. by D. J. Hollenbach and H. A. Thronson (Kluwer, Dordrecht, 1987), p. 561.
18. Y. Fukui, in *Low Mass Star Formation and Pre-Main Sequence Objects*, Ed. by Reipurth (ESO, Garching bei Munchen, 1989), p. 95.
19. D. S. Shepherd and E. Churchwell, Astrophys. J. **472**, 225 (1996).
20. R. L. Snell, R. L. Dickman, and Y. L. Huang, Astrophys. J. **352**, 139 (1990).
21. V. I. Slysh, S. V. Kalenskii, I. E. Val'tts, *et al.*, Astron. Astrophys., Suppl. Ser. **134**, 115 (1999).
22. J. M. Carpenter, R. L. Snell, F. P. Schloerb, and M. F. Skrutskie, Astrophys. J. **407**, 657 (1993).
23. R. Bachiller, J. Cernicharo, J. Martin-Pintado, *et al.*, Astron. Astrophys. **231**, 174 (1990).
24. K. M. Menten, Astrophys. J. **380**, L75 (1991).
25. R. Plume, D. T. Jaffe, N. J. Evans, *et al.*, Astrophys. J. **476**, 730 (1997).
26. R. L. Snell, Y. L. Huang, R. L. Dickman, and M. J. Claussen, Astrophys. J. **325**, 853 (1988).
27. J. L. Caswell, R. A. Vaile, S. P. Ellingsen, *et al.*, Mon. Not. R. Astron. Soc. **272**, 96 (1995).
28. I. Zinchenko, V. Forsstrom, A. Lapinov, and K. Mattila, Astron. Astrophys. **288**, 601 (1994).
29. J. M. Carpenter, R. L. Snell, F. P. Schloerb, and M. F. Skrutskie, Astrophys. J. **450**, 201 (1995).
30. T. R. Hunter, T. G. Phillips, and K. M. Menten, Astrophys. J. **478**, 283 (1997).
31. J. Fisher, D. B. Sanders, M. Simon, and P. M. Solomon, Astrophys. J. **293**, 508 (1985).
32. M. Cohen, Astrophys. J. **215**, 533 (1977).
33. R. M. Levreault, Astrophys. J., Suppl. Ser. **67**, 283 (1988).
34. K. Sugitani and Y. Fukui, in *Star Forming Regions (IAU Symp. 115)*, Ed. by M. Peimbert and Jun Jugaku (Reidel, Dordrecht, 1987), p. 75.

Translated by G. Rudnitskiĭ

Astronomy Reports, Vol. 45, No. 5, 2001, pp. 339–349. Translated from Astronomicheskiĭ Zhurnal, Vol. 78, No. 5, 2001, pp. 396–407.

Variations of the H_2O Maser Emission of W51M in 1981–1998

V. A. Samodurov and S. V. Logvinenko

Pushchino Radio Astronomy Observatory, Astro Space Center, Lebedev Institute of Physics, Pushchino, Moscow oblast, 142292 Russia

Received May 24, 1999

Abstract—The results of spectral monitoring of the maser source W51M carried out in the water-vapor line at 1.35 cm (22GHz) on the 22-m telescope of the Pushchino Radio Astronomy Observatory in 1981–1998 are reported and interpreted. Long-term variations of the maser flux with a period of 12–13 years are found. W51M may be a rotating and simultaneously expanding toroidal cloud of gas and dust around a young star with a mass of the order of ~15$M_\odot$, with numerous high-velocity jets of maser condensations flowing out in two broad cones along the polar axis of the torus. A stellar wind with a velocity of about 2000–3000 km/s is responsible for the maser pumping. © *2001 MAIK "Nauka/Interperiodica".*

1. INTRODUCTION

Regular spectral observations (every one to three months) of a number of sources of maser emission in the water vapor line at 1.35 cm (22 GHz) were carried out on the 22-m radio telescope of the Pushchino Radio Astronomy Observatory (PRAO) in 1981–1998. Among these was the star-forming region W51 Main (W51M), for which we report results here. W51M is located in the W51 molecular-cloud complex [1], which contains numerous IR sources and OH and H_2O masers associated with star-forming regions in the complex [2–6]. W51M has coordinates $\alpha = 19^h21^m26.2^s$, $\delta = +14°24'44''$ [7] (here and below, coordinates are given for epoch 1950.0). There is a component of the molecular cloud W51A at the same position; its center hosts the IR source G49.5–0.4, which coincides with a continuum radio source and compact HII region. The radial velocity of G49.5–0.4 with respect to the LSR determined from the H109α radio recombination line is V = 59.0 km/s [8].

The distance to the maser source W51M is estimated to be 7.0 ± 1.5 kpc [9], based on proper motions of individual H_2O maser condensations. The source was discovered in 1969 [2]. Various individual spectral observations of the source were made, as well as spectral monitoring observations in February 1969–March 1970 [10] and November 1974–September 1976 [11]. Some interferometric results have also been reported [9, 12–15].

2. OBSERVATIONS

Our 1.35-cm observations were made using the 22-m PRAO radio telescope from 1981 to 1998. The antenna beamwidth at 22 GHz is 2.6′. The observations were carried out using an ON–ON method with symmetrical beam switching: the antenna was pointed toward the source first with one horn feed, then with the other. The source signal was determined as the difference between the signals measured by the on-source horn and the horn directed toward a source-free comparison area.

Some of the spectral features of W51M are linearly polarized up to 9% [16], which is typically smaller than the rms error of our observations (which ranges from 10–15% of the flux, due to the different observing conditions in different sessions). Nevertheless, the source was usually observed in the same sky sector, to avoid the polarizations of individual spectral features influencing the signal amplitude.

We performed the spectral analysis of the signal using a 96-channel filter bank with a spectral resolution of 7.5 kHz, or 0.101 km/s per channel. Thus, one 96-channel spectrogram covered 9.7 km/s in radial velocity. In our observations of W51M, several spectrograms were obtained sequentially with a velocity step of 9.7 km/s. Beginning in 1997, the spectrum analyzer was expanded to 128 channels (12.94 km/s).

Taken as a whole, our observations covered a radial-velocity interval of 28–133 km/s, but a substantial fraction of them were carried out in the range 38–106 km/s. There is some uncertainty in the radial-velocity scale. When we compared our results with those of some studies (for example, [4]), we found no discrepancies in the radial velocity of the main spectral peak; however comparison with the results of [2, 12, 16] revealed small systematic differences in the positions of some spectral features. For example, the radial velocities for our spectra are 0.9 ± 0.1 km/s lower than those in [16].

The system noise temperature varied from 180 to 300 K. An antenna temperature of 1 K for a point-like source of unpolarized emission corresponds to a flux of 25 Jy. The signals from both horns were taken in antiphase, and their absolute values added; therefore, to convert the antenna temperature to the flux in Jy, the spectrograms were multiplied by a factor of 12.5. All plots and data presented below are given in Jy.

1063-7729/01/4505-0339$21.00 © 2001 MAIK "Nauka/Interperiodica"

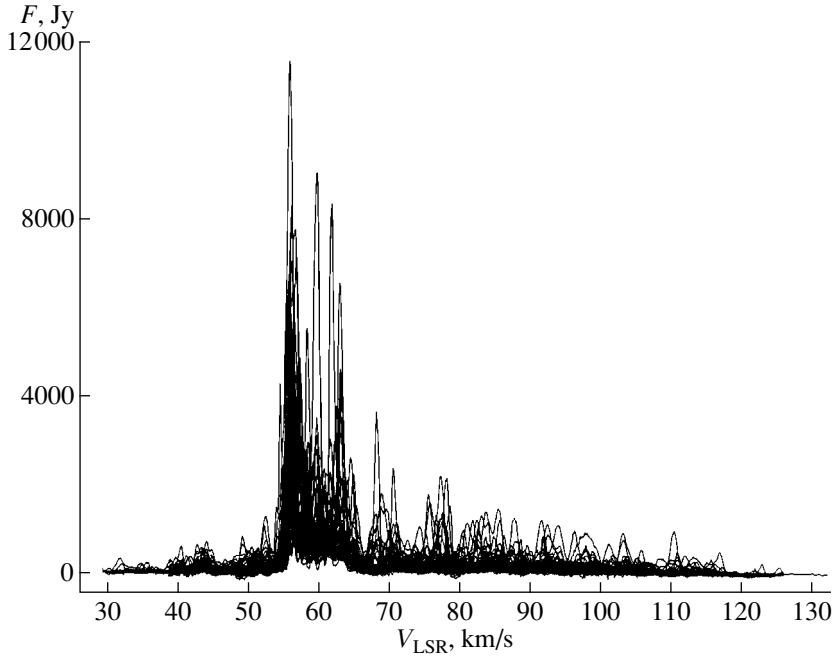

Fig. 1. Homogeneous sample of W51M spectra for 1981–1998, plotted on a single graph.

The spectra were calibrated as follows. Approximately twice a year, under ideal observing conditions (clear weather, low atmospheric humidity and temperature), we observed calibration sources with known fluxes: either planets (Venus and Jupiter, calibrated in accordance with [17, 18]) or the source DR21 (flux 19 Jy; [19]). We also observed a number of maser sources with slowly varying spectra (timescales for significant flux variations exceeding one year). We used the spectra of these maser sources as calibrators under poorer observing conditions, when we were not able to obtain reliable measurements for the primary calibrators (as clouds pass across the telescope beam, the signal can fluctuate by up to 50–100 Jy).

Near W51M, there is another maser source with comparable flux, W51N (or W51 North, with 1950.0 coordinates $\alpha = 19^h21^m22.4^s$, $\delta = +14°25'13.0''$ [7]). Unfortunately, this source falls inside the beam of the 22-m telescope during observations of W51M (the projected distance between the sources is about 1′). However, it is known [12, 20] that the flux of this source constitutes no more than 40–50% of the flux of W51M at radial velocities below 80 km/s. Mader *et al.* [4] detected no significant flux from W51N in comparison with W51M. In addition, the telescope beam was not centered on W51N in our observations. As a result, we estimate that the contribution of W51N at velocities below 80 km/s did not exceed 30% of the total flux; the effect of W51N outside this spectral interval is negligible (judging from the spectra of W51N presented in [12, 20]). There is also evidence (see the spectra of W51N in [20]) that the spectral behavior of W51N is much more stable than that of W51M in the radial-velocity interval observed. Therefore, it is quite possible that all the spectral variations we have observed are associated primarily with the object of our study, W51M. Nevertheless, some features in our spectra are due to W51N, as we discuss below.

3. RESULTS

The observations were carried out no less frequent than every six months. In 1981–1998, about 110 spectrograms were obtained at a mean interval of two months. The results of the observations are presented in electronic form at the web site http://astra.prao.psn.ru/sam/win/w51m.htm. We do not reproduce this multipage figure here, in view of its large volume.

Since the observations were not completely regular (the interval between observations varied from one day to six months), we have compiled a sample of spectra uniformly spread throughout the total observation interval—about 70 spectra in all, with four spectra per year of observations. These are presented in Fig. 1. We used this sample for a statistical analysis of the spectra of W51M.

We used this sample to determine the mean spectrum of W51M (Fig. 2). For the arithmetic mean spectrum, we calculated the radial velocities (with step 0.101 km/s)

$$F_{\text{sum}}(V) = \frac{\sum_{i=1}^{i=N} F_i(V)}{N}, \quad (1)$$

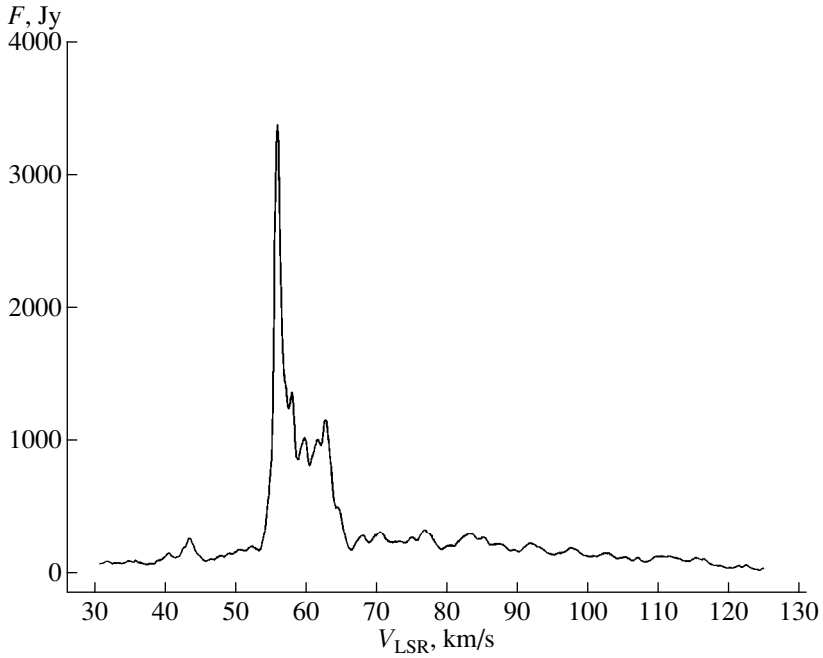

Fig. 2. Mean spectrum of W51M for 1981–1998.

where N is the number of observations at velocity V for the entire time interval 1981–1998.

Analysis of the spectra for this sample and the mean spectrogram reveals zones in the W51M spectrum displaying different behaviors and appearances. First and foremost, the "core" spectrum at velocities 53–66 km/s is evident. This region contains about 60% of the total flux of the spectrum (explaining why many early studies were restricted to this interval [11, 21]).

Based on Figs. 1 and 2, we can approximately divide the observed spectral interval into a number of zones (Table 1). The accuracy of the locations of zone boundaries in radial velocity is ±0.2 km/s. Upon closer inspection, the central zone (53–66 km/s) can be divided into three subintervals: 53–58.5 km/s (the spectral feature dominating the entire spectrum), 58.5–60.2 km/s (long-lived, strong spectral features persisting over several years), and 60.2–66 km/s (persistent groups of spectral lines forming a stable plateau in the spectrum). Note also that division of the spectrum into zones beyond 79 km/s is quite approximate: there are no longer sharp boundaries between spectral zones.

3.1. Comparative Analysis of the Spectra of W51M and W51N

In the Introduction, we noted the problem of isolating the effect of the source W51N in the spectra of W51M. We have developed a technique for separating the two spectra. In several observing sessions, we measured the spectra at the positions of W51M ($\alpha = 19^h21^m26.2^s$, $\delta = +14°24'44''$), W51N ($\alpha = 19^h21^m22.4^s$, $\delta = +14°25'13.0''$), and W51N + a shift in the direction away from W51N by an amount equal to the separation between W51M and W51N ($\alpha = 19^h21^m18.6^s$, $\delta = +14°25'42.0''$). This last point is sufficiently close to W51N for spectral features due to W51N to be rather strong, whereas features due to W51M fall on the steep fall-off of the radio telescope beam, so that their intensity is sharply decreased. As a result, we can readily determine which features are

Table 1. Division of the W51M spectrum into zones according to the spectrum averaged over all years of observations

Interval of V_{LSR}, km/s	Comments
28–37.5	Faint sporadic features
37.5–45	Persistent features
45–53	Usually no strong features
53–66:	
53–58.5	Dominating feature
58.5–60.2	Persistent features
60.2–66	A group of strong persistent features (plateau)
66–72.5	Persistent features
72.5–79	Persistent features
79–90	Transient features
90–95.5	Transient features
95.5–100.5	Transient features
100.5–109	Transient features
109–118.5	Transient features
118.5–126	Faint sporadic features

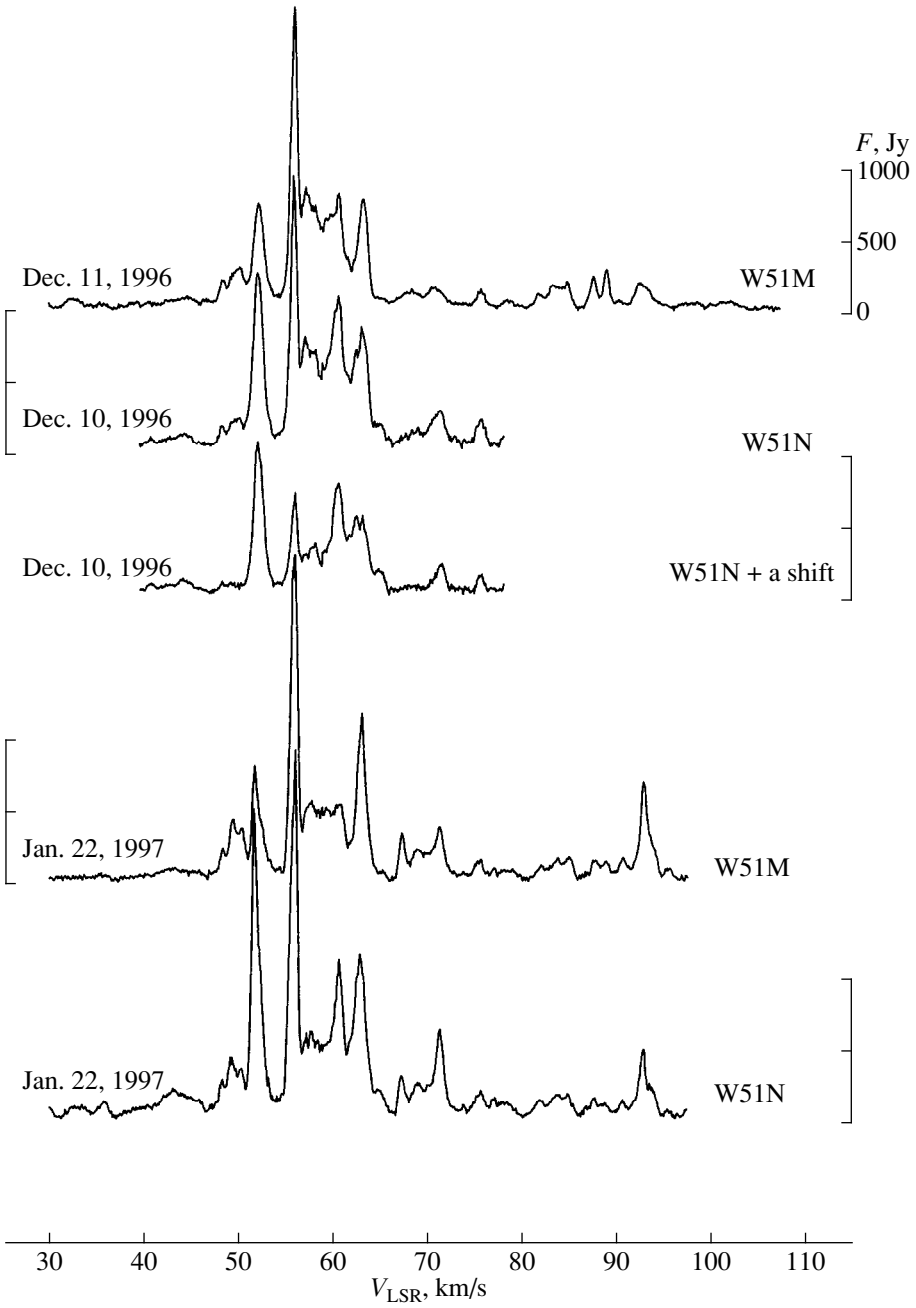

Fig. 3. Comparison of the spectra of W51M, W51N, and a point shifted from W51N by a distance equal to the separation of W51M and W51N (in the direction opposite to W51M); this last spectrum is denoted W51N + a shift.

due to W51M and which to W51N. Figure 3 presents a sample of such observations.

We can see in Fig. 3 find that W51N dominates at <47 km/s while only the effect of W51M is appreciable at >86 km/s. In the remainder of the spectrum, features at 47–52, 53.5–59.5, and 61–70.2 km/s certainly belong to W51M, while features at 52.0–53.5 and 59.5–61 km/s are associated with W51N. W51N probably also dominates at 70.2–86 km/s. Of course, these conclusions are relevant only for the spectra presented in Fig. 3, and the situation may be different at other epochs.

3.2. Analysis of Integrated Flux Variations of W51M in Various Spectral Intervals

We have analyzed the behavior of the total flux in various intervals of the spectrum of W51M. Figure 4 shows these flux variations for the entire spectrum. Since the radial-velocity range can differ from session to session, we give curves for intervals covering a large fraction of the spectrum: 38–115, 38–105, 48–95.5, and 53–66 km/s. It is readily apparent that the behaviors in these intervals are the same on timescales of several years,

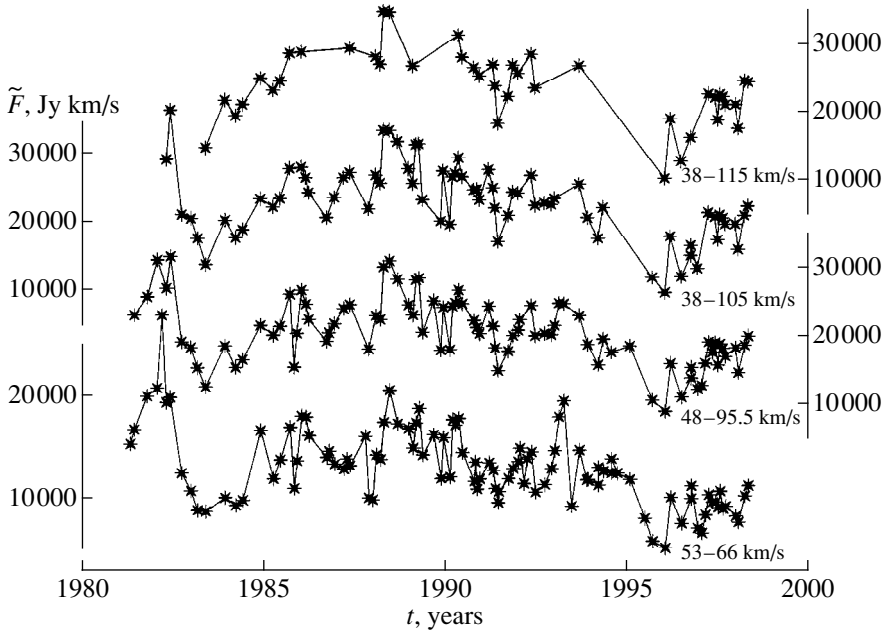

Fig. 4. Variations of the integrated maser flux in spectral intervals covering a large fraction of the entire W51M spectrum: 38–115, 38–105, 48–95.5, and 53–66 km/s.

displaying flux minima in 1983–1984 and 1996 and a flux maximum in about 1989. The total flux for the entire spectrum (39–105 km/s) varied throughout the observation period from $\sim 1.2 \times 10^4$ to $\sim 3.7 \times 10^4$ Jy km/s.

On the whole, the integrated-flux variations are sinusoidal with a period of 12–13 years. The interval 53–66 km/s shows the same behavior and contains about 60–65% of the total flux of W51M.

We now turn to the data presented in [10, 11, 21], which were obtained in nearly the same velocity range, 52–72 km/s. A total flux of 1.5×10^4 Jy km/s is given for 1969–1970 (near the suspected minimum, 1970–1971, according to our data); the total flux is 3.5×10^4 Jy km/s in 1975–1976 (near the suspected maximum, 1976–1977, according to our data) [21]. These data are consistent with a period for the total-flux variations of 12–13 years, as indicated by our data for 1981–1998. The ratio of the 1975–1976 to the 1969–1970 fluxes is 2.33 [21]. The ratio of our fluxes at 53–66 km/s, $\sim 2.0 \times 10^4$ Jy km/s for 1988–1989 and $\sim 0.8 \times 10^4$ Jy km/s for 1983–1984, is 2.5, in good agreement with the data of [21]. Thus, we conclude that the total flux has varied sinusoidally with a period of 12–13 years (with flux minima in 1969–1970, 1983–1984, and 1996); the ratio of the maximum to minimum fluxes is about 2.5. Similar behavior for integrated flux variations has also been found for other sources [22–26].

Let us now consider the flux variations of W51M in individual spectral zones. Detailed analysis shows that the spectrum contains extended zones with similar temporal flux behavior, which differs from those in adjacent zones. One example of such a zone (47.5–52.5 km/s) is shown in Fig. 5. Along with a plot of the flux behavior for the entire interval (lower curve), Fig. 5 shows plots for the consecutive spectral intervals 47.5–48.5, 48.5–49.5, 49.5–50.5, 50.5–51.5, and 51.5–52.5 km/s. We can see

Table 2. Division of the W51M spectrum into zones according to the temporal behavior of the integrated flux in intervals

Interval of V_{LSR}, km/s	Source determining the behavior of the spectral zone
38–40	Probably W51N
40–43	W51N
43.5–47	W51N
47.5–52.5	W51M
53–56	W51M
58–60	W51N
61–66	W51M
66.5–71	W51M
72–75	Not clear whether W51M or W51N
75–78.5	Not clear whether W51M or W51N
80–85.5	W51N
86–92	W51M
92.5–95	W51M
96–99	W51M
100–105	W51M
105–109	W51M
109–112	W51M
112–115	W51M

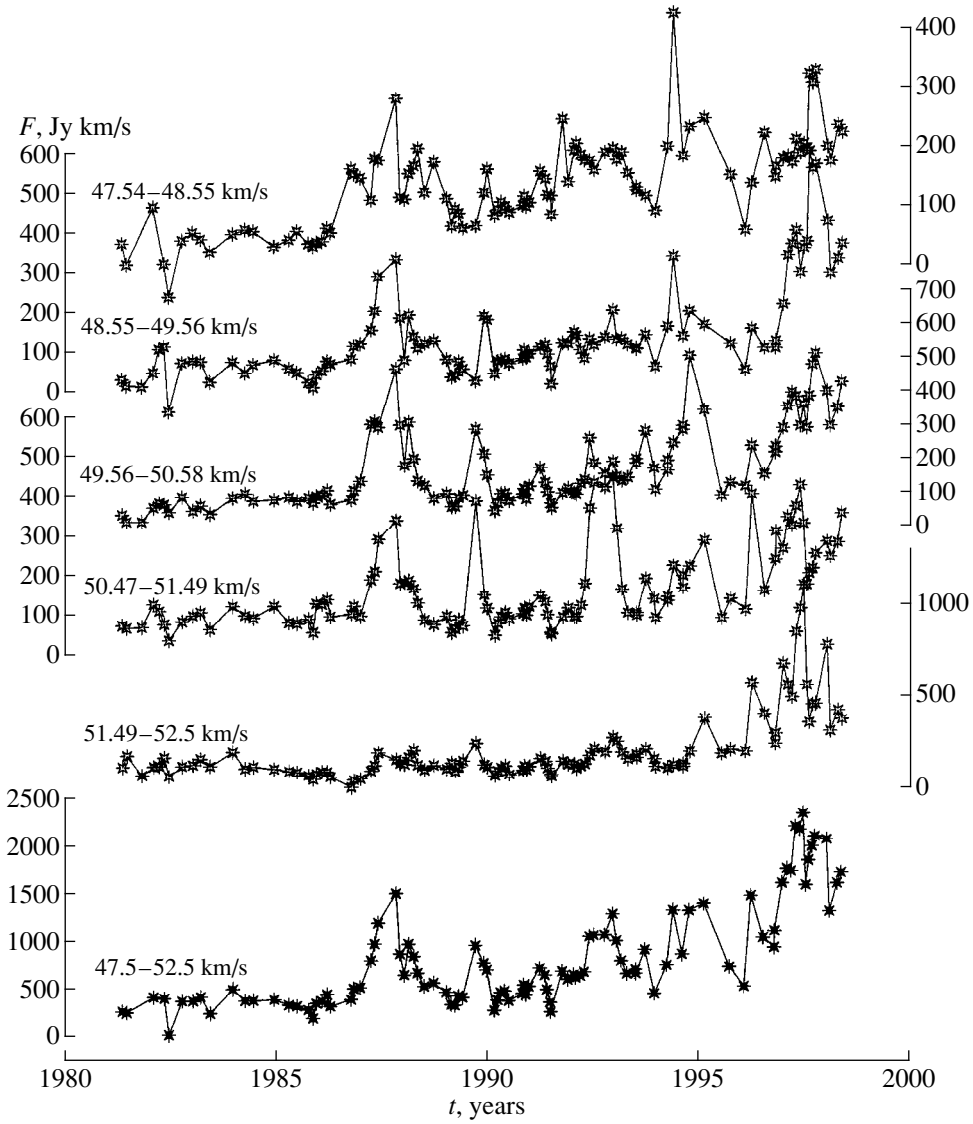

Fig. 5. Flux variations of W51M within individual spectral subintervals in the spectral zone 47.5–52.5 km/s. Lower curve: flux for the entire zone. Other curves: fluxes for velocity ranges 47.5–48.5, 48.5–49.5, 49.5–50.5, 50.5–51.5, and 51.5–52.5 km/s. The similarity of the plots is obvious.

that, on short timescales (about one year), the behavior of these zones can differ, whereas on longer timescales (several years), they behave similarly. In this case, we observe a slow growth of the flux throughout 1981–1998. This effect is not very common, for the following reason. Since the half-width of the spectral lines of H_2O maser sources is usually 0.6–0.7 km/s, an individual line can affect a spectral interval about 1.5 km/s wide via its flux variations. Hence, the similar character of the flux plots for broader spectral zones must be determined by groups of spectral lines distributed over the entire spectrum, whose fluxes display the same behavior on long timescales.

Interferometric observations of this source [9, 12–14] indicate that the emission in lines and entire spectral intervals comes from spatially compact groups of maser condensations with roughly the same range of radial velocities (5–10 km/s). Thus, the flux behavior on long timescales suggests that the emission in each of the spectral zones we have identified is due to a separate group of maser condensations. Figure 6 shows a division of the spectrum into zones based on a comparative analysis of the behavior of their fluxes. Table 2 lists spectral zones with uniform temporal flux behavior.

This division of the spectrum into zones is independent of the division described above, based on the appearance of the mean spectrum (Table 1); it has lower accuracy in delimiting the spectral intervals (of about ±0.5 km/s). Nevertheless, it demonstrates a good correlation with our previous division of the spectrum into

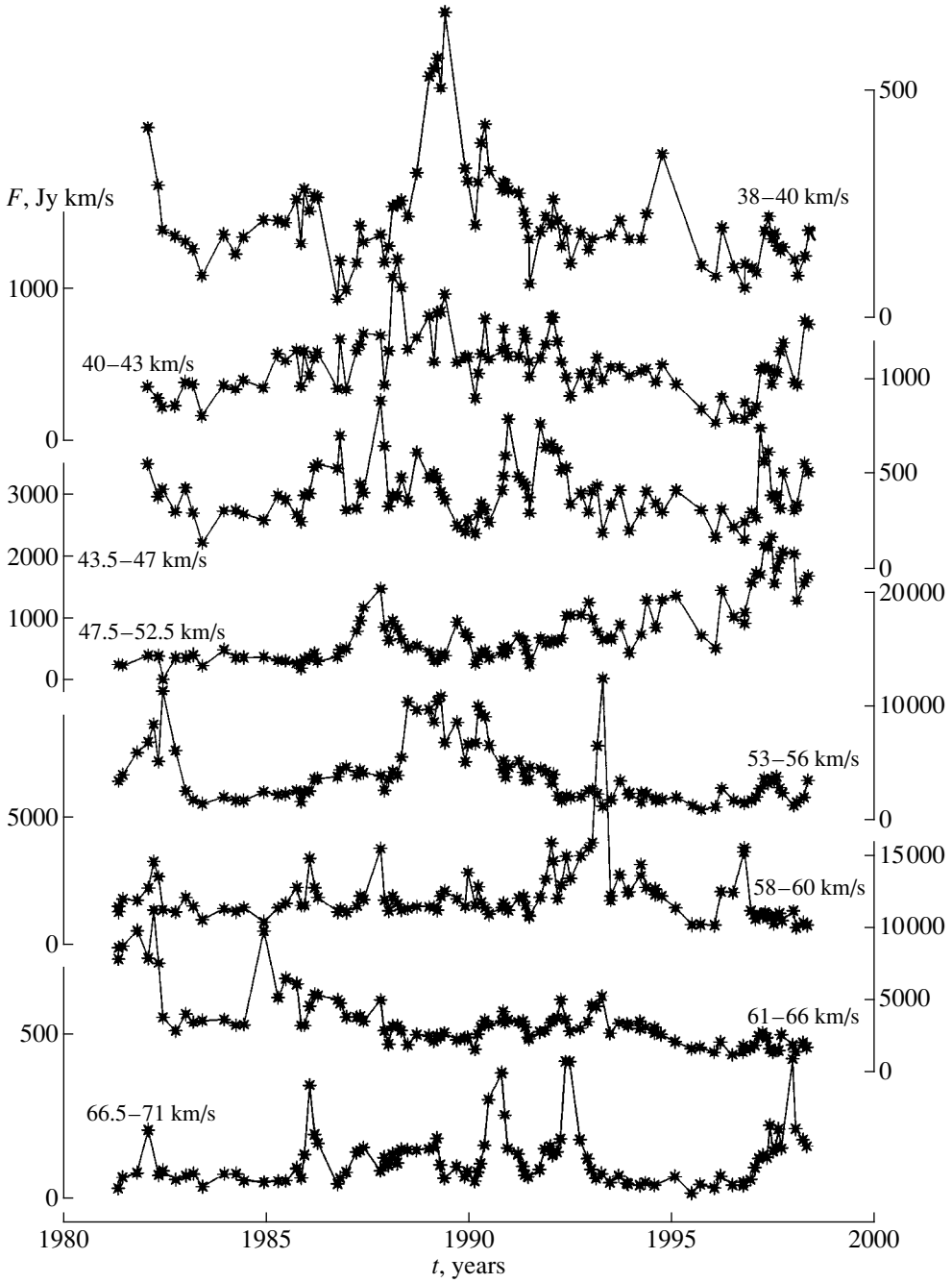

Fig. 6. Variations of the integrated flux of W51M in different spectral zones. Each radial-velocity interval is characterized by uniform temporal behavior of the flux.

zones (Table 1). We can identify corresponding pairs of spectral ranges found by the two methods for subdividing the spectrum. The results of this comparison are given in Table 3 (the first in each pair corresponds to division based on the mean spectrum).

Again, we note that the division of the mean spectrum beyond 79 km/s is uncertain. Nevertheless, some conformity to the division based on the character of flux variations can be noted even beyond this point on the radial-velocity scale.

We suggest that the spectral division according to flux behavior corresponds more closely to a true separation of the masing region in W51M into nests of maser condensations. The reason is that interferometric maps of W51M [9, 12–15] display prominent compact groups of maser condensations emitting in rather narrow radial-velocity ranges (several kilometers per second). However, quite frequently, groups of maser condensations that are widely separated spatially radiate in approximately the same range of radial velocities. In other words,

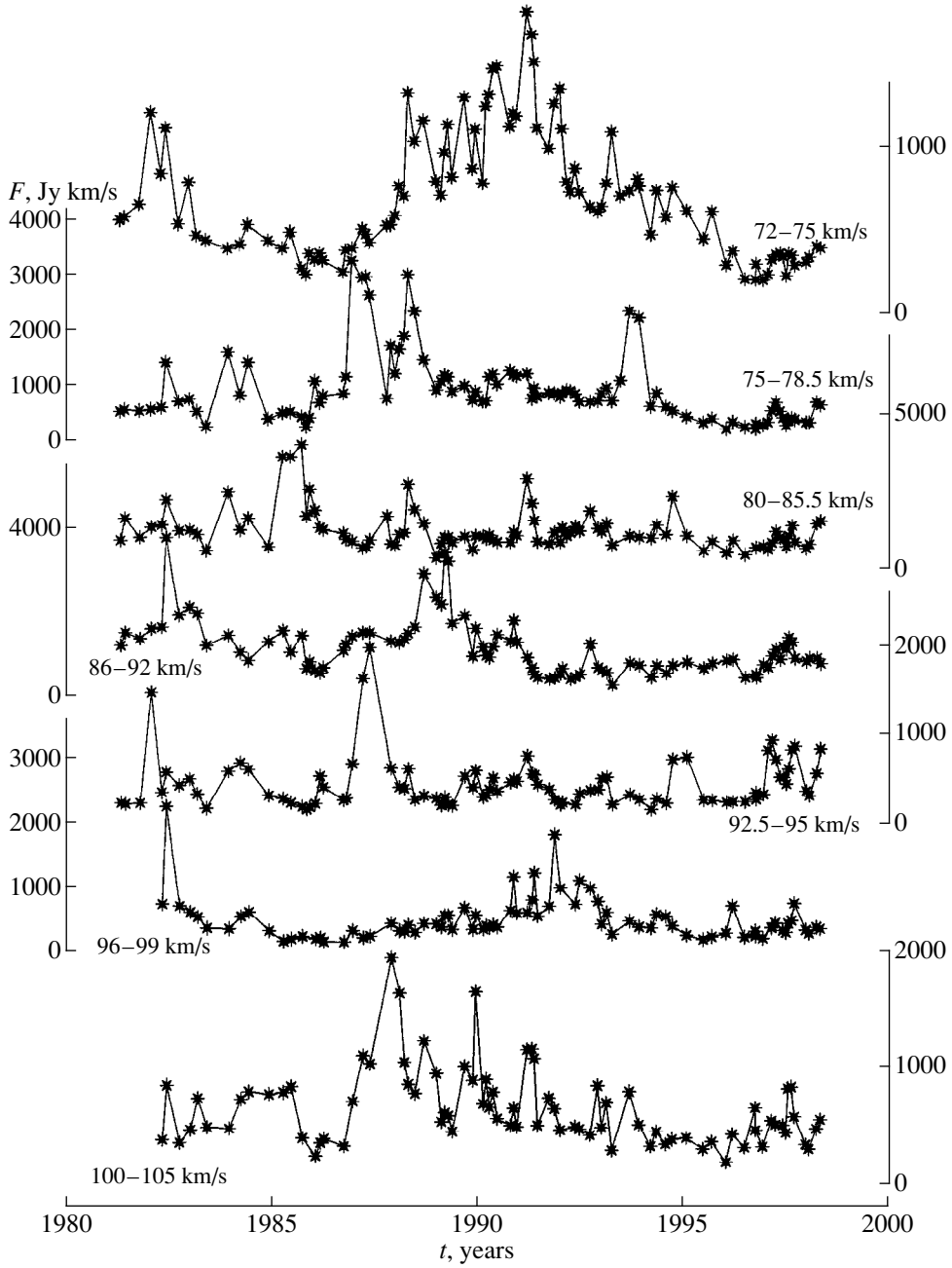

Fig. 6. (Contd.)

features in a particular region of the spectrum are not necessarily physically related to each other. At the same time, it seems rather obvious that the fluxes of all features within each spatially isolated group of maser condensations should display similar time evolutions, which can be followed in changes of the spectrum in the corresponding range of radial velocities. Hence, the inverse statement seems reasonable: a tight group of spectral features showing similar flux evolution on timescales of several years is likely to be associated with the emission of a compact nest of maser condensations.

A careful comparison of the behavior of the integrated fluxes in different spectral zones frequently indicates that rises or declines in their fluxes on timescales of several years are either correlated or anti-correlated. In particular, adjacent radial-velocity intervals often display opposite trends: when the flux in one interval is at a maximum over several years, the flux in a neighboring interval is at a minimum; i.e., they are anti-correlated. Such pairs of adjacent intervals demonstrating anti-correlated flux variations include three ranges with somewhat indistinct anti-correlations [(47–52.5)–(53–56) km/s, (72–

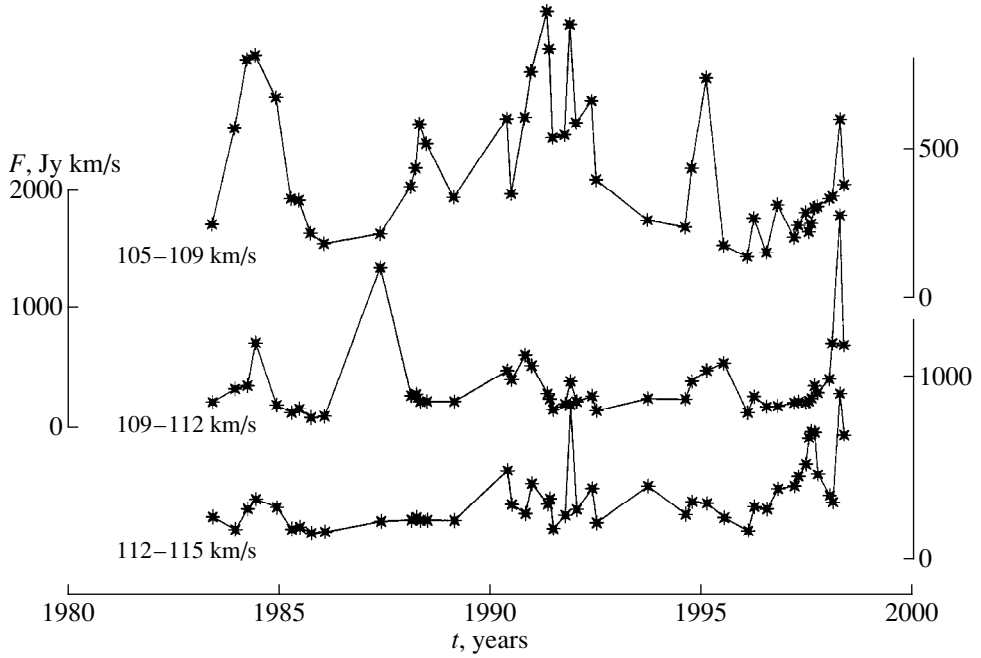

Fig. 6. (Contd.)

75)–(75–78.5) km/s, and (96–99)–(100–105) km/s] and a fourth range displaying a clear anti-correlation [(61.5–66)–(66.5–71) km/s].

Such anti-correlations could be associated with a transfer of flux from one interval to another (movement of spectral features from one zone to another). However, this explanation cannot operate for anti-correlated intervals that are not adjacent to each other. At the same time, there are examples of non-adjacent intervals for which anti-correlations are rather clear, such as (38–40)–(43.5–47) km/s and (53–56)–(61–66) km/s. This latter case is of special interest, since these zones contain the blue and red wings of the central part of the spectrum. Similar phenomena have been reported in studies of other H_2O maser sources based on observations with the Pushchino 22-m telescope [23, 27].

There are several pairs of intervals whose flux behavior is correlated, which are frequently non-adjacent in the spectrum: (38–40)–(53–56) km/s (a fairly clear correlation, which is unusual, since these intervals are probably dominated by W51N and W5M, respectively), (53–56)–(72–75) km/s (a distinct correlation), and (53–56)–(105–109) km/s (a distinct correlation with an appreciable time delay). The variations at (105–109) km/s lag behind those at (53–56) km/s by roughly two years. A similar unusual correlation is observed for the pair (61–66)–(100–105) km/s, with a lag of approximately 2.5 years. The interferometric map of [9] suggests that the spectral intervals (100–105) km/s and (105–109) km/s could be dominated primarily by one of the high-velocity groups of maser condensations located to the north and south of the activity center of W51M, at similar projected distances of ~0.120″ (1.3×10^{16} cm, or 800–900 AU). We will return to this in the Conclusion.

A more detailed discussion of the correlations between spectral intervals in W51M will be presented in a forthcoming paper, in which we will compare individual spectral zones with nests of maser condensations on interferometric maps [9, 12–15].

Table 3. Comparison of the W51M spectral division based on the two different methods (see Tables 1 and 2)

Interval of V_{LSR} (km/s) based on the mean spectrum	Interval of V_{LSR} (km/s) based on the flux behavior
37.5–45	40–43
45–53	47.5–52.5
53–66:	
53–58.5	53–56
58.5–60.2	58–60
60.2–66	61–66
66–72.5	66.5–71
72.5–79	72–75 75–78.5
79–90	Two zones 80–85.5 and 75–78.5
90–95.5	92.5–95
95.5–100.5	96–99
100.5–109	Two zones: 100–105 and 105–109
109–118.5	Two zones: 100–112 and 112–115
118.5–126	Insufficient data statistics

4. DISCUSSION AND CONCLUSIONS

Based on our joint analysis of spectra of W51M and the fluxes from various spectral intervals, we draw the following conclusions.

(1) The entire set of W51M spectra for 1981–1998 and the mean spectrum indicate a central zone of emission at 53–66 km/s. This zone emits about 60% of the total flux of W51M and is split into a blue wing (53–58.5 km/s), central region (58.5–60.2 km/s), and a red wing (60.2–66 km/s). It is known from [8] that the position of W51M is coincident with the source G49.5–0.4, which has a radial velocity of V_{LSR} = 59.0 km/s, in good agreement with the central velocity of the W51M spectra. Interferometric maps [12, 14, 15, 21] indicate that the main groups of maser condensations lie near the activity center of the maser emission region. The blue and red features belong to two main groups of maser condensations [28] separated by 0.025″ (2.6×10^{15} cm, or 175 AU). It is probable that the same groups are traced on the map of [9]. However, the separation between them found in [9] is about 0.040″–0.050″ (280–350 AU).

Based on the mean spectrum and the behavior of the fluxes in different spectral intervals, we have divided the spectrum into zones, presented in Table 3. The zone boundaries are somewhat uncertain and slightly dependent on the method for division of the spectrum.

(2) Our analysis of the flux variations in the entire spectrum throughout the observation interval, also taking into account the data of [21], indicates that the total flux varied sinusoidally with a period of 12–13 years (with minima in 1969–1970, 1983–1984, and 1996). The ratio of the maximum to the minimum fluxes is approximately 2.5.

(3) We have found a number of pairs of spectral intervals whose flux variations are either correlated or anti-correlated. The flux behavior for some spectral intervals (109–112, 100–105 km/s) display temporal shifts of about two to three years with respect to the central part of the spectrum (containing the center of the maser activity of the W51M region). The interferometric map of [9] suggests that these spectral intervals are dominated by high-velocity groups of maser condensations located to the north and south of the W51M activity center at approximately equal projected distances of ~0.120″ (1.3×10^{16} cm, or 800–900 AU). In this case, the changes in the behavior of the maser condensations propagate at a velocity of $\approx(1.5–2.0) \times 10^3$ km/s. This value is consistent with the stellar-wind velocity, suggesting that the stellar wind is the main mechanism for maser pumping in W51M. Similar stellar-wind velocities for massive stars were found in the theoretical study [28], and also in direct observations of jet outflows from the young massive star HH 80–81 [29]. The velocity of these jets is $(0.6–1.4) \times 10^3$ km/s, consistent with our data.

(4) Genzel *et al.* [9] proposed two models for W51M: (a) a rotating and expanding disk (torus) with bipolar outflows along its poles, and (b) an expanding envelope with outlets channeling high-velocity jets of maser condensations. Figure 13 in [9] shows the computed emission spectra for the different source models. Comparing these models with our data, we suggest that W51M is a rotating and simultaneously expanding toroidal cloud of gas and dust. Numerous high-velocity jets, consisting of separate groups of maser condensations, flow outward in two broad cones along the poles of the torus. The spectral interval 53–66 km/s is responsible for the torus emission. The blue wing (53–58.5 km/s) comes from the side of the torus that approaches the observer as a result of rotation. The red wing (60.2–66 km/s) is produced by the receding edge of the torus. The mean linear size of the torus is about 175–350 AU [9, 14].

The jets are manifest in the remaining spectral zones (especially the high-velocity zones, with radial velocities above 90 km/s) and can be traced on interferometric maps to distances of 2000–3000 AU. On large-scale maps [9], some features are visible at distances up to 2″(14×10^3 AU). Moreover, infrared observations [6] indicate that jet outflows with their center in the W51M region are clearly visible to 15″–30″ from the outflow center! This corresponds to a distance of the order of 100000–200000 AU; i.e., several tenths of a parsec. An even more distinct pattern of jet outflows in broad cones can be found in [30, 31] for the source IRc 2 in Orion (it also corresponds to the maser source Ori A and to Ori KL). According to [30, 31], the jet-outflow cones extend to more than 2′; for a distance of 0.45 kpc [7], this corresponds to linear scales >50000 AU. The smaller scale of the phenomenon in W51M may be due to the smaller mass of its central young star. Based on the centripetal motions of some condensations, Genzel *et al.* [9] estimated the mass of the central star of W51M to be $15M_\odot$. However, they assumed free fall of the condensations toward the center. Since the orbital motions of these condensations can be projected onto the plane of the sky, this estimate corresponds to a lower limit for the mass of the young star in W51M.

Thus far, our statements about the structure of W51M are to some extent preliminary. Firmer conclusions require a more detailed statistical analysis of the behavior of spectral features throughout the entire observation period (1981–1998), as was done in [27, 32]. The results of such an analysis will be presented in a separate paper.

ACKNOWLEDGMENTS

The authors are grateful to E.E. Lekht for his careful, long-term observations of the maser source W51M in 1981–1993, help with the subsequent observations, useful discussions on spectral data processing, and valuable comments on the preparation of the article. We are also grateful to I.I. Berulis for help with the observations and with the preparation of this article, and for fruitful discussions. This work was supported by the Russian Foundation for Basic Research (project code 99-02-16293).

REFERENCES

1. W. M. Goss and P. A. Shaver, Aust. J. Phys. Astrophys. Suppl. **14**, 1 (1970).
2. S. H. Knowles, C. H. Mayer, A. C. Cheung, *et al.*, Science **163**, 1055 (1969).
3. D. Crampton, Y. M. Georgelin, and Y. P. Georgelin, Astron. Astrophys. **66**, 1 (1978).
4. G. L. Mader, K. J. Johnston, and J. M. Moran, Astrophys. J. **224**, 115 (1978).
5. P. M. Harvey, M. Joy, D. F. Lester, and B. A. Wilking, Astrophys. J. **300**, 737 (1986).
6. J. D. Goldader and C. G. Wynn-Williams, Astrophys. J. **433**, 164 (1994).
7. F. Palagi, R. Cesaroni, G. Comoretto, *et al.*, Astron. Astrophys., Suppl. Ser. **101**, 153 (1993).
8. S. L. Mufson and H. S. Liszt, Astrophys. J. **232**, 451 (1979).
9. R. Genzel, D. Downes, M. H. Schneps, *et al.*, Astrophys. J. **247**, 1039 (1981).
10. W. T. Sullivan, Astrophys. J., Suppl. Ser. **25**, 393 (1973).
11. L. T. Little, G. J. White, and P. W. Riley, Mon. Not. R. Astron. Soc. **180**, 639 (1977).
12. R. Genzel, D. Downes, J. M. Moran, *et al.*, Astron. Astrophys. **66**, 13 (1978).
13. R. Genzel, D. Downes, J. M. Moran, *et al.*, Astron. Astrophys. **78**, 239 (1979).
14. R. C. Walker, B. F. Burke, A. D. Haschick, *et al.*, Astrophys. J. **226**, 95 (1978).
15. T. Liljestrom and K. Leppanen, in *Proceedings of the 2nd Guillermo Haro Conference on Interstellar Turbulence*, Puebla, México, 1998.
16. R. Barvanis and S. Deguchi, Astron. J. **97**, 1089 (1989).
17. A. D. Kuz'min and A. E. Salomonovich, *Radio-Astronomical Methods for the Measurement of Antenna Parameters* [in Russian] (Sov. Radio, Moscow, 1964), p. 151.
18. J. D. Kraus, *Radio Astronomy* (McGraw-Hill, New York, 1966; Sov. Radio, Moscow, 1973), p. 95.
19. J. W. M. Baars, R. Genzel, I. I. K. Pauliny-Toth, and A. Witzel, Astron. Astrophys. **61** (1), 99 (1977).
20. M. H. Schneps, J. M. Moran, R. Genzel, *et al.*, Astrophys. J. **249**, 124 (1981).
21. G. J. White and G. H. Macdonald, Mon. Not. R. Astron. Soc. **188**, 745 (1979).
22. E. E. Lekht, J. E. Mendoza-Torres, and R. L. Sorochenko, Astron. Zh. **72**, 39 (1995) [Astron. Rep. **39**, 34 (1995)].
23. E. E. Lekht, Pis'ma Astron. Zh. **20**, 464 (1994) [Astron. Lett. **20**, 395 (1994)].
24. E. E. Lekht, Astron. Astrophys. Trans. **11**, 303 (1996).
25. I. I. Berulis, E. E. Lekht, and J. E. Mendoza-Torres, Astron. Zh. **72**, 468 (1995) [Astron. Rep. **39**, 411 (1995)].
26. I. I. Berulis, E. E. Lekht, V. A. Munitsyn, and G. M. Rudnitskiĭ, Astron. Zh. **75**, 394 (1998) [Astron. Rep. **42**, 346 (1998)].
27. E. E. Lekht, J. E. Mendoza-Torres, and R. L. Sorochenko, Astrophys. J. **443**, 222 (1995).
28. J. M. Stone, Xu Jianjum, and L. G. Mundy, Nature **377**, 315 (1995).
29. J. Marti, L. F. Rodríguez, and Bo Reipurth, Astrophys. J. **449**, 184 (1995).
30. M. M. MacLow, Nature **377**, 287 (1995).
31. D. A. Allen and M. G. Burton, Nature **363**, 54 (1993).
32. E. E. Lekht, Astron. Zh. **72**, 31 (1995) [Astron. Rep. **39**, 27 (1995)].

Translated by G. Rudnitskiĭ

Astronomy Reports, Vol. 45, No. 5, 2001, pp. 350–360. Translated from Astronomicheskiĭ Zhurnal, Vol. 78, No. 5, 2001, pp. 408–420.

Coordinated Observations of Cyg X-1 (V1357 Cyg) from 1994–1998 in the Commonwealth of Independent States

E. A. Karitskaya[1], I. B. Voloshina[2], V. P. Goranskiĭ[2], K. N. Grankin[3], É. B. Dzhaniashvili[4], O. V. Ezhkova[3], N. T. Kochiashvili[4], M. I. Kumsiashvili[4], A. V. Kusakin[2], V. M. Lyutyĭ[2], S. Yu. Mel'nikov[3], and N. V. Metlova[2]

[1]*Institute of Astronomy, Russian Academy of Sciences, ul. Pyatnitskaya 48, Moscow, 109017 Russia*
[2]*Sternberg Astronomical Institute, Universitetskiĭ pr. 13, Moscow, 119899, Russia*
[3]*Institute of Astronomy, National Academy of Sciences of Uzbekistan, Astronomicheskaya ul. 33, Tashkent, 700052 Uzbekistan*
[4]*Abastumani Astrophysical Observatory, Academy of Sciences of Georgia, Gora Kanobili, Abastumani, 383762 Georgia*

Received July 14, 2000

Abstract—We present observations of Cyg X-1 obtained during the coordinated international campaign "Optical Monitoring of Unique Astrophysical Objects," carried out in observatories of CIS countries (Georgia, Kazakhstan, Russia, Uzbekistan, and Ukraine) in 1994–1998. The data are presented as a single set, taking into account systematic differences between individual data sets. In total, 2258 *UBVR* observations were obtained during 407 nights. The observations were carried out simultaneously with X-ray observations at 2–10 keV (ASM/RXTE) and 20–100 keV (BATSE/CGRO), and also with radio observations (in 1997). Our optical data partially overlap the soft X-ray outburst in 1996 (JD 2450200–320) and subsequent hard state, which displayed various types of increases and decreases of the X-ray flux. The 1996 outburst was not accompanied by any optical brightening. However, an orbital light curve corresponding to a tidally distorted star was superimposed on individual flares and brightness dips. For example, in two independent sets of observations, an intense optical flare with amplitude $0\overset{m}{.}04$ above the quiescent level was detected on JD 2450988, preceding the X-ray flare on JD 2451000–51040. In this time interval, the system displayed chaotic intrinsic variability on a timescale of a day, and flares and brightness dips with amplitude $0\overset{m}{.}10$ lasting up to several days. The variability power spectra display a predominant secondary period at $147^{\mathrm{d}} \pm 2^{\mathrm{d}}$, which is half the 294^{d} "precessional" period previously found at both X-ray and optical wavelengths. We show that the 147^{d} period dominates in X-ray data (ASM/RXTE) in the quiescent state, or after subtraction of the 1996 outburst radiation from the X-ray light curve. This period is also close to the period of $142^{\mathrm{d}} \pm 7^{\mathrm{d}}$ derived from recent radio data. Cross-correlation analysis confirms a significant correlation between the long-term optical and 2–10 keV X-ray variations (without the soft X-ray outburst), with the X-ray variations lagging by 12 ± 2 days. © *2001 MAIK "Nauka/Interperiodica".*

1. INTRODUCTION

The X-ray source Cyg X-1 is identified with the optical variable star V1357 Cyg. This is a massive close binary with orbital period $5\overset{\mathrm{d}}{.}6$, in which one of the components is an O9.7Iab star and the other a massive compact object (possibly a black hole). The estimated mass of the supergiant is $18M_{\odot}$, and that of the compact object is $10M_{\odot}$ [1].

The main source of optical radiation in the Cyg X-1 system is the O9.7Iab supergiant. The orbital light curve of the system is dominated by a double wave with amplitude $0\overset{m}{.}04$, due to the tidal distortion of the O star. The light curve is superimposed with variations that reflect processes related to the accretion disk around the relativistic component and the mass exchange between the components. Due to the low amplitude of the variability of these processes, studying them requires excellent weather conditions, which, as a rule, are realized with high-altitude observatories, well-adjusted equipment, and correct account for atmospheric and instrumental factors.

Our observations of Cyg X-1 started in 1995 as part of the coordinated program "Optical Monitoring of Unique Astrophysical Objects," and were carried out at observatories located in Georgia, Kazakhstan, Russia, Uzbekistan, and Ukraine. The results have been partially published [2–4]. Here, we aim to combine the entire volume of the data, taking into account systematic differences between individual data sets. This problem is particularly important since our intensive photometric observations were carried out in parallel with observations in soft (2–10 keV) X-rays (ASM/RXTE; we used preliminary results presented in July 1999 by the ASM/RXTE research group at the WWW site space.mit.edu/XTE/), hard (20–100 keV) X-rays (BATSE/CGRO) [4], and the radio (15 GHz) (Mullard Radio Astronomy Observatory, Cambridge, England) [4].

1063-7729/01/4505-0350$21.00 © 2001 MAIK "Nauka/Interperiodica"

List of data sets

No.	Observatory	Observing season	Instrument	Standard star	Observer(s)
I	Sternberg Institute, Crimean base	1996–1998	SAI 60-cm telescope, *UBV* photometer	BD + 34°3816	Lyutyĭ, Metlova
II	Sternberg Institute, Crimean base	1994–1998	SAI 60-cm telescope, *UBV* photometer	BD + 34°3816	Voloshina
III	Abastumani Observatory, Georgia	1995	48-cm telescope, *UBVR* photometer	BD + 34°3812	Dzhaniashvili
IV	Abastumani Observatory, Georgia	1996–1998	48-cm telescope, *UBV* photometer	BD + 34°3812	Kochiashvili, Kumsiashvili
V	Tien-Shan observatory, Kazakhstan	1995–1996	1-m Telescope, *WBVR* photometer	BD + 34°3812 BD + 35°3895	Goranskiĭ, Karitskaya
VI	Maĭdanak Observatory, Uzbekistan	1995–1998	48-cm Telescope, *UBVR* photometer	BD + 34°3812 BD + 35°3895 BD + 40°4147	Grankin, Ezhkova, Mel'nikov
VII	Moscow, SAI Crimean Observatory (CrAO), Zvenigorod Observatory, Institute of Astronomy (INASAN)	1995–1998	70-cm telescope 38-cm telescope 60-cm telescope *UBV* photometer	BD + 34°3812 BD + 35°3895	Goranskiĭ, Kusakin, Karitskaya

This provides a unique opportunity to compare the behavior of Cyg X-1 at optical wavelengths with that in other spectral ranges, as was done in [3, 4]. In particular, in [3], different types of variability were revealed and connections between them established. A delay of about a week of the long-term X-ray variations relative to the optical variations was detected, and a possible physical interpretation was suggested. The data obtained enable estimation of the characteristic time needed for matter to pass through the accretion disk.

In the analysis presented here, we use extended photometric data obtained over four years.

2. OBSERVATIONS

In 1994–1998, the participants of the campaign obtained 2258 observations during 407 nights. The Table presents information about the equipment, telescopes, reference stars, and observers.

At the Tien-Shan Observatory, the observations were carried out with the four-channel *WBVR* photometer designed by Kornilov and Krylov [5], with beam splitting achieved with dichroic plates. The response functions of the photometer *BVR* channels are close to the Morgan–Johnson system, and standard filters were used. However, the reproduction of the Strajzhys *W* ultraviolet band without use of a filter was inaccurate, and this response function was closer to the *U* band. A detailed study of the photometer band transparency with and without filters (in particular, for the *UV* band) is presented in [6]. As in [3], the *UV* observations were reduced to the *U* Morgan–Johnson system taking into account a constant correction coefficient; we denote these reduced observations by *u*.

The other photometers used are based on a standard single-channel design with filters providing photometric bands close to the *UBV* Morgan–Johnson bands. Most observers used the reference star **c** from [5] BD + 34°3812, which has roughly the same brightness as the variable. Like BD + 34°3812, Cyg X-1 is an early-type star; however, its color differs due to the presence of appreciable interstellar reddening. Therefore, starting from 1971, in order to minimize the color-difference correction, Lyutyĭ [7] chose star **a**(BD + 34°3816) as a local standard star for Cyg X-1 observations in the *UBV* bands. In 1978, this star was suspected to be a low-amplitude, possibly periodic variable [8], and denoted V1674 Cyg. A targeted study of V1674 Cyg carried out by several participants of the campaign (V.P. Goranskiĭ, E.A. Karitskaya, K.N. Grankin, and O.V. Ezhkova) [9] confirmed that the star is indeed a low-amplitude ($\sim 0^m.01$) variable with periodic components in its light curve. I.B. Voloshina, V.M. Lyutyĭ, and N.V. Metlova used it as a reference star in our campaign observations. We studied this section of the Crimean observations to search for components due to V1674 Cyg in the power spectrum of Cyg X-1. No significant features of the reference star were detected in the frequency spectrum, due to their low amplitude relative to that of the irregular variability Cyg X-1.

Some observers used the reference stars HD 189474 (BD + 35°3895) and HD 229196 (BD + 40°4147). The latter was previously suspected to be a low-amplitude variable [10]; it is known as NSV 25130 and was rediscovered by us in 1996 data from the Maĭdanak Observatory [3]. When NSV 25130 was confirmed to be a periodic variable [3], the 1995–1996 Maĭdanak observations were corrected to compensate for the variability of this comparison star. Different reference stars were chosen for the 1997–1998 Maĭdanak observations: BD + 35°3895 and BD + 34°3812.

Since various instruments and reduction techniques were used in the observations, it is necessary to take into

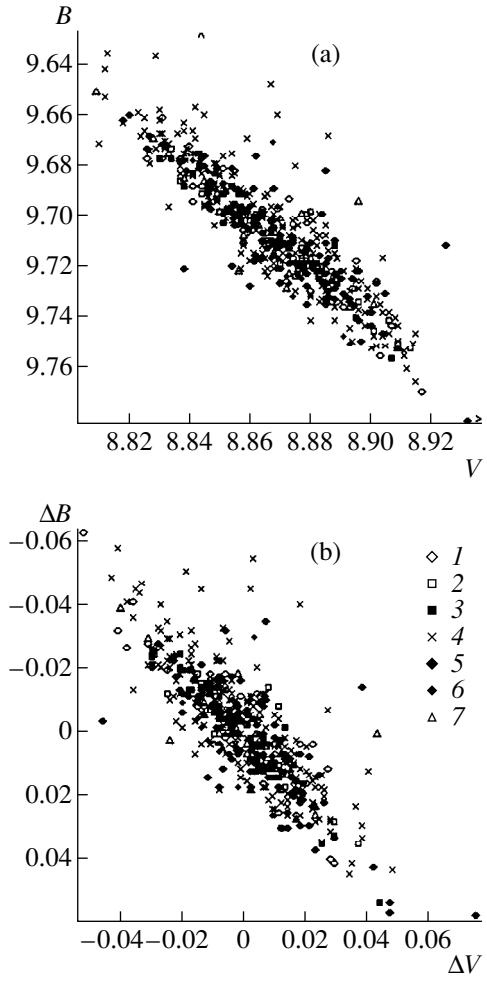

Fig. 1. (a) Relation between *B* and *V* for the following data sets: (*1*) Voloshina (Crimea; dataset II), (*2*) Dzhaniashvili (Georgia, Abastumani; III), (*3*) Goranskiĭ and Karitskaya (Tien-Shan; V), (*4*) Grankin, Ezhkova, and Mel'nikov (Maĭdanak; VI), (*5*) Lyutyĭ and Metlova (Crimea; I), (*6*) Kochiashvili and Kumsiashvili (Abastumani; IV), (*7*) Goranskiĭ, Karitskaya, and Kusakin (Shugarov–Volkov photometer used in Crimea, Moscow, and Zvenigorod; VII). (b) Relation between residuals after subtraction of the mean orbital light curve (double wave) in the *B* and *V* bands. These ΔB and ΔV residuals reflect real physical variability of Cyg X-1.

account systematic differences between data sets obtained with different equipment and processed by different authors, in order to derive a single homogeneous dataset. This procedure is simplified by the fact that the brightness and color-index variations of the object have low amplitudes. In addition, the observations were so dense that each individual dataset contains a sufficient number of points coincident with points from other data sets (quasi-simultaneous observations) to enable derivation of relative corrections. Naturally, the intrinsic variability of Cyg X-1 during a night affects the accuracy of these corrections; however, this small variability exceeded the photometric errors on only two nights, during outbursts.

Corrections for each dataset were determined from quasi-simultaneous observations. The data obtained with the Shugarov–Volkov photometer turned out to be inhomogeneous, since they were acquired with different telescopes. Corrections were made separately for the 38-cm and the 60–70-cm reflectors. Figure 1a presents the dependence of *B* on *V* in the final data set; the correlation coefficient is 0.89. The various symbols indicate individual data sets; a key to the symbols is given in the figure caption. The correlation coefficients for the dependences of *U* and *R* on *V* are 0.82 and 0.89, respectively. These values show the rather high average internal accuracy of the final data sets. Most of the points in Fig. 1a are located along a line with a slope of 45°, so that the color index *B*–*V* is not variable. Nonetheless, we can see deviations of some observations upwards from the main dependence. These deviations could be due to either systematic errors or physical variations in the spectrum of the star (related, for instance, to the appearance of bright Balmer emission lines, as it was shown in [11] for one of the bursts).

The table, which can be found in electronic form at the address http://cdsweb.u-strasbg.fr/pub/cats/j, presents our nightly-averaged *U*(*u*)*BVR* photoelectric observations of Cyg X-1. Column 1 presents the Julian dates of the observations, with fractions of a day; columns 2–5 values for *V*, *B*, *U*, and *R*; columns 6–9 the dispersions in these bands per night; column 10 the number of averaged observations per night; and column 11 a two-letter code denoting the dataset to which the observations are ascribed. The designations in column 11 are ja—E.B. Dzhaniashvili (Abastumani, Georgia, dataset III); mz—N.T. Kochiashvili and M.I. Kumsiashvili (Abastumani, Georgia, dataset IV); lu—V.M. Lyutyĭ and N.V. Metlova (Crimea, dataset I); sh—V.P. Goranskiĭ, A.V. Kusakin, and E.A. Karitskaya (Shugarov–Volkov photometer, Moscow, Zvenigorod, and Crimea, dataset VII); ts—V.P. Goranskiĭ and E.A. Karitskaya (Tien-Shan, Kazakhstan, dataset V); uz—K.N. Grankin, O.V. Ezhkova, and S.Yu. Mel'nikov (Maĭdanak, Uzbekistan, dataset VI); vo—I.B. Voloshina (Crimea, dataset II). These *UBVR* data were processed as described above and used in our analysis.

Figure 2 demonstrates the quality of the reduction of the observations to a single dataset. The horizontal axes show the *V* values for the combined dataset, and the vertical axes the (corrected) *V* values for the same nights for (a) the Crimean dataset I and (b) the Maĭdanak dataset VI, which are the most numerous. The notation is the same as in Fig. 1. Although the dispersions of the dependences exceed that in Fig. 1 (the systematic errors between different data sets exceed the internal errors for each dataset), the mean error for the nightly-averaged observations is expected to be smaller than $0^m.01$.

3. THE LIGHT CURVE OF CYG X-1

Figure 3a presents the 1994–1998 orbital light curve in the *V* band, constructed using the refined orbital elements from [12]:

$$\text{Min I hel} = \text{JD}2441\,163.529(9) + 5^d.599\,829(16)E. \quad (1)$$

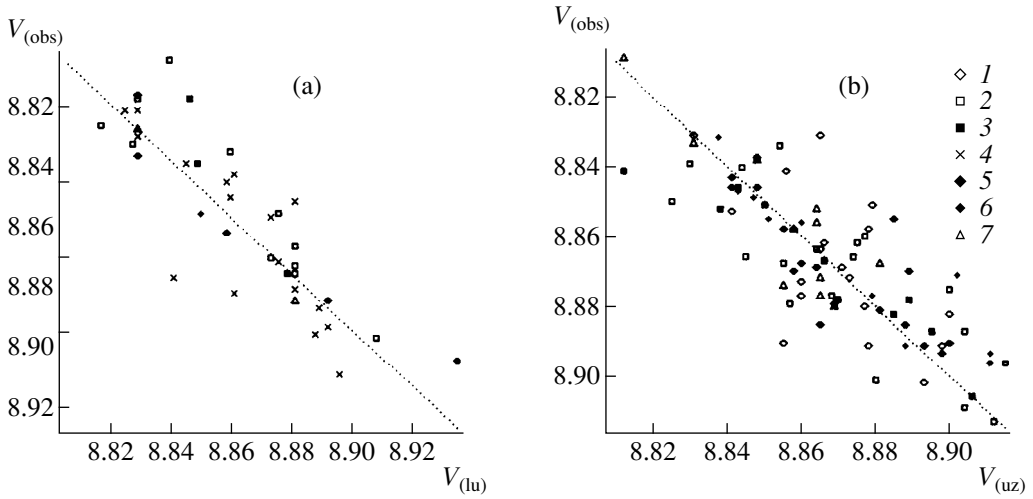

Fig. 2. Relations between V values for various data sets derived from simultaneous observations made on the same nights, after corrections. Relations between observations made by various authors with those made by (a) Lyutyĭ and Metlova (Crimea; I); (b) Grankin, Ezhkova, and Mel'nikov (Maĭdanak; VI). Notation is the same as in Fig. 1.

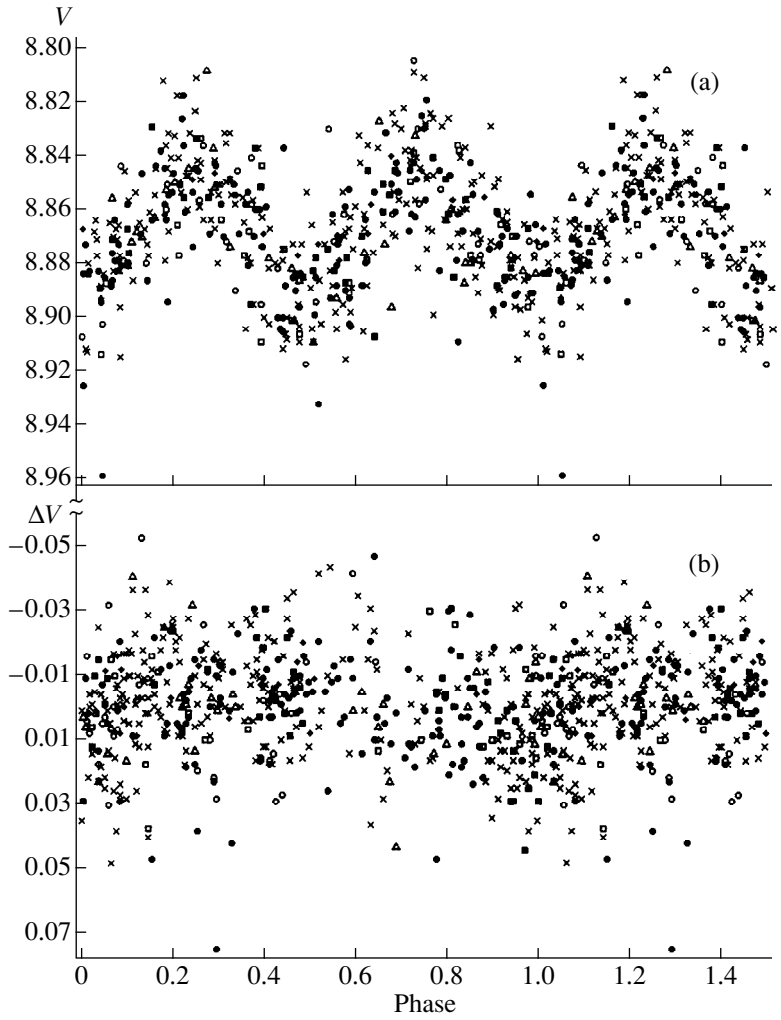

Fig. 3. (a) Orbital phase light curve in the V band and (b) phase curve of the residual ΔV values with period 147 days after subtraction of the V-band orbital wave. Nightly-averaged values are given for each dataset. Notation is the same as in Fig. 1.

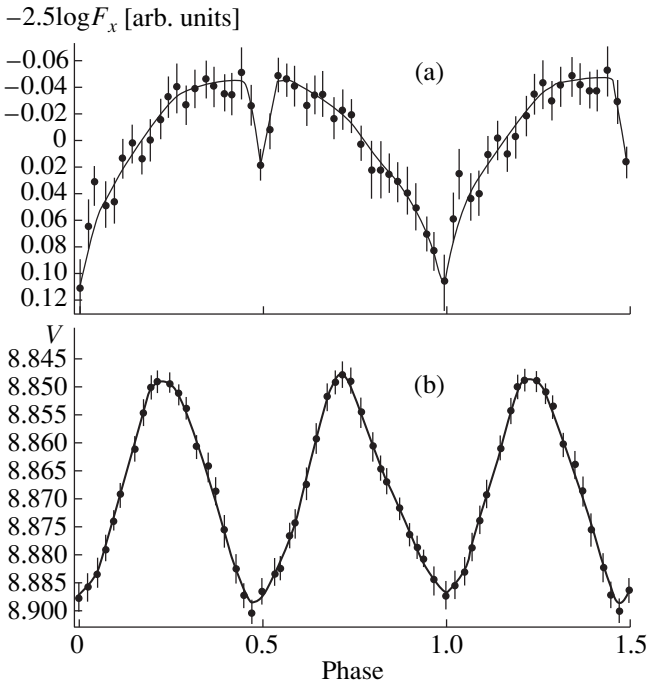

Fig. 4. Comparison between the mean orbital light curves in (a) soft X-rays and (b) the optical (*V* band). The solid smoothed curves were used to subtract the orbital variability.

The notation in Fig. 3 is the same as in Fig. 1. Each symbol corresponds to the average for an individual night from an independent set of observations. We can see that the light curve has the form of a double wave, as is characteristic of ellipsoidal variables, with amplitude $0^m.045$; however, the points show appreciable scatter, up to $0^m.10$. The double wave is due to the rotation of the tidally deformed O star in the course of its orbital motion around the common center of mass of the system. The scatter in the light curve represents physical variability, and reflects primarily the instability of the mass exchange between the components, which may include an accretion disk around a black hole. In order to recognize and study physical variability, we must take into account the influence of the optical component (O star); i.e., we must accurately determine the orbital double wave and subtract it from the total light curve at the appropriate orbital phase.

An mean orbital *V*-band light curve calculated using a sliding average is presented in Fig. 4b. To subtract the double wave and isolate physical variability of the star, we used the solid smoothed average curve. The total amplitude of the *V* orbital variability calculated using all our observations was $0^m.045 \pm 0^m.002$, while the difference in the depths of the minima was $0^m.003 \pm 0^m.002$. Figure 1b presents the relation between the residuals in the *B* and *V* bands after subtraction of the double wave. The correlation coefficient between the residuals (0.81) is high, suggesting the dominance of real physical variability synchronous in the *B* and *V* bands rather than random errors.

Figure 4a presents a mean orbital light curve calculated from the ASM/RXTE soft X-ray data using the same orbital elements (1) as for the optical curve (Fig. 4b). To decrease the dispersion of the mean curve, we subtracted low-frequency components of the Fourier spectrum from the X-ray curve; a well-known pre-whitening technique was used (see, for example, [13]). The total amplitude of the orbital variability in soft X-rays was $0^m.16$. The X-ray curve displays two minima: a deep minimum coincides in phase with the spectroscopic upper conjunction of the relativistic object [4], while the other, shallow and narrow, minimum at phase 0.5 corresponds to its lower conjunction. This latter minimum was not detected in [4], apparently due to the larger averaging interval, but it can be recognized in the light curve in Fig. 7 from [3]. The solid curve in Fig. 4a represents a smoothened X-ray light curve, which was used to take into account the orbital periodicity in the soft X-rays.

In order to identify physical variability, the averaged, smoothened light curves were subtracted (at the appropriate phase) from the optical *V* and (pre-whitened) ASM/RXTE X-ray data sets. In this way, we derived curves showing the physical variability, presented in Fig. 5. The light curves are given according to season, for intervals when photoelectric observations were carried out. In Fig. 5b, we can see the double-peak maximum of a soft (in terms of its spectrum) X-ray outburst, which is not accompanied by similar behavior at optical wavelengths. At the same time, the local minimum between the two peaks of the large outburst is accompanied by a minimum in the slow variability (a decrease in the mean brightness). Figure 5d presents our observations that overlap with the X-ray outburst on JD 2451000–51040. Note that the increase of the X-ray flux began immediately after an intense and brief optical outburst with amplitude $0^m.04$ on JD 2450998. This event is confirmed by two independent sets of observations. We cannot exclude the possibility that the optical outburst was a precursor to the more prolonged X-ray outburst.

Our observations also contain some other intense outbursts. In particular, we can see in Fig. 5b one with its maximum on JD 2450266 (previously described in [3]), which precedes the second peak of a soft X-ray outburst (Fig. 5b). This event was observed at Maĭdanak and the Crimea. The intense outburst on JD 2450635 could also be related to the small local X-ray outburst that followed it.

X-ray outbursts are characterized by an increase in the dispersion of the physical variability, as can be clearly seen in Fig. 5d. This can hardly be due to observational selection effects, since it is clearly visible in the more homogeneous, Crimean, dataset, and the fact that other

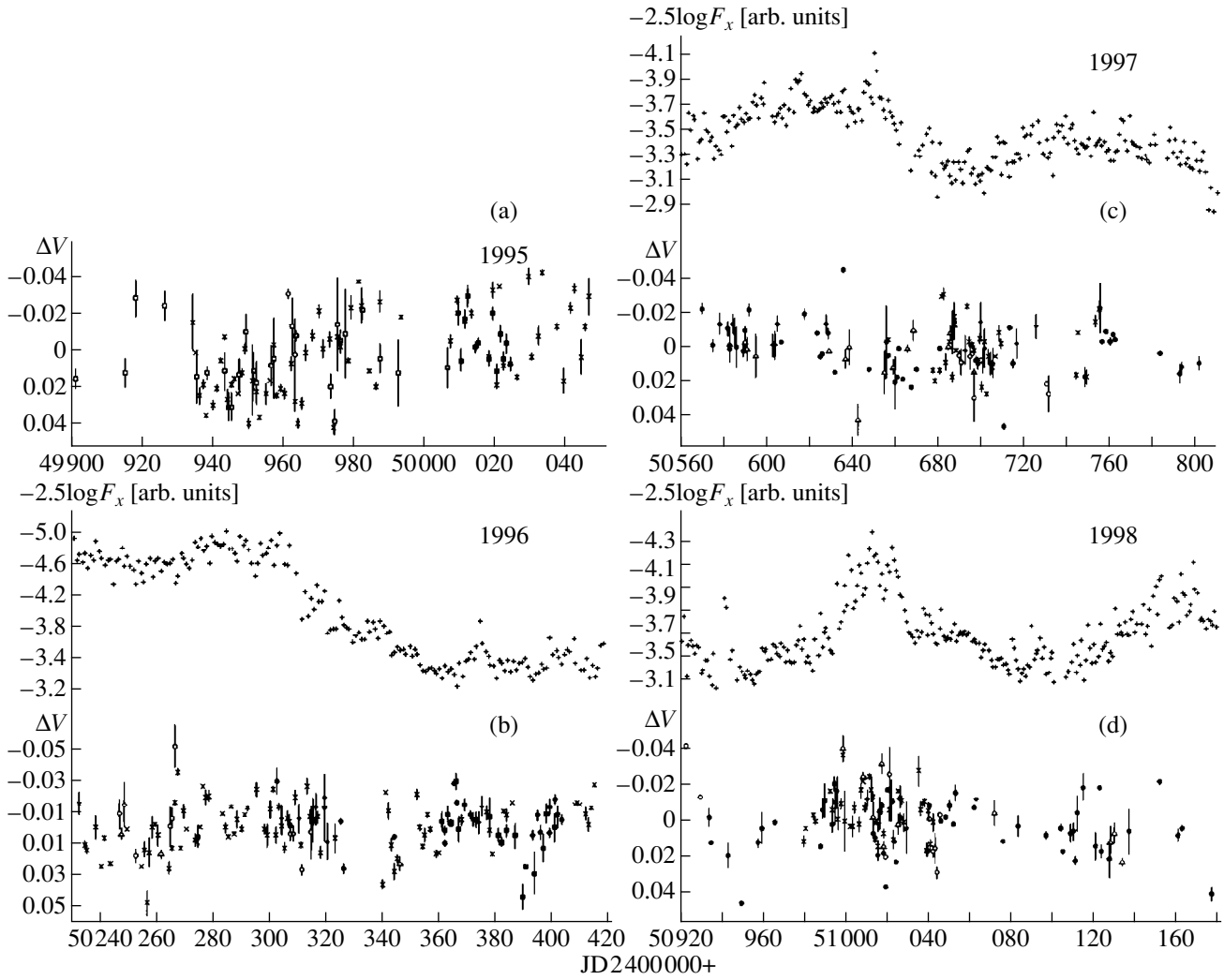

Fig. 5. Comparison between the light curve of physical variability in soft X-rays (ASM/ RXTE) and the *V* band in (b) 1996, (c) 1997, and (d) 1998. The optical light curve for 1995 (a), when no X-ray observations were carried out, is also presented.

observations often confirm individual features in the Crimean light curve only strengthen this conclusion.

In addition to outbursts, Cyg X-1 sometimes displays fairly deep dips in brightness with amplitudes reaching $0^m.04$–$0^m.05$. According to [14], this corresponds to the contribution of the accretion disk to the total brightness of the system. Appreciable brightness decreases were detected on JD 2450256 (lasting no more than one day), JD 2450390, JD 2450642, JD 2450710 (lasting no more than one day), JD 2450949, and JD2451177. The targeted study [15] was dedicated to the brightness dip of Cyg X-1 on JD 2450390. According to the Tien-Shan observations, it lasted about one week. We can see from Fig. 5b that the addition of the Crimean observations appreciably fills out the pattern of this event, and these observations are consistent with the Tien-Shan data. During the gradual egress from the brightness decrease, it is possible that some brightness fluctuations occurred, with the same amplitude as in the regular state, and/or that the duration of the brightness dip was shorter.

It is essential to establish what variations in the light curve were due to the JD 2450390 brightness decrease. The circles in Fig. 6 show a fragment of the light curve of Cyg X-1, while the solid curve shows the mean ellipsoidal orbital curve. We can see that the event is associated with a "disappearance" of the maximum at phase 0.75; in addition, at the maximum phase of the dip, the brightness of the system was lower than in the preceding (secondary) minimum. Kemp *et al.* [16] described a similar situation: the other maximum (at phase 0.25) was not seen over an entire month, whereas the maximum at phase 0.75 was not decreased. The event coincided with an X-ray outburst, similar to that in 1996. An explanation was suggested in [16] based on absorption in a jet ejected from the accretion disk in the course of an intense X-ray outburst.

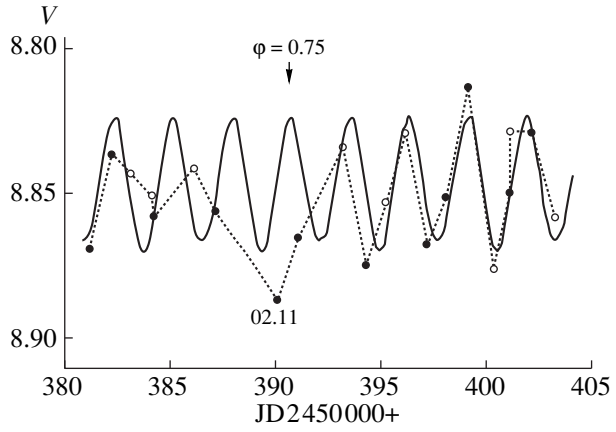

Fig. 6. The brightness dip of November 2–3, 1996 (orbital phase 0.75) in the Tien-Shan (filled circles) and Crimean–Maĭdanak (hollow circles) data. The solid curve indicates the ellipsoidal variability curve.

Some eclipsing binaries display "unequal maxima" and even disappearance of one maximum in the ellipsoidal wave. These phenomena can be understood as the result of absorption in flows of matter in the orbital plane. The orbital inclination of Cyg X-1 is 28°–63° [17], so that the system is not eclipsing. Therefore, it is not reasonable to expect long-lived flows of matter to exist at such a large height above the orbital plane and screen the disk of the O star.

Our observations do not indicate anything similar to the effect described by Kemp *et al.* [16]. In Fig. 3a, we cannot see any dependence of the rate of occurrence of the brightness dips (or the outbursts) or of their depth on orbital phase. The dispersion of the nightly-averaged values is quite uniformly distributed about the ellipsoidal curve, which has a rather symmetrical double-wave shape with equal maxima and minima (Fig. 4b). Our observations did not indicate any long-term variations of the light curve similar to those described in [16] during the 1996 X-ray outburst.

The amplitudes of rapid day-to-day variability are an order of magnitude higher in the X-ray range than in the optical. In addition to outbursts, slow, long-term variations of the mean brightness are characteristic of the soft X-ray variability. Slow variations are also seen in the optical, but with substantially smaller amplitude.

4. COMPARATIVE FREQUENCY ANALYSIS FOR THE X-RAY AND OPTICAL DATA

We carried out a frequency analysis of the 1994–1998 *UBVR* and 1996–1998 X-ray ASM/RXTE (2–10 keV) data using the method of Deeming [18] (Fourier analysis for non-uniform sets). The observations (see the electronic table) were additionally averaged so that one averaged value corresponded to one night, as for the X-ray data. We subtracted a mean light curve with the known orbital elements (1) from the optical data.

In addition to the mean orbital light curve, we subtracted the mean curve for the soft X-ray outburst from the daily-averaged X-ray fluxes on a logarithmic scale. Our use of a logarithmic scale for the X-ray data is justified by the fact that, on this scale, the dispersion of the observations does not depend on time or the level of activity of the object, so that we can consider the entire set, including both hard, low and soft, high states, simultaneously with the same dispersion. We estimated the significance levels of peaks in the power spectra using the empirical technique described by Terebizh [13]. Namely, the initial dataset was randomly scrambled so that each time in the observations was associated with a randomly chosen data value from the same set. The resulting artificial random dataset was then studied statistically. Figures 7a and 7b present a comparison of the power spectra for the X-ray and *V* optical data sets. The solid horizontal lines mark significance levels for the spectral peaks. Figure 7c and 7d show the distribution functions for the amplitudes of the power spectra of the artificial random X-ray (Fig. 7c, on a logarithmic scale) and optical (Fig. 7d) data sets. The examples demonstrate how the 99.99% significance level was determined; the other significance levels were derived from the distribution function in the same way.

Note that, first, the *V*-band observations are the most accurate, since the influence of the atmosphere (the Forbes effect, for example) can be taken into account with the highest accuracy. Second, the *V* dataset is more complete than the *U* and *R* data sets, since the *U* and *R* bands were not available at all our detectors. This is why we present here the results of the *V* observations, although the other data sets were processed in the same way. We noted earlier that the observations in different bands are well correlated, and their power spectra, in general, resemble one another. However, some differences still exist. The main difference between the spectra of the optical and ASM/RXTE data sets is that the former contains a number of spurious yearly-conjugate peaks, since it is discontinuous with a one year period (Cyg X-1 was observable only in summer and autumn). This complicates the analysis of the optical observations.

The period $150^d \pm 2^d$ dominates in the X-ray power spectrum, while the similar period $147^d \pm 2^d$ dominates in the optical. The frequency analysis indicated that these periods are not significantly different. (The high 245^d peak (Fig. 7b) located nearby is a yearly-conjugate peak associated with the 147^d period.) The total amplitudes of the periodic components in the X-ray and optical are $0\overset{m}{.}16$ and $0\overset{m}{.}012$, respectively. Both the X-ray and optical secondary periods are close to half the well known "precessional" period of 294^d, previously detected in X-ray [19] and optical [20] data. In addition, the optical period $147\overset{d}{.}0$ is close to that of radio flux modulations at 15 GHz, equal to $142^d \pm 7^d$, according to Mullard Radio

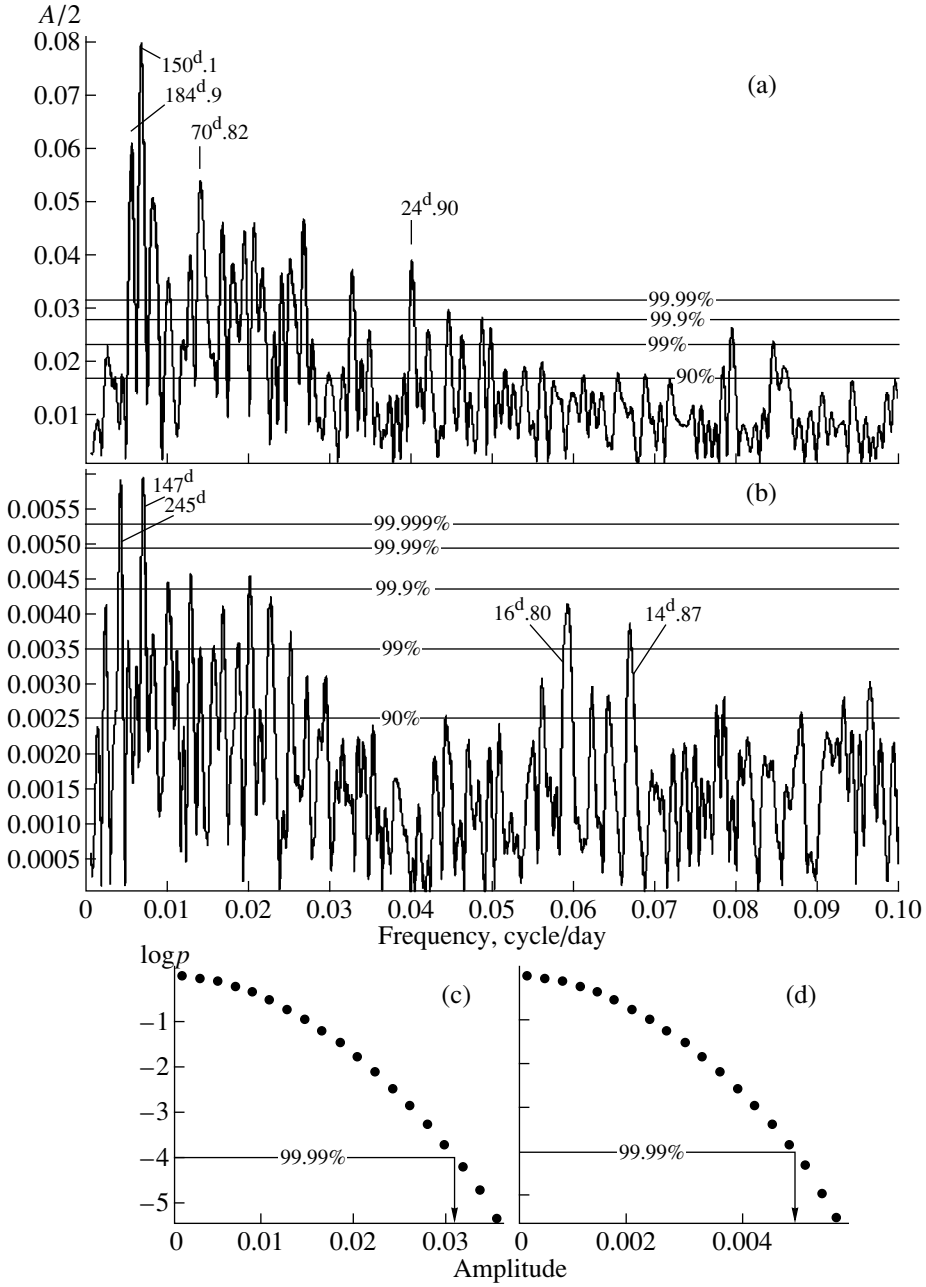

Fig. 7. Comparison between the frequency spectra for the (a) ASM/RXTE (2–10 keV) X-ray and (b) optical *V* band observations. The vertical axes plot the amplitudes of the harmonic component (*A*/2). Below: logarithms of the amplitude distribution of the power spectra for artificial random sets in the (c) X-ray and (d) optical, used to estimate the significance levels. The example demonstrates determination of the 99.99% significance level.

Astronomy Observatory data [4]. The differences between the X-ray, optical, and radio periods are insignificant.

Figure 3b presents the *V*-band phase light curve after subtraction of the orbital period double wave. The phases were calculated using the elements

$$\text{Min} = \text{JD } 2449953 + 147^{\text{d}}.0E_1. \qquad (2)$$

The light curve has a broad maximum and a relatively narrow minimum. We can see in the figure, where various data sets are indicated, that the periodicity is confirmed in all fairly complete data sets. This period is also well represented in the other photometric bands.

The 50^{d} period detected in 1996 as the period of outbursts in ASM/RXTE data [21] and confirmed by a frequency analysis of 1996 optical and X-ray data [3] is not manifest in more recent X-ray and optical data. It might have been episodic, and may have been associated with the large 90-day soft X-ray outburst. On the

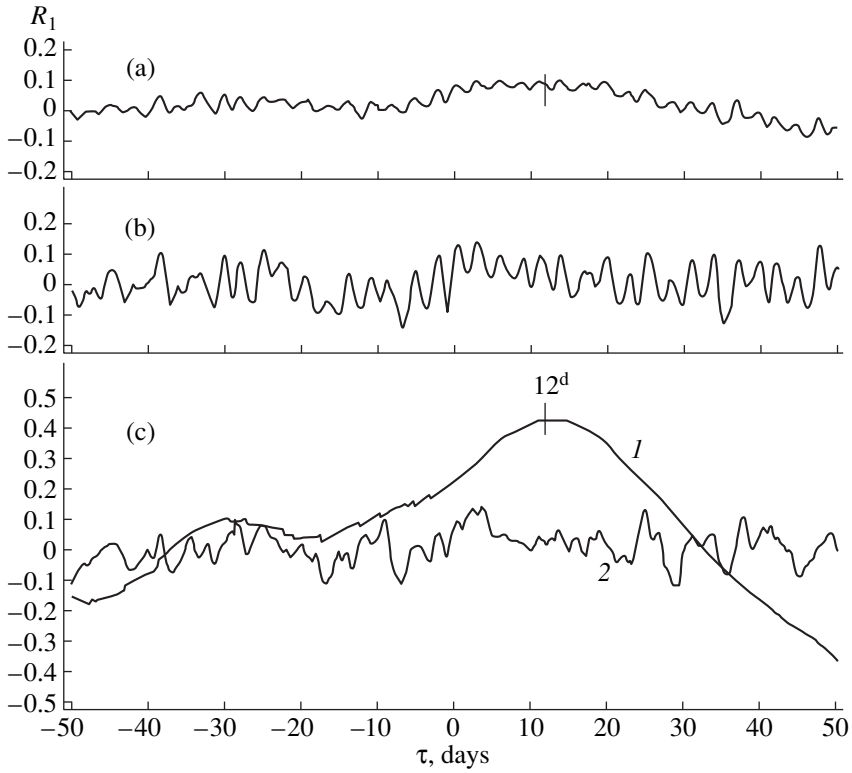

Fig. 8. Cross correlations between the X-ray and optical data, for (a) the initial data sets (X-ray data on a logarithmic scale), (b) orbital variability (all low-frequency components of the X-ray power spectrum with $A/2$ have been pre-whitened; $P > 20^d$ the initial optical dataset is given), (c) long-term variations (curve *1*, soft X-ray outburst excluded) and rapid variability (curve *2*, both data sets pre-whitened of all low-frequency components and the orbital wave).

other hand, our observations confirm that the peaks near $16\overset{d}{.}8$ and $14\overset{d}{.}8$ detected in the shorter dataset in [3] are stable. These variations in the power spectrum are of interest for a more specialized study.

5. CORRELATION BETWEEN X-RAY AND OPTICAL VARIATIONS OF CYG X-1

We used the data sets described above to study the correlation between the soft X-ray and optical radiation. Figure 8a presents the cross-correlation function for the initial data sets in stellar magnitudes. The correlation coefficients do not exceed 0.10, confirming the absence of a direct correlation between the X-ray and optical variations. For example, phenomena similar to the soft X-ray outbursts were not observed in the optical.

Nonetheless, the frequency analysis demonstrates that some relation exists, if for no other reason than because both light curves contain orbital components with appreciable amplitudes: $0\overset{m}{.}16$ and $0\overset{m}{.}045$ in the X-ray and optical spectra, respectively. We expect the correlation coefficients to be small even between the mean phase light curves, since these are not similar (a single wave with a narrow secondary minimum in the X-ray and a double wave with equal minima in the optical; Figs. 4a, 4b). However, correlation analysis is able to reveal the underlying relationship even in this case. For example, variations on a characteristic timescale (1–20 days) were distinguished in the X-ray light curve via a successive subtraction of low-frequency components of the power spectrum with $P > 20^d$ (see Fig. 8b). The cross-correlation function for the residual and the optical *V*-band dataset displays periodic oscillations with $P = 2\overset{d}{.}8$, half the orbital period. The maxima of the cross-correlation function occur at shifts τ for which the main minima of the X-ray light curve and alternating minima of the optical light curve coincide. The maximum value of the correlation function, 0.14, occurs for a shift of $2\overset{d}{.}8$. This indicates that even such a weak correlation can become physically significant when a large number of observations are included in the analysis. Nonetheless, it is of interest to estimate mathematically the significance of this value, corresponding to the probability of obtaining this value by chance if the optical light curve were random.

We used the same empirical technique described by Terebizh [13] that was previously applied to the power spectrum peaks to estimate the significance of the cross-correlation values. By randomly scrambling the values for the optical light curve (with fixed observing times), we constructed random functions that had the

same distributions of values and times as the real curve. For these functions, we then calculated a large number (tens of thousands) of correlation coefficients and studied the distribution of the cross-correlation functions. In this way, we found that the probability of obtaining the result $R_1(\tau) = 0.14$ (for $\tau = 2.8$, Fig. 8b) by chance is 0.5%, i.e., very small.

It is obvious that the X-ray and optical light curves are not similar. Nevertheless, it is of interest to try to trace the relationship between both rapid (within the scatter of points on the curves) and long-term X-ray and optical variations. This is especially true since a correlation between the long-term X-ray and optical variations with $R_1(\tau) = 0.63$ and a week shift between the light curves was detected in a relatively short series of observations [3]. Let us see if our more extended dataset can confirm this relation.

We calculated cross-correlation functions for two cases.

(1) Comparing medium-level, long-term variations at X-ray and optical wavelengths. Both residual sets were smoothened using a sliding average with smoothing interval 17^d and step $3\overset{d}{.}4$. Figure 8c (curve *1*) presents the result.

(2) Comparing relatively fast day-to-day variability at the two wavelengths. Both residual sets were prewhitened of all low-frequency components of the power spectrum with $P > 20^d$ (see Fig. 8c, curve *2*).

For the first case, we derived a correlation coefficient $R_1(\tau) = 0.43$, with the X-ray light curve lagging 12 ± 2 days relative to the optical light curve, with a significance level substantially exceeding 99.99%; this is similar to the results obtained in [3]. We were able to derive only a lower limit for the significance level, since, for 10^4 realizations of the cross-correlation function values for the random optical dataset, the maximum was as small as 0.20!

In the second case, the amplitude of the cross-correlation function is appreciably smaller, and the X-ray and optical ranges are related more weakly, if at all. For example, the amplitude for the local maximum of the function for a three-day shift (function 2 in Fig. 8c) does not differ from the maximum of the correlation for periodic components (Fig. 8b), and could be found by chance only with probability 0.4%.

Simulations with the observational data can provide a fresh look at the cross-correlation function for the initial X-ray and optical data (Fig. 8a). In spite of its low amplitude, this function contains information about all interconnections between the X-ray and optical variations, including orbital variability (the low-amplitude periodic component)! Separation of the large amount of observational data obtained during the CIS campaign and ASM/RXTE monitoring into different types and scales of variability enables determination of each type of correlation with high significance.

6. CONCLUSIONS

We have organized a unified dataset from a variety of initial optical observations of Cyg X-1 carried out during 1994–1998 at observatories of the CIS. We have compared our optical data with ASM/RXTE X-ray data available via the Web. The following conclusions can be drawn.

(1) In Cyg X-1 = V 1357 Cyg, the amplitudes of brightness variations and flares are not as high in the optical as they are at X-ray energies. The light curve has a double wave with the orbital period and an amplitude of $0\overset{m}{.}045$, outbursts and rapid low-amplitude variability with a characteristic timescale of one day, and decreases (or dips) in the brightness. Some intense rapid optical outbursts may be precursors for large X-ray flares.

(2) We have detected a secondary minimum of the X-ray orbital variability at phase 0.5 (lower conjunction of the X-ray source), whose origin remains unknown.

(3) In addition to the orbital period, the frequency analysis has revealed a secondary period of $147^d \pm 2^d$, which is half the previously known (precessional?) period of 294^d. The ASM/RXTE data in the quiescent state (excluding the large 1996 outburst) are dominated by the similar period $150^d \pm 2^d$. These X-ray and optical periods are also close to the radio period $142^d \pm 7^d$.

(4) Correlation analysis has revealed several types of correlations between the X-ray (2–10 keV) and optical variations of Cyg X-1. These are a strong dependence between slow variations of the mean brightnesses (with correlation coefficient $R_1 = 0.43$) and a weak dependence between the orbital variations (with coefficient $R_1 = 0.14$). We have determined the delay of the slow X-ray variability relative to the optical variations to be 12 days. All the derived relations are mathematically significant due to the large number of the observations. The correlation function of the initial observational data sets reflects all these types of correlations.

To facilitate the establishment of connections between the optical variations and variations in other spectral ranges, we have made our data available in electronic form. Given the clear importance of simultaneous coordinated observations of Cyg X-1 at various wavelengths for investigations of the behavior of matter and radiation in the vicinity of a relativistic black hole, we plan to continue this work. We have not considered a physical interpretation of the phenomena detected, and defer this to our subsequent studies.

ACKNOWLEDGMENTS

K.N. Grankin, O.V. Ezhkova, and S.Yu. Mel'nikov are grateful to V.B. Kondrat'ev for his help with the observations at Maĭdanak Observatory. V.P. Goranskiĭ and E.A. Karitskaya thank the Director of Tien-Shan Astronomical Observatory K. Kuratov and the observatory staff for their hospitality and allocation of observational time. The study was partially supported by the Min-

istry of Science of the Russian Federation (budget item "Optical Monitoring of Unique Astrophysical Objects"), the Russian Foundation for Basic Research (project code 98-06-17067), Astronomy (1.4.2.2), and the Program for Support of Leading Scientific Schools (grant 96-15-96489).

REFERENCES

1. A. Herrero, R. P. Kudritzki, R. Gabler, *et al.*, Astron. Astrophys. **297**, 556 (1995).
2. I. B. Voloshina, V. M. Lyutyĭ, and A. E. Tarasov, Pis'ma Astron. Zh. **23**, 335 (1997) [Astron. Lett. **23**, 293 (1997)].
3. E. A. Karitskaya, V. P. Goranskiĭ, K. N. Grankin, and S. Yu. Mel'nikov, Pis'ma Astron. Zh. **26**, 27 (2000) [Astron. Lett. **26**, 22 (2000)].
4. C. Brocksopp, R. P. Fender, V. M. Larionov, *et al.*, Mon. Not. R. Astron. Soc. **309**, 1063 (1999).
5. V. G. Kornilov and A. V. Krylov, Astron. Zh. **70**, 426 (1993) [Astron. Rep. **37**, 221 (1993)].
6. V. G. Kornilov, Balt. Astron. **7**, 513 (1998).
7. V. M. Lyutyĭ, Perem. Zvezdy **18**, 417 (1972).
8. E. N. Walker and A. R. Quintanilla, Mon. Not. R. Astron. Soc. **182**, 315 (1978).
9. V. P. Goranskij, E. A. Karitskaya, K. N. Grankin, and O. V. Ezhkova, Inf. Bull. Var. Stars, No. 4682 (1999).
10. G. Hill, R. W. Hilditch, and E. L. Pfannenschmidt, Publ. Dom. Astrophys. Obs. Victoria BC **15**, 1 (1976).
11. N. G. Bochkarev and V. M. Lyutyĭ, Pis'ma Astron. Zh. **24**, 330 (1998) [Astron. Lett. **24**, 277 (1998)].
12. C. Brocksopp, A. E. Tarasov, V. M. Lyuty, and P. Roche, Astron. Astrophys. **343**, 861 (1999).
13. V. Yu. Terebizh, *Analysis of Time Series in Astrophysics* [in Russian] (Nauka, Moscow, 1992).
14. V. V. Bruevich, N. N. Kilyachkov, R. A. Syunyaev, and V. S. Shevchenko, Pis'ma Astron. Zh. **4**, 544 (1978) [Sov. Astron. Lett. **4**, 292 (1978)].
15. E. A. Karitskaya and V. P. Goranskij, Inf. Bull. Var. Stars, No. 4404 (1996).
16. J. C. Kemp, M. S. Barbour, and R. E. McBirney, Astrophys. J. Lett. **244**, L73 (1981).
17. A. M. Cherepashchuk, Usp. Fiz. Nauk **166** (8), 809 (1996) [Phys. Usp. **39**, 759 (1996)].
18. T. J. Deeming, Astrophys. Space Sci. **36**, 173 (1975).
19. W. C. Priedhorsky, J. Terrell, and S. S. Holt, Astrophys. J. **270**, 233 (1983).
20. J. C. Kemp, E. A. Karitskaya, M. I. Kumsiashvili, *et al.*, Astron. Zh. **64**, 326 (1987) [Sov. Astron. **31**, 170 (1987)].
21. S. W. Zhang, B. A. Harmon, W. S. Paciesas, *et al.*, IAU Circ. No. 6462 (1996).

Translated by K. Maslennikov

Astronomy Reports, Vol. 45, No. 5, 2001, pp. 361–370. Translated from Astronomicheskiĭ Zhurnal, Vol. 78, No. 5, 2001, pp. 421–431.

The Structure of Shocks in the Atmospheres of Pulsating Stars

Yu. A. Fadeev

Institute of Astronomy, Russian Academy of Sciences, ul. Pyatnitskaya 48, Moscow, 109017 Russia

Received July 25, 2000

Abstract—The structure of shocks propagating through partially ionized hydrogen gas with characteristics typical of the atmospheres of RR Lyr, W Vir, and RV Tau type variables is analyzed in terms of a self-consistent solution of the equations of gas dynamics, atomic kinetics, and radiation transfer. The solutions were obtained for shock waves with velocities 20 km/s $\le U_1 \le$ 90 km/s and unperturbed hydrogen gas with temperatures 3000 K $\le T_1 \le$ 9000 K and density $\rho_1 = 10^{-10}$ g/cm^3. The fraction of the energy of the gas-dynamic flux converted into radiation increases with the shock amplitude, and the ratio of the radiation flux emitted by the shock to the gas kinetic energy flux is $0.4 \lesssim \mathcal{R} \lesssim 0.8$ for the velocities U_1 considered. This ratio also increases slightly with the ambient gas temperature T_1 due to an increase in hydrogen ionization in the radiative precursor. The flux emitted by the leading edge of the shock opposite to the gas flow is several percent higher than the flux emitted in the opposite direction by the trailing edge of the shock. Radiation is mostly concentrated in the Balmer continuum, and the region of efficient Lyman radiation transfer includes gas layers located near the viscous jump ($\delta X = \pm 10^4$ cm). The final gas-compression ratio in units of the limiting compression corresponding to an isothermal approximation is virtually independent of the shock amplitude, and increases with the unperturbed gas temperature from $r \approx 0.5$ at $T_1 = 3000$ K to $r \approx 0.9$ at $T_1 = 9000$ K. © *2001 MAIK "Nauka/Interperiodica".*

1. INTRODUCTION

Periodic shocks are among the most interesting gas-dynamical phenomena observed in the atmospheres of pulsating stars. The primary shock indicators are blue-shifted hydrogen emission lines. These features are often accompanied by split absorption lines, which are indicative of gas-velocity discontinuities. Shock effects are especially conspicuous in Population-II Cepheids [1–3], RV Tau pulsating variables [4, 5], and Mira variables [6–8].

Shocks constitute the main mass-loss mechanism in intermediate- and late-type pulsating giants. Periodic shocks can produce mass outflows into the circumstellar medium even when the gas velocity behind the viscous jump is less than the corresponding escape velocity [9]. An important consequence of periodic shocks is an increase of the gas density in the outer layers of the stellar atmosphere, providing favorable conditions for the condensation of dust particles [10]. This conclusion is supported by the results of various observations suggesting a close relationship between circumstellar dust shells and stellar pulsations.

The principal physical processes in shocks are qualitatively well understood, and a detailed description of shock morphology can be found in a number of monographs (see, e.g., [11–14]). At the same time, quantitative estimates of the fraction of the kinetic energy of the gas-dynamical flow lost to shocks via radiation remain rather uncertain. The more than modest success achieved with determining shock damping rates in stellar atmospheres is due to serious problems that arise when attempting to analyze dissipative processes (mainly dissociation of molecules and ionization of atoms) under conditions of non-local radiative heat transfer.

Atmospheres with effective temperatures $T_{\rm eff} >$ 3000 K consist primarily of atomic gas, and the main dissipative processes leading to shock damping (apart from radiative cooling) are due to the excitation and ionization of atoms. It follows that the structure of shocks propagating through the atmospheres of pulsating stars can be described by solutions of the equations of gas dynamics, atomic-level kinetics, and radiation transfer. Such systems of equations are difficult to solve because of the rigidity of the kinetics equation and the substantial (up to several orders of magnitude) difference of the gas opacities on either side of the Lyman continuum edge. These difficulties can be overcome by representing the gas-dynamical and atomic-kinetics equations with a system of ordinary differential equations, which are best adapted to solving rigid problems, and treating the radiation transfer as a boundary problem. The inter-relation between the gas-dynamical flow and the radiation field produced by this flow is accounted for iteratively, which admits, as shown in [15, 16], a converging and stable solution.

The results of computations of shock structures reported in our previous paper [16] were obtained for unperturbed gas with temperature $T_1 = 6000$ K and density $\rho_1 = 10^{-10}$ g/cm^3. However, since many astrophysical applications require that the shock properties be known

over wide temperature and density ranges, we report here the results of shock-structure computations for unperturbed gas with density $\rho_1 = 10^{-10}$ g/cm^3 and temperatures 3000 K $\le T_1 \le$ 9000 K. We will report results for different densities ρ_1 in a future paper. Note that the results presented below are based on a more detailed analysis of the radiation transfer than those in [16]. In particular, we extended the spectral interval on which the transfer equation is solved to $13 \le \log\nu \le 16$, and increased the total number of quadrature nodes to ≈900. We performed separate integrations over frequency ν in several spectral intervals with their monochromatic parameters varying continuously within each interval. The boundaries of these intervals are either ionization limits or the edges of line wings separated from the line center ν_0 by $\delta\nu = 5 \times 10^{-4}\nu_0$. We thus do not restrict our computations of the radiation transfer in spectral lines to their cores, as was done in [16], and allow for line wings described by Doppler broadening.

As in [15, 16], we analyze below the structure of shocks propagating through a partially ionized hydrogen gas. In this case, the solution is determined by three main parameters: the temperature T_1 and density ρ_1 of the unperturbed gas, and the shock velocity U_1 relative to the unperturbed gas. See [16] for the main equations and the methods used to solve them.

2. STEADY-STATE SHOCK MODEL

Shocks in the atmospheres of pulsating stars are nonstationary phenomena; however, the time scale for relaxation behind the viscous jump is much smaller than the time scale for variations of the parameters of the medium through which the shock propagates. This circumstance allows us to treat the shock structure as a steady-state feature, simplifying the problem considerably. In particular, the gas-dynamical and atomic-kinetics equations can be reduced to a system of ordinary differential equations, which are best adapted for solving the rigid Cauchy problem. A detailed discussion of the applicability of a steady-state approximation to shocks is presented by Zeldovich and Raĭzer [11].

The boundary problem for the radiation-transfer equation can be solved only in a limited interval of the spatial coordinate X, and we therefore model the shock as a plane-parallel layer co-moving with the wave. We take the spatial coordinates at the layer boundary to be X_1 and X_N, with gas flowing into the layer at X_1 and out of the layer at X_N. We put our coordinate origin $X = 0$ at the viscous jump, where the gas-dynamical parameters are discontinuous. The thickness of the viscous jump is only several particle mean free paths, and it can therefore be considered infinitely thin. To solve the radiation-transfer equation using the method of Feautrier [17], the entire interval $[X_1, X_N]$ is subdivided into $N - 1$ subintervals. The interval between adjacent grid points is smallest (ΔX = 1cm) in the vicinity of the viscous jump, and increases in accordance with a geometrical progression with distance from the jump. Small intervals near the viscous jump are required if we wish to distinguish the fastest relaxation processes; however, the optical depths of intervals beyond the Lyman continuum are so small that this often leads to a loss of accuracy if a standard Feautrier technique is applied. Therefore, we solved the transfer equation using the modified Feautrier method suggested by Rybicki and Hammer [18]. We carried out all our computations on a $1000 \le N \le 3000$ spatial grid. We performed integrations over the angular coordinate $0 \le \mu \le 1$ using Gaussian quadratures with $m = 8$ nodes.

To specify the boundary conditions for the transfer equation, we assumed that the radiation intensity $I_{\mu\nu}$ of the ambient gas was isotropic and Planckian at both layer boundaries:

$$\begin{aligned} I_{\mu\nu} &= B_\nu(T_1), \quad \mu > 0, \quad X = X_1, \\ I_{\mu\nu} &= B_\nu(T_1), \quad \mu < 0, \quad X = X_N, \end{aligned} \tag{1}$$

where $\mu = \cos\theta$ and θ is the angle between the gas flow velocity and the direction of propagation of the radiation intensity $I_{\mu\nu}$.

We solve the Cauchy problem for the equations of gas dynamics and atomic-level kinematics on the intervals $[X_1, X^-]$ and $[X^+, X_N]$, which correspond to the spatial regions in front of and behind the viscous jump. Here, X^- and X^+ are the points of the computation domain nearest to the viscous jump, at distances $\Delta X/2$ = 0.5 cm on either side of the jump. Our initial conditions for integrating the equations over the interval $[X_1, X^-]$ are the unperturbed temperatures T_1, densities ρ_1, and velocities U_1. The atomic-level populations n_i and degree of hydrogen ionization x_H at X_1 are computed using a statistical equilibrium approximation, so that these quantities include the effect of the non-equilibrium radiation field of the shock. The gas-dynamical variables in the vicinity of the viscous jump at X^+ and X^+ are related via the Rankine–Hugoniot equations, which enable us to derive the initial conditions at X^- required for the integration over $[X^+, X_N]$ from the parameter values at X^-. Integration of the system of ordinary differential equations and subsequent solution of the radiation-transfer equation for the entire shock constitute a single cycle of the iteration procedure. The iterations are repeated until the differences between ith and the $(i + 1)$th values of the gas-dynamical variables at each node of the difference-scheme grid become smaller than a specified threshold. The number of required iterations depends on the initial approximation, and ranged in our case from several dozen to several hundred. We used this convergence criterion in this way in order to maintain a constant total energy flux $\mathscr{C}_2$ up to a relative error of $\varepsilon(\mathscr{C}_2) \lesssim 10^{-2}$ throughout the model.

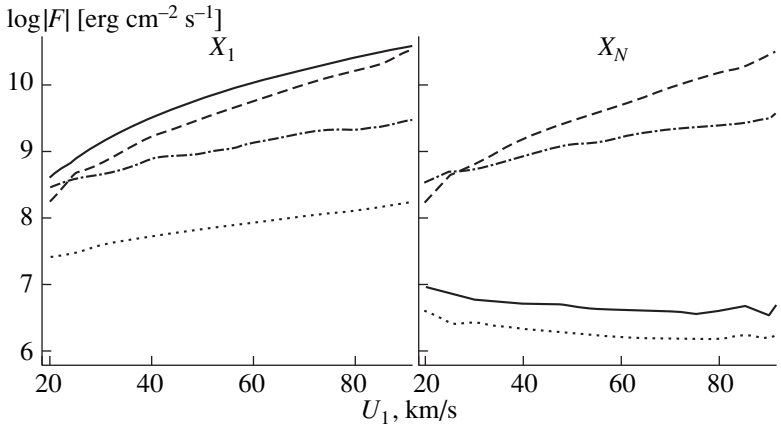

Fig. 1. Kinetic-energy flux F_K (solid), radiative flux $|F_R|$ (dashed), and total flux F_h (dash–dot) and $F_r = U(E_R + P_R)$ (dotted) at the boundary points X_1 (left) and X_N (right) as functions of the shock velocity U_1 for $\rho_1 = 10^{-10}$ g/cm^3 and $T_1 = 6000$ K.

3. STRUCTURE OF THE SHOCK

For shocks with radiative heat exchange, the Rankine–Hugoniot equations in the co-moving frame take the form [13, 19]

$$\rho U = \mathcal{C}_0 \equiv \dot{m}, \tag{2}$$

$$\dot{m}U + P_g + P_R = \mathcal{C}_1, \tag{3}$$

$$\frac{1}{2}\dot{m}U^2 + \dot{m}h + F_R + U(E_R + P_R) = \mathcal{C}_2, \tag{4}$$

where U is the gas flow velocity, E_R the total radiation energy density, F_R the radiation flux, and P_R the radiation pressure. Since the temperature of the heavy particles (ions and hydrogen atoms), T_a, can differ from that of the electrons, T_e, the formulas for the gas pressure P_g and specific enthalpy h must be written

$$P_g = n_{\rm H}kT_a + n_e kT_e \tag{5}$$

and

$$h = \frac{5}{2}\frac{n_{\rm H}}{\rho}kT_a + \frac{5}{2}\frac{n_e}{\rho}kT_e + \frac{\chi_{\rm H}}{\rho}\sum_{i=1}^{L}\left(1 - \frac{1}{i^2}\right)n_i + \frac{\chi_{\rm H}}{\rho}n_e, \tag{6}$$

where $n_{\rm H}$ is the total density of hydrogen atoms, n_i the density of hydrogen atoms in the ith level, n_e the density of free electrons, k the Boltzmann constant, $\chi_{\rm H}$ the ionization potential of hydrogen, and $L = 4$ the number of levels in the adopted model for the hydrogen atom.

We did not use the Rankine–Hugoniot equations (2)–(4) only to compute the gas-dynamical quantities behind the viscous jump at X^+. In the case of a planar geometry, the total energy flux $\mathcal{C}_2$ given by (4) is independent of the spatial coordinate, and variations of the kinetic-energy flux $F_K = \frac{1}{2}\dot{m}U^2$ are accompanied by corresponding variations of the thermal-energy flux $F_h = \dot{m}\,h$, radiation flux F_R, and the flux $F_r = U(E_R + P_R)$ associated with the energy and pressure of the radiation. Figure 1 shows the values of these quantities at the boundary points X_1 (left panel) and X_2 (right panel) for $T_1 = 6000$ K and $\rho_1 = 10^{-10}$ g/cm^3 as functions of the shock velocity relative to the unperturbed gas U_1. These plots show how the kinetic and thermal energy of the gas changes as a result of the passage of the shock. It is important that each term in (4) is a positive quantity, with the exception of the radiation flux, which can be negative at X_1. That is why we plot the absolute value $|F_R|$ in the left panel of Fig. 1. The relations shown indicate that, whereas the initial state of the gas-dynamical flow is characterized by a predominance of kinetic energy, the main contribution to the total energy flux behind the viscous jump is made by the thermal energy of the gas (enthalpy flux F_h) and radiation (flux F_R); the kinetic-energy flux F_K decreases by 1.5–4 orders of magnitude, depending on the shock velocity. The contributions of the radiation energy E_R and pressure P_R remain so small throughout the shock that F_r can be neglected.

The leading and trailing edges produce more or less equal radiation; i.e., the fluxes emerging from the boundary points X_1 and X_N are approximately (within a few percent) equal in absolute value: $-F_{R1} \approx F_{RN}$. A more detailed comparison of these quantities shows that, in all the models considered, the flux $|F_R|$ emerging from X_1 opposite to the gas flow is several percent higher than the flux emerging from X_N.

The conversion of the shock kinetic energy into radiation can be described in more detail by analyzing variations in the fluxes F_K, F_h, and F_R with the spatial coordinate X. Figure 2 shows the corresponding dependences for shocks propagating at velocities $U_1 = 30$ and 60 km/s with $T_1 = 6000$ K and $\rho_1 = 10^{-10}$ g/cm^3. We do not show plots for $F_r = U(E_R + P_R)$ because this quantity remains negligible for all X values. For clearer graphical presentation, we subdivide our shock model into

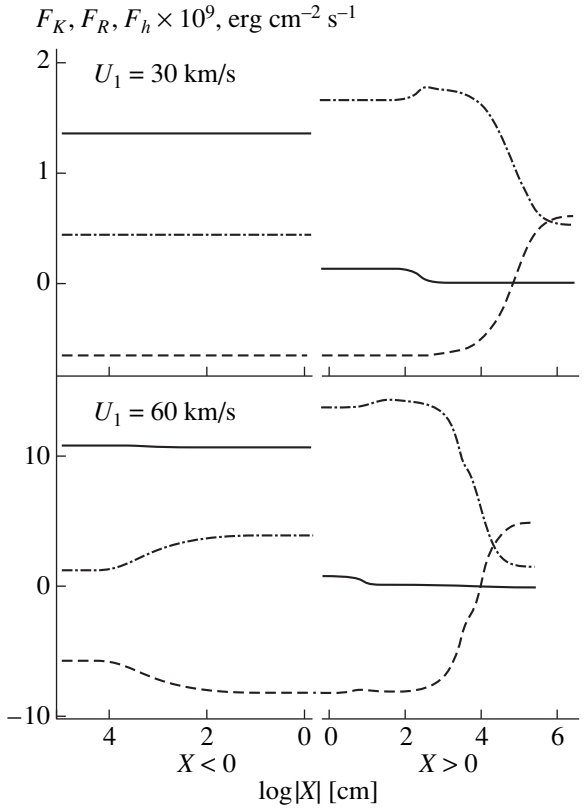

Fig. 2. Kinetic-energy flux F_K (solid), radiation flux F_R (dashed), and enthalpy flux F_h (dash–dot) as functions of distance $|X|$ from the adiabatic viscous jump for U_1 = 30 km/s (upper panel) and U_1 = 60 km/s (lower panel). The left and right parts of the plot correspond to the shock region in front of and behind the viscous jump, respectively.

two regions on either side of the viscous jump and use a logarithmic scale in X in each region.

3.1. Region of the Radiative Precursor

At temperatures $T_1 \lesssim 8000$ K, the hydrogen atom is predominantly in its neutral state, and the hydrogen gas is characterized by a large absorption coefficient in the Lyman continuum. Therefore, the change in the thermodynamical parameters in front of the viscous jump is due to the absorption of Lyman photons emitted in the shock region behind the viscous jump. The size of the precursor region is about ~10^4 cm for $\rho_1 = 10^{-10}$ g/cm^3. In this region, the gas temperature increases and hydrogen atoms become excited and ionized. Note that, throughout the entire precursor region, atomic transitions are associated exclusively with radiation processes, since the photo-excitation and photo-ionization rates are several orders of magnitude higher than the rates of electron-collisional excitation and ionization. The left panel in Fig. 3 shows variations in the degree of hydrogen ionization x_H in front of the viscous jump for shock velocities U_1 = 30 and 60 km/s.

In shocks with velocities $U_1 < 60$ km/s (Mach numbers $M_1 = U_1/a_1 < 6$, where a_1 is the adiabatic sound speed at X_1), variations of the enthalpy flux F_h in the region of the radiative precursor are almost fully compensated by the corresponding variations of the radiation flux F_R, and therefore have virtually no effect on the gas density ρ and flow velocity U. The interrelation between variations of F_h and F_R in front of the viscous jump is clearly traced in the lower panel of Fig. 2 for U_1 = 60 km/s.

When $U_1 > 60$ km/s, increase in the shock velocity changes substantially the gas density ρ in front of the viscous jump: when U_1 = 70 km/s, the relative gas density increase is $\Delta\rho/\rho_1 \approx 3\%$, whereas when U_1 = 90 km/s, the gas density increases by ≈10%. The increase of the gas density and decrease of its flow velocity in front of the viscous jump are associated with the strong dependence of the Lyman continuum flux on the shock amplitude, since the absorption of Lyman photons results in an increasingly strong rise of the electron temperature of the gas. For example, in a shock with velocity U_1 = 90 km/s, the temperature in front of the viscous jump can increase by as much as $\Delta T = T^- - T_1 \approx 4 \times 10^4$ K.

3.2. Viscous Jump

Deceleration of the gas-dynamical flow at the viscous jump is accompanied by an abrupt decrease in the kinetic energy flux at $X = 0$. Since the atomic-level populations, degree of ionization, and characteristics of the radiation field do not change in the viscous jump, the decrease in the kinetic-energy flux F_K is balanced by the increase of the enthalpy flux associated with the increase of the temperatures of the heavy particles T_a and electrons T_e (Fig. 2). The temperature of the heavy particles behind the viscous jump T_a^+ can be determined from the solution of the Rankine–Hugoniot equations (2)–(4):

$$T_a^+ = T_a^- + \frac{n_e^-}{n_H^-}(T_e^- - T_e^+) + \frac{1}{5}\frac{\dot{m}U^-}{n_H^- k}\left(1 - \frac{1}{\eta^2}\right) + \frac{2}{5}\frac{F_R^- - F_R^+}{n_H^- k U^-} + \frac{2}{5}\frac{E_R^- + P_R^- - (E_R^+ - P_R^+)/\eta^{-1}}{n_H^- k}, \quad (7)$$

where $\eta = \rho^+/\rho^-$ is the compression ratio and the "minus" and "plus" superscripts denote gas-dynamical variables at X^- and X^+ on either side of the viscous jump. Since we have not taken into account the effect of the electron thermal conductivity, the electron temperature at the viscous jump changes only as a result of adiabatic compression:

$$T_e^+ = \eta^{\gamma - 1} T_e^-, \quad (8)$$

where $\gamma = 5/3$ is the adiabatic index of the electron gas.

3.3. Relaxation Region

The shock region behind the viscous jump is usually treated as a relaxation layer, where individual degrees of freedom are excited on different relaxation time scales. In the case of a partially ionized hydrogen gas, these processes are equalization of the electron and heavy-particle temperatures T_e and T_a (the translational degree of freedom) and excitation and ionization of the hydrogen atoms. Note that the rates of electron-collisional excitation and ionization are negligible compared to the rates of the corresponding radiative transitions, so that all variations of the atomic states in the relaxation region are due primarily to photon processes.

The increase in the enthalpy flux F_h immediately behind the viscous jump ($X \lesssim 10^3$ cm for $U_1 = 30$ km/s and $X \lesssim 10$ cm for $U_1 = 60$ km/s) determines the boundaries of the region of thermalization where the temperatures T_e and T_a are equalized as a result of elastic collisions between electrons and ions/neutral atoms. A comparison of the plots F_h in the right-hand side of Fig. 2 for $U_1 = 30$ and 60 km/s shows that the size of the thermalization region decreases rapidly with the shock velocity. This is due to the fact that the energy exchange between the hydrogen atoms and electron gas is due mainly to elastic collisions between electrons and hydrogen ions, whose density in front of the viscous jump increases with the shock amplitude. The total radiation flux does not change significantly inside the thermalization region, and the increase of the electron temperature is accompanied by only a slight decrease in the gas flow velocity U.

At a somewhat larger distance from the viscous jump ($\log X > 2.5$ for $U_1 = 30$ km/s and $\log X > 2$ for $U_1 = 60$ km/s), the decrease in the enthalpy flux is accompanied by a corresponding change in the radiation flux, while the kinetic-energy flux remains approximately constant. This shock region is of the greatest interest, since it is here that mechanical energy initially stored in the form of thermal gas energy is converted into radiation energy. A comparison of the plots of the enthalpy flux F_h in Fig. 2 with those of the degree of ionization x_H in Fig. 3 indicates that the shock radiation flux forms mainly in the region of hydrogen recombination.

The excitation of atomic levels via radiative bound–bound transitions is approximately as rapid a process as equalization of the electron and heavy-particle temperatures, so that there is a rapid population of levels $i \geq 2$ behind the viscous jump. The density of excited hydrogen atoms n_i continues to increase until the decrease in the degree of ionization becomes appreciable. In the case of bound–free transitions, a much higher number of collisions is required; this means that hydrogen-ionization events occur much farther from the viscous jump, and the ionizational degree of freedom becomes frozen, resulting in a lower gas heat capacity and about a twofold increase in the gas density ρ. For instance, for shocks with velocity $U_1 = 60$ km/s, the compression ratio at the viscous jump is

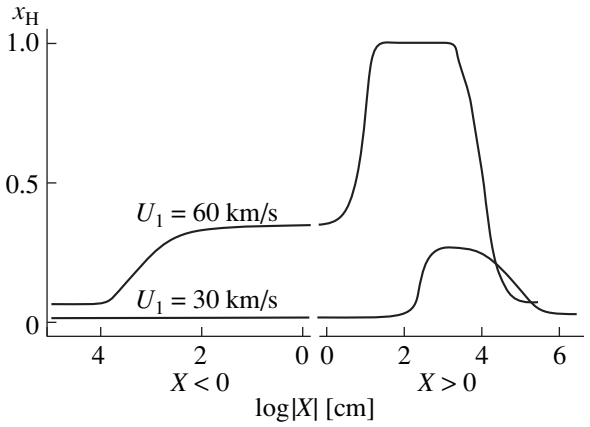

Fig. 3. Degree of hydrogen ionization x_H as a function of distance $|X|$ from the viscous jump for shock velocities $U_1 = 30$ and 60 km/s.

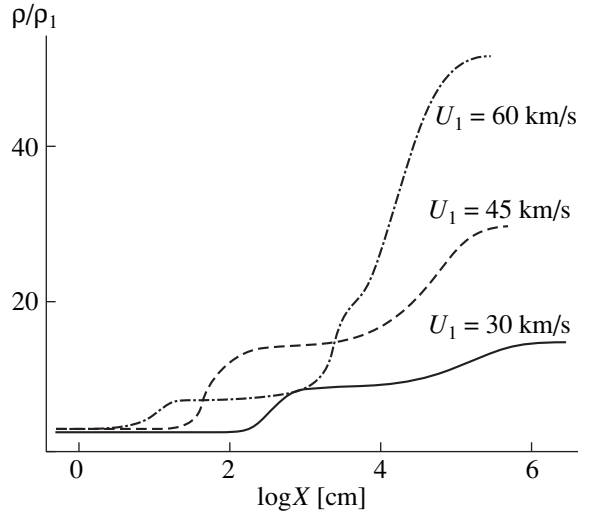

Fig. 4. Compression ratio ρ/ρ_1 behind the viscous jump for shock velocities $U_1 = 30$ km/s (solid), $U_1 = 45$ km/s (dashed), and $U_1 = 60$ km/s (dash–dot) for $\rho_1 = 10^{-10}$ g/cm^3 and $T_1 = 6000$ K.

$\rho^+/\rho^- = 3.6$ (the limiting compression ratio for a monoatomic gas is $\rho^+/\rho^- = (\gamma + 1)/(\gamma - 1) = 4$). In the region of excitation of the translational degree of freedom, the compression ratio before ionization increases to $\rho/\rho_1 \approx 9$ when $U_1 = 30$ km/s and to $\rho/\rho_1 \approx 8$ when $U_1 = 60$ km/s (Fig. 4). The compression ratio continues to increase even more farther from the viscous jump, in the region of radiative cooling of the gas, where variations of the hydrogen recombination lag behind those of the gas temperature. The final compression ratio lies in the range $10 \lesssim \rho/\rho_1 \lesssim 100$, and depends on the fraction of the total energy flux due to radiation; i.e., on the shock velocity U_1.

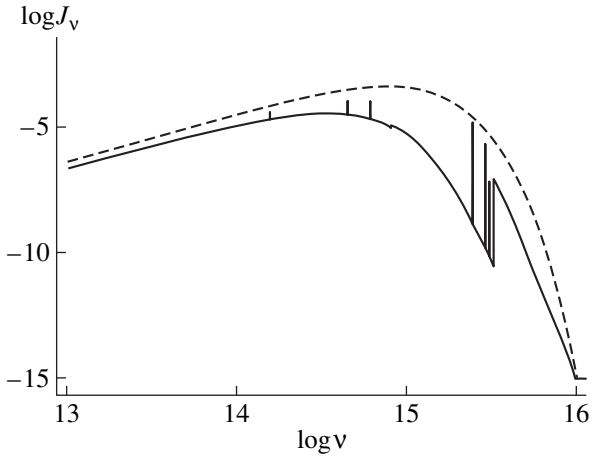

Fig. 5. Spectral dependence of the mean radiation intensity J_ν (solid) and local Planck function $B_\nu(T_e)$ (dashed) in the shock thermalization region for $T_1 = 6000$ K, $\rho_1 = 10^{-10}$ g/cm^3, $U_1 = 45$ km/s, and $X = 70.6$ cm.

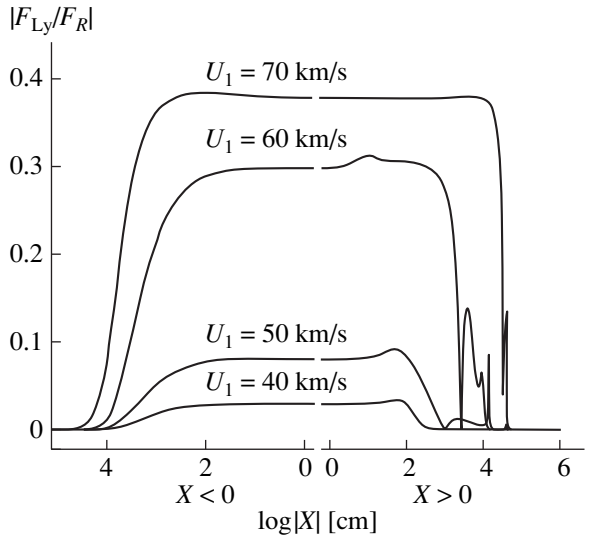

Fig. 6. Ratio of the radiation flux in the Lyman continuum F_{Ly} to the total radiation flux F_R as a function of the spatial coordinate X for shock velocities U_1 = 40, 50, 60, and 70 km/s for $\rho_1 = 10^{-10}$ g/cm^3 and $T_1 = 6000$ K.

4. RADIATION FIELD OF THE SHOCK

The radiation field produced by the shock is fairly far from equilibrium, and assuming thermal equilibrium should inevitably lead to errors in the computed radiative flux. Even at the boundary of the region of equalization of the heavy-particle and electron temperatures, deviations of the mean radiation intensity J_ν from the local Planck function $B_\nu(T_e)$ remain very important, making it impossible to use a Planck function to approximate the radiation field. To illustrate this, we plot in Fig. 5 the mean intensity J_ν as a function of frequency ν in the thermalization region behind the viscous jump for U_1 = 45 km/s. The large differences between the spectral dependences of J_ν and $B_\nu(T_e)$ are due to substantial departures of the atomic-level populations n_i and electron densities n_e from their equilibrium values.

The computation results we present here were obtained using a model for the hydrogen atom with $L = 4$ levels, and the spectral dependences of monochromatic quantities exhibit three Lyman lines (Lyα, Lyβ, and Lyγ), two Balmer lines (Hα and Hβ), and the Paα line (Fig. 5). The continuum spectrum presents the greatest interest, since this is where most of the radiation-energy transfer occurs. However, in spite of their insignificant contribution to the total energy transport, emission lines have a substantial effect on the atomic-level populations and overall ionization balance. Moreover, the computed spectral-line emission profiles can be compared with observations.

4.1. Radiation Transfer in the Continuum

Unlike steady-state stellar atmospheres, where the anisotropy of the radiation field is due to the predominance of photons propagating radially, the angular dependence of the radiation intensity $I_{\mu\nu}$ in a shock is determined to an appreciable degree by the finite geometric width of the layer $[X_1, X_N]$ in which the shock lies. Given a source function $S_\nu(\tau)$, in a planar geometry, the formal solution to the transfer equation relating the intensities at the boundary points X_1 and X_N has the form

$$I_{\mu\nu}(X_N) = I_{\mu\nu}(X_1)e^{-\Delta\tau_\nu/\mu} + \frac{1}{\mu}\int_0^{\Delta\tau_\nu} S_\nu(t)e^{-t/\mu}dt, \qquad (9)$$

where $\Delta\tau_\nu$ is the monochromatic optical depth of the layer $[X_1, X_N]$. The typical optical depth at the Lyman continuum boundary is $\Delta\tau_\nu \sim 10^4$. The optical depth of the layer at frequencies below the Lyman limit is $\Delta\tau_\nu \lesssim 10^{-2}$, and the second term on the right-hand side of (9) decreases rapidly as the direction changes from orthogonal ($\mu = 0$) to parallel ($\mu = \pm 1$) to the gas flow. As a result, the ratio of the moments of the transfer equation is equal to that for an isotropic radiation field ($K_\nu/J_\nu = 1/3$) only at Lyman continuum frequencies, while $K_\nu/J_\nu \approx 0.1$ beyond the Lyman continuum. Because of this strong anisotropy, a diffusion approximation for the transfer equation becomes unsuitable, and leads to substantial errors in the computed shock radiation field. We consider this circumstance to be very important, since most of the radiation flux transfer occurs at frequencies beyond the Lyman continuum, and the region of efficient radiation transfer in the Lyman continuum includes only gas layers closest to the viscous jump. Figure 6 shows the ratio of the Lyman continuum flux F_{Ly} to the total flux F_R in the vicinity of the viscous jump. The minimum of this

ratio is $|F_{Ly}/F_R| \sim 0.01$ for shock velocity $U_1 = 25$ km/s, and increases to $|F_{Ly}/F_R| \approx 0.38$ for $U_1 = 70$ km/s.

The increase of the ratio $|F_{Ly}/F_R|$ near the viscous jump is associated with the increase of the degree of hydrogen ionization and, consequently, to the decrease of the gas opacity in this region of the shock. When $U_1 = 75$ km/s, the hydrogen becomes almost fully ionized in the precursor region ($x_H^- \approx 0.98$), and the fraction of the Lyman continuum in the total flux reaches its limiting value. Further increase of the shock velocity leaves the maximum $|F_{Ly}/F_R|$ virtually unchanged, and only increases the size of the region of radiation transfer in the Lyman continuum.

As noted above, the total fluxes F_R emitted upstream and downstream of the shock are approximately equal. This is also true of the monochromatic fluxes at frequencies below the Lyman limit. However, the Lyman continuum flux is directed primarily opposite to the gas flow, with only a small fraction emitted in the opposite direction. The interaction between matter and radiation in the Lyman continuum is described by the divergence of the Lyman flux:

$$\nabla F_{Ly} = 4\pi \int_{\nu_1}^{\infty} (\eta_\nu - \kappa_\nu J_\nu) d\nu, \qquad (10)$$

where η_ν and κ_ν are monochromatic radiation and absorption coefficients and ν_1 is the threshold frequency for ionization of hydrogen from the ground level. We can see in Fig. 7 that $\nabla F_{Ly} < 0$ immediately behind the viscous jump, so that the electron temperature T_e increases not only due to elastic collisions with ions and neutral hydrogen atoms, but also due to the absorption of radiation in the Lyman continuum. The region of negative ∇F_{Ly} is bounded by layers where the degree of ionization increases considerably, resulting in a decrease of the opacity in the Lyman continuum.

The gas opacity is much lower outside the Lyman continuum, and radiation interacts with matter at a greater distance from the viscous jump. For comparison, Fig. 7 shows the divergence of the radiation flux between frequencies ν_1 and ν_2 corresponding to the thresholds for ionization from the first and second levels. It is evident that, at frequencies $\nu < \nu_1$, the region where gas interacts with radiation is almost two orders of magnitudes wider than at the Lyman continuum frequencies.

4.2. Radiation Transfer in Spectral Lines

Spectral lines account for only a small fraction of the total radiation flux; however, the contribution of lines increases rapidly with increasing shock velocity. For example, the maximum ratio of the Lyα flux to the total flux F_R behind the viscous jump in a shock with $U_1 = 30$ km/s does not exceed $\sim 10^{-6}$, but reaches $|F_{Ly\alpha}/F_R| \approx 0.03$ for $U_1 = 75$ km/s. This increase of the

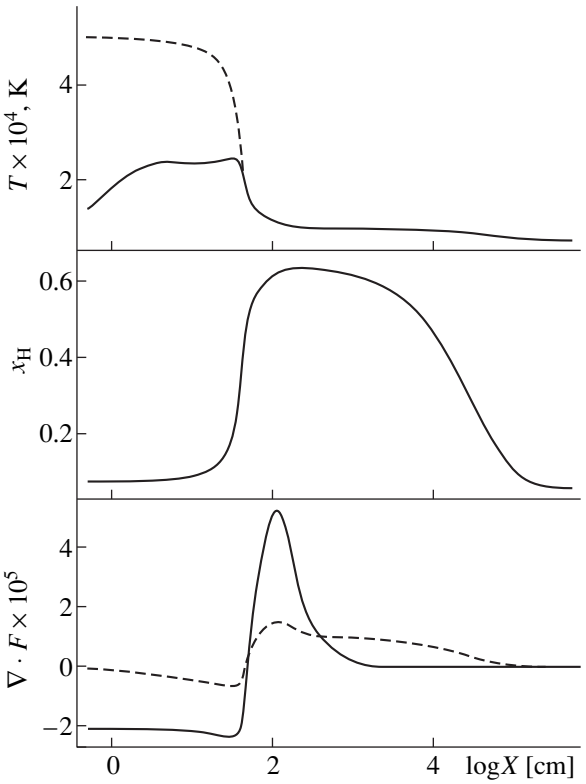

Fig. 7. Shock structure behind the viscous jump for $\rho_1 = 10^{-10}$ g/cm^3, $T_1 = 6000$ K, and $U_1 = 45$ km/s. Upper panel: electron temperature T_e (solid) and heavy-particle temperature T_a (dashed); center: degree of hydrogen ionization x_H; lower panel: divergence of the radiation flux in the Lyman (solid) and Balmer (dashed) continua.

line flux with shock velocity is due to the temperature dependence of the Doppler line width and the dependence of the temperature of the neutral atoms and ions behind the viscous jump on the compression ratio η, which is determined by the solution (7) of the Rankine–Hugoniot equations (2)–(4). Note here that these estimates give only upper limits to the line flux, since they include the continuum flux on which the lines are superimposed.

In the vicinity of the viscous jump, the monochromatic fluxes F_ν of spectral lines exceed significantly the continuum flux at the same frequency ν. Toward the edges of the shock regions, the gas temperature decreases and approaches its equilibrium value T_1; the Doppler line width decreases, and the line absorption coefficient increases. As a result, for each line, the monochromatic fluxes F_ν emerging from the boundary points X_1 and X_N have a wide emission profile superimposed on a narrow absorption line. This is most typical of the Lyman-series lines, which are characterized by large absorption coefficients at gas temperatures $T_1 < 8000$ K. The upper panel in Fig. 8 shows the spectral dependences of the monochromatic fluxes F_ν for the Lyα and Lyβ lines at the boundary point X_1, the point X^+ behind the viscous jump, and the

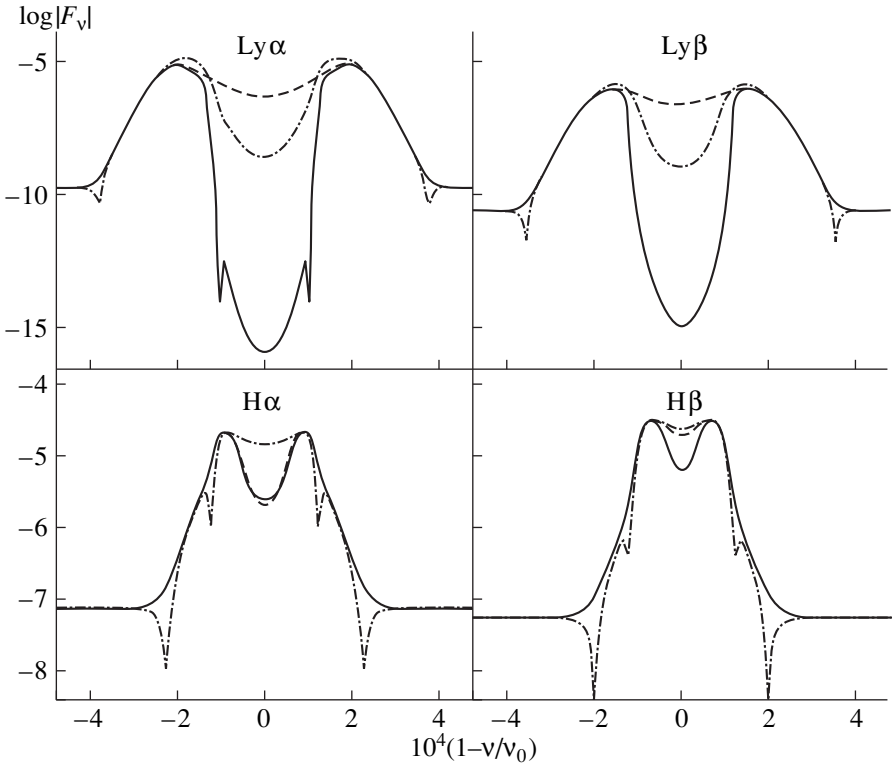

Fig. 8. Radiation flux in Lyα and Lyβ (upper panel) and Hα and Hβ (lower panel) at the leading boundary X_1 (solid), behind the viscous jump (dashed), and in the thermalization region (dash–dot) of the shock for $T_1 = 6000$ K, $\rho_1 = 10^{-10}$ g/cm^3, and $U_1 = 45$ km/s.

boundary of the thermalization region where $T_e \approx T_a$. The gas opacity is substantially lower at the Balmer-line frequencies, and these lines appear only in emission throughout the entire shock region (see lower panel in Fig. 8).

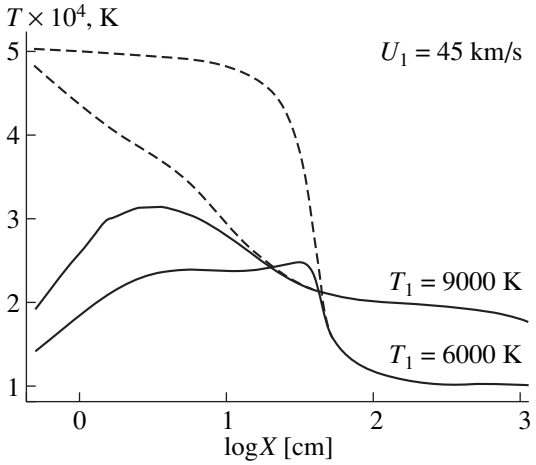

Fig. 9. Temperatures of the electrons T_e (solid) and of the hydrogen ions and neutral atoms T_a (dashed) as functions of distance from the viscous jump for $T_1 = 6000$ and 9000 K. The ambient gas density is $\rho_1 = 10^{-10}$ g/cm^3 and the shock velocity is $U_1 = 45$ km/s.

5. DEPENDENCE ON AMBIENT GAS TEMPERATURE

One of the most important features of shocks is the close inter-relation between the various shock regions, brought about by radiation. In particular, the geometrical size of the thermalization region is determined, to a considerable degree, by the degree of hydrogen ionization in front of the viscous jump, whereas ionization in the radiative-precursor region is governed by the radiation flux emitted by the gas behind the viscous jump. The inter-relation between the precursor region and the relaxation region is clearly traced when we consider the shock structures for different unperturbed gas temperatures T_1. Figure 9 shows the electron temperature T_e and hydrogen-atom temperature T_a as functions of distance from the viscous jump for two ambient gas temperatures T_1 for a shock with velocity $U_1 = 45$ km/s. When $T_1 = 6000$ K, the equilibrium degree of ionization of the unperturbed hydrogen gas is $x_H^* = 8.36 \times 10^{-3}$. As we approach the viscous jump, the degree of ionization increases, reaching $\bar{x}_H = 0.072$ in front of the jump. In a gas with $T_1 = 9000$ K, the equilibrium degree of hydrogen ionization is $x_H^* = 0.59$, and increases to $\bar{x}_H = 0.62$ in front of the viscous jump. Since the rate of energy exchange between electrons and hydrogen atoms behind the viscous jump is determined by elastic colli-

sions between electrons and hydrogen ions, the higher degree of ionization in front of the viscous jump when T_1 = 9000 K results in faster temperature equalization and, consequently, in a narrower thermalization region.

Thus, the temperature T_1 of the unperturbed gas in which the shock propagates affects substantially the structure of the shock, including the flux it emits. The results of computing the shock structure for various T_1 are summarized in the table, which also gives computed ratios of the radiation flux to the total kinetic-energy flux $\mathcal{R} = |F_R|/\frac{1}{2}\dot{m}U_1^2$ at the point of gas inflow into the shock (X_1) and the compression ratios ρ_N/ρ_1 at the gas-outflow point X_N. When the ambient gas temperature is T_1 = 6000 K, the velocity interval 20 km/s $\le U_1 \le$ 90 km/s corresponds to Mach numbers $2.2 \le M_1 \le 9.3$. The data in table clearly show that increasing the ambient gas temperature increases the fraction of the kinetic energy of the gas-dynamical flow that is converted into radiation. These variations are due to the increase of the degree of hydrogen ionization in front of the viscous jump, and become especially important when $T_1 > 7000$ K; i.e., for equilibrium degrees of ionization $x_H^* \gtrsim 0.2$.

It is evident from the table that the final gas compression ratio due to shocks with velocities 20 km/s $\le U_1 \le$ 90 km/s varies by more than an order of magnitude. These variations reflect the fact that the shock has a rather low optical depth at the frequencies at which the bulk of the radiative energy transfer occurs, making it possible to use an isothermal approximation with an upper limit to the gas compression ratio $(\rho_N/\rho_1)_{\rm lim} = \gamma M_1^2$ to describe the shock as a whole. Since the optical depth of the shock decreases with the equilibrium degree of ionization x_H^* of the hydrogen gas, the isothermal approximation becomes increasingly suitable at higher unperturbed gas temperatures T_1. The computations show that the ratio $r = (\rho_N/\rho_1)/(\rho_N/\rho_1)_{\rm lim}$ depends only slightly on the shock velocity U_1, and varies from $r \approx 0.5$ when T_1 = 3000 K to $r \approx 0.9$ when T_1 = 7000 K.

Ratio of radiative to kinetic energy flux $\mathcal{R} = |F_R|/\frac{1}{2}\dot{m}\,U_1^2$ at X_1 and the final compression ratio ρ_i/ρ_1 as a function of shock velocity U_1 and the unperturbed gas temperature T_1 for $\rho_1 = 10^{-10}$ g/cm^3

U_1, km/s	T_1, K						
	3000	4000	5000	6000	7000	8000	9000
	$\mathcal{R}$, ρ_N/ρ_1						
20	0.36	0.40	0.44	0.45			
	7.99	7.82	7.28	6.64			
30	0.44	0.46	0.48	0.48	0.52	0.76	
	16.7	16.4	15.8	14.8	13.8	12.4	9.53
40	0.49	0.48	0.49	0.51	0.54	0.60	0.76
	30.2	28.1	26.3	24.9	20.9	17.6	16.0
50	0.51	0.49	0.49	0.49	0.50	0.56	0.69
	46.1	41.7	38.0	36.4	33.0	31.5	26.7
60	0.55	0.54	0.52	0.54	0.54	0.58	
	62.2	58.6	54.1	51.1	47.8	42.6	
70	0.63	0.62	0.60	0.60	0.62		
	81.4	78.2	71.5	65.9	61.1		
80	0.69	0.69	0.65	0.66	0.68		
	96.1	95.8	87.3	82.9	76.0		
90	0.85	0.81	0.85	0.85			
	114	114	110	102			

6. CONCLUSIONS

Our computational results reproduce the main feature of shocks—conversion of the kinetic energy of a gas-dynamical flow into radiation. Our self-consistent solution of the equations of gas dynamics, atomic-level kinetics, and radiative transfer allows quantitative estimation of the radiation flux emitted by the shock. On the whole, we conclude that the non-equilibrium radiation field that develops in a shock has a significant effect on gas cooling behind the viscous jump. This follows both from the rather high ratios $\mathcal{R} = |F_R|/F_K$ and from the fact that the final gas-compression ratio is close to its limiting value $(\rho_N/\rho_1)_{\rm lim}$, determined by an isothermal approximation. However, the isothermal approximation obviously overestimates the shock damping rates at unperturbed gas temperatures $T_1 \le 6000$ K. The typical shock velocities in Miras and W Vir pulsating variables are $U_1 \sim 50$ km/s [7] and $60 \lesssim U_1 \lesssim 90$ km/s [3], respectively. These values correspond to ratios $\mathcal{R} \sim 0.5$ and $0.5 \lesssim \mathcal{R} \lesssim 0.8$ for Miras and Population-II Cepheids, respectively, while the final compression ratio is $\rho_N/\rho_1 \lesssim 0.8\ (\rho_N/\rho_1)_{\rm lim}$. More definitive conclusions about the role of radiative losses in shocks can be obtained by computing models covering a wide range of unperturbed gas densities ρ_1. Such computations are much more time consuming, and we plan to report these results in a forthcoming paper.

The theoretically computed monochromatic fluxes F_ν in spectral lines are of considerable interest from the viewpoint of plasma diagnostics and comparison of theoretic models with observations. The hydrogen-line profiles shown above in Fig. 8 are based on a detailed solution of the transfer equation, but neglect the Doppler effect. Solving the transfer equation in this case is much more difficult, due to the angular dependence of the absorption and radiation coefficients. We will use the models developed in this paper as initial approximations in future computations including the effect of Doppler shifts in photon frequencies.

Tables of the main gas-dynamical variables as functions of the spatial coordinate X for shocks with various T_1, ρ_1, and U_1 can be obtained from the author.

ACKNOWLEDGMENTS

I am very grateful to N.N. Chugaĭ for a number of valuable comments made while preparing this paper. This work was supported by the Russian Foundation for Basic Research (project code 98-02-16734).

REFERENCES

1. H. A. Abt, Astrophys. J., Suppl. Ser. **1**, 63 (1954).
2. G. Wallerstein, Astrophys. J. **127**, 583 (1958).
3. G. Wallerstein, Astrophys. J. **130**, 560 (1959).
4. R. Scott and S. R. Baird, Publ. Astron. Soc. Pac. **94**, 850 (1982).
5. S. R. Baird, Publ. Astron. Soc. Pac. **96**, 72 (1984).
6. L. A. Willson, Astrophys. J. **205**, 172 (1976).
7. M. W. Fox, P. R. Wood, and M. A. Dopita, Astrophys. J. **286**, 337 (1984).
8. D. Gillet, Astron. Astrophys. **192**, 206 (1988).
9. L. A. Willson and S. J. Hill, Astrophys. J. **228**, 854 (1979).
10. Yu. A. Fadeyev, Lect. Notes Phys. **305**, 174 (1988).
11. Ya. B. Zel'dovich and Yu. P. Raĭzer, *Physics of Shock Waves and High-Temperature Hydrodynamic Phenomena* (Fizmatgiz, Moscow, 1963; Academic, New York, 1966, 1967), Vols. 1, 2.
12. I. A. Klimishin, *Shock Waves in Stellar Envelopes* [in Russian] (Nauka, Moscow, 1984).
13. D. Mihalas and B. W. Mihalas, *Foundations of Radiation Hydrodynamics* (Oxford Univ. Press, New York, 1984).
14. A. L. Velikovich and M. A. Liberman, *Physics of Shock Waves in Gases and Plasmas* [in Russian] (Nauka, Moscow, 1987).
15. Yu. A. Fadeyev and D. Gillet, Astron. Astrophys. **333**, 687 (1998).
16. Yu. A. Fadeyev and D. Gillet, Astron. Astrophys. **354**, 349 (2000).
17. P. Feautrier, C. R. Acad. Sci. Paris **258**, 3189 (1964).
18. G. B. Rybicki and D. G. Hummer, Astron. Astrophys. **245**, 171 (1991).
19. R. E. Marshak, Phys. Fluids **1**, 24 (1958).

Translated by A. Dambis

Astronomy Reports, Vol. 45, No. 5, 2001, pp. 371–381. Translated from Astronomicheskiĭ Zhurnal, Vol. 78, No. 5, 2001, pp. 432–443.

Interpretation of the Light Curve of the Eclipsing Binary V444 Cyg on the Set of Convexo-Concave Functions

I. I. Antokhin and A. M. Cherepashchuk

Sternberg Astronomical Institute, Universitetskiĭ pr. 13, Moscow, 119899 Russia

Received June 15, 2000

Abstract—The narrow-band λ4244 Å continuum light curve of the eclipsing binary V444 Cyg, which has a Wolf–Rayet component, is interpreted assuming that the brightness distribution and absorption in the WN5 star's disk are monotonic, non-increasing, convexo-concave, non-negative functions. The convex and concave parts of these functions correspond to the core of the WN5 star and its extended photosphere and atmosphere, respectively. The radius and brightness temperature of the opaque core of the WN5 star are $r_{\rm WN5}^{\rm core} \simeq 4R_\odot$ and $T_{\rm br}^{\rm core} > 52\,000$ K, respectively. The stellar wind is characterized by an accelerated radial outflow. Acceleration of the wind persists at large distances from the center of the star. A crude Lamers-law fit to the reconstructed velocity field in the wind yields an acceleration parameter β = 1.58–1.82. © *2001 MAIK "Nauka/Interperiodica".*

1. INTRODUCTION

Wolf–Rayet (WR) stars are helium remnants of evolved massive stars with initial masses of several tens of solar masses. The WR stage is only a brief episode in the life of a massive star. However, these objects play a key role in our understanding of the evolution and internal structure of massive stars, because they offer a combination of unique physical characteristics that make them valuable for comparisons of theoretical predictions with observations. One of the distinguishing features of WR stars are their powerful winds (with mass loss rates as high as $\sim 10^{-4} M_\odot$/yr), whose origin remains incompletely understood. Their dense winds make it very difficult to determine the physical parameters of the central cores of WR stars.

One possible approach to overcoming this problem is to construct adequate self-consistent models of a WR wind to be used as a sort of "transfer function" linking the hot core and observed external properties (e.g., spectra). In recent years, considerable advances have been made in this direction (see, e.g., [1, 2] and references therein). The so-called "standard model" of WR stellar winds is able to explain all the important spectral characteristics of these objects. However, a number of problems remain unsolved. This is partially due to the lack of a fully self-consistent model that includes gas-dynamical computations and solution of the transfer equations. In the standard model, only the transfer equations are solved, and a simple analytic formula is used to describe the kinematic structure of the wind.

Another approach is to try to obtain the maximum possible number of observational constraints with the minimum number of model assumptions. The eclipsing binary V444 Cyg (WN5 + O6, $P \simeq 4\overset{\rm d}{.}2$) provides a unique opportunity to analyze the structure of the extended wind of a Wolf–Rayet star in this type of approach. The binary has a high orbital inclination ($i \simeq 80°$), so that the stellar system exhibits deep eclipses, allowing the companion of the WR star (an O6 star) to be used as a test body.

In this paper, we implement this second approach. Our observational data are a λ4244 Å rectified narrow-band optical continuum light curve of V444 Cyg. We apply an algorithm for solving inverse problems on the compact set of convexo-concave, non-increasing, non-negative functions to the integral equations describing the light curve. These equations belong to the class of so-called ill-posed problems, and can be solved under certain *a priori* assumptions about the unknown functions. Earlier, we have solved the same problem on other compact sets (non-increasing, non-negative functions [3, 4] and non-increasing, non-negative, concave functions [5]). As we show below, *a priori* assumptions that the unknown functions $I_c(\xi)$ and $I_a(\xi)$ describing the brightness distribution and absorption properties in the disk of the WN5 star are concave-convex and monotonic are more specific and physically justified compared to assumptions adopted previously. The *a priori* information used here enables us to take into account more accurately specific features of the model for the WR star and its extended atmosphere. As a result, analysis of the eclipse light curve enables reconstruction of the structure of the inner parts of the WR stellar wind and, in particular, of the velocity field of the radial mass outflow.

1063-7729/01/4505-0371$21.00

2. FORMULATION OF THE PROBLEM

The light curve of an eclipsing binary with a component with an extended atmosphere can be described by the following set of integral and algebraic equations [3, 6]:

$$1 - l_1(\theta) = \int_0^{R_a} K_1(\xi, \Delta, r_{O6}) I_0 I_a(\xi) d\xi, \quad (1a)$$

$$1 - l_2(\theta) = \int_0^{R_c} K_2(\xi, \Delta, r_{O6}) I_c(\xi) d\xi, \quad (1b)$$

$$I_0 \pi r_{O6}^2 \left(1 - \frac{x}{3}\right) + \int_0^{R_c} I_c(\xi) 2\pi\xi d\xi = 1. \quad (1c)$$

Here, $1 - l_{1,2}(\theta)$ is the observed loss of light in the primary and secondary minima; θ the angle of relative rotation of the components, which is related to the separation Δ between the centers of their disks via the formula $\Delta^2 = \cos^2 i + \sin^2 i \sin^2\theta$ (the radius of the relative orbit and the total out-of-eclipse luminosity of the components are taken to be unity); r_{O6} the radius of the O6 star; I_0 the central brightness of the disk of this star; i the orbital inclination; $x = 0.3$ (for λ4244 Å) the limb-darkening coefficient for the O6-star disk; R_a and R_c quantities dominating the full radii of the eclipsing and emitting extended photospheres of the WN5 star, respectively; and $K_1(\xi, \Delta, r_{O6})$ and $K_2(\xi, \Delta, r_{O6})$ functions describing the disk overlap region during eclipse (the corresponding formulas can be found in [3, 6]). We assume that both binary components are spherical. $I_c(\xi)$ and $I_a(\xi)$ are unknown functions. See [3] for a detailed description of the problem.

Using the result for the function $I_c(\xi)$ obtained by solving (1), and setting the effective temperature of the O6 star to be $T = 40\,000$ K, in accordance with its spectral type, we can determine the central brightness temperature of the WN5-star disk, which characterizes the temperature of its core (i.e., the WR star proper). Note that this quantity is independent of interstellar extinction, since the O6 star serves as a comparison star and the method used is differential (see [3, 4, 6] for details).

On the other hand, the function $I_a(\xi)$ can be used to reconstruct the distribution of the absorption coefficient and the velocity law in the extended photosphere of the WN5 star. In fact, $I_a(\xi) = 1 - e^{-\tau(\xi)}$, where $\tau(\xi)$ is the line-of-sight optical depth of the extended atmosphere:

$$\tau(\xi) = 2\int_\xi^{R_a} \frac{\alpha(r) r dr}{\sqrt{r^2 - \xi^2}}, \quad (2)$$

where $\alpha(r)$ is the absorption coefficient in the extended atmosphere as a function of the distance r from the center of the WR star. Equation (2) is an Abelian integral equation with the unknown function $\alpha(r)$. Since scattering by free electrons is the main absorption mechanism in the optical continuum, the electron-density distribution can be derived from $\alpha(r)$:

$$n_e(r) = \frac{\alpha(r)}{\sigma_T}, \quad (3)$$

where $\sigma_T \simeq 7 \times 10^{-25}$ cm^2 is the Thomson scattering cross section. Since helium can be considered fully ionized in the inner parts of the WN5-star wind (see, e.g., [1, 2]), we can now determine the distribution of the total mass density $\rho(r)$ in this wind:

$$\rho(r) = 2 m_p n_e(r), \quad (4)$$

where $m_p = 1.7 \times 10^{-24}$ g is proton mass (we assume that the medium consists entirely of helium). We then use the continuity equation for the radial mass outflow in the WR wind to derive the unknown velocity distribution $v(r)$:

$$v(r) = \frac{\dot{M}_{WR}}{4\pi r^2 \rho(r)}, \quad (5)$$

where $\dot{M}_{WR}$ is the mass-loss rate of the WR star. A mass-loss rate $\dot{M}_{WN5} \simeq 7 \times 10^{-6} M_\odot$/yr was derived for V444 Cyg based on observations of the rate of increase of the binary period [7, 8] and linear polarization variations at optical wavelengths [9]. At the same time, we emphasized that the mass-loss rate indicated by radio continuum observations is about a factor of three higher. This discrepancy is most likely due to clumpy structure of the WR wind [10]. Obviously, the numerical values of $\alpha(r)$ and $v(r)$ depend on the absolute separation between the components ($a \simeq 38 R_\odot$) and the mass-loss rates adopted. To avoid this dependence, when solving problems (1) and (2), we always expressed distances in units of the component separation; i.e., we take the majorants of the radii R_a and R_c to be unity. In addition, we transform Eq. (5) into the dimensionless form

$$\frac{v(r)}{v_0} = \frac{r_0^2 \alpha_0}{r^2 \alpha(r)}, \quad (6)$$

where r_0 is the radius of the optical-continuum opaque core of the WR star observed when the disk is face-on. This radius is determined by the condition $\tau(\xi = r_0) = 1$, $\alpha_0 \equiv \alpha(r_0)$, $v_0 \equiv v(r_0)$; r_0 exceeds the hydrostatic core radius r_c.

We now have a number of observational data that make it possible to obtain more reliable results when interpreting the light curve.

(1) New spectropolarimeric observations of V444 Cyg [11] have shown that depolarization at the frequencies of emission lines depends strongly on orbital phase. This indicates that the depolarization is primarily due to the small separation between the binary components (tidal deformation of the outer parts of the WN5-star wind, effects due to the collision of the winds

of the two components, etc.). The fact that the depolarization vanishes at least at some orbital phases leads us to conclude that the inner part of the WN5 stellar wind in the V444 Cyg system emitting and absorbing in the continuum must be spherical.

(2) The independent spectrophotometric estimate of the component luminosity ratio in V444 Cyg derived by Cherepashchuk *et al.* [12] enables more reliable interpretation of the light curve and, in particular, derivation of the geometrical parameters r_{O6} and i (see below).

Note also that modern powerful computers enable much more efficient implementations of algorithms for solving inverse problems on compact sets of functions than was possible in our earlier works [3, 6], enabling analysis of solutions of the inverse problem of light-curve interpretation in more detail.

3. ALGORITHM FOR SOLUTION OF THE INVERSE PROBLEM ON THE SET OF CONVEXO-CONCAVE, NON-INCREASING, AND NON-NEGATIVE FUNCTIONS

The first two formulas in (1) are Fredholm equations of the first kind, which are well known [6] examples of so-called ill-posed problems. The same is true of the Abelian equation (2). It is well known that such problems cannot be solved without invoking some *a priori* information about the behavior of the unknown function, parametrization of the problem being the simplest example. For example, if both components in the binary are main-sequence stars with thin atmospheres, we can use linear limb-darkening laws for the functions $I_c(\xi)$ (which is precisely what we do for the O6 star), and the function $I_a(\xi)$ can be set equal to unity and zero at $\xi \le r_0$ and $\xi > r_0$, respectively. Such assumptions reduce (1) to classical equations in the theory of eclipsing variables.

Unfortunately, in the case of Wolf–Rayet stars, we have very little information about the behavior of the unknown functions. It goes without saying that $I_c(\xi)$ cannot be approximated by a linear limb-darkening law. Neither can we use the simple approximation for $I_a(\xi)$ mentioned above, due to the semi-transparent nature of the WR-star photosphere. As a result, only two alternatives remain: we can either compute the unknown functions in terms of some photospheric model for the WR component and then infer the parameters of this model by comparing the theoretical and observed light curves, or we can try to extract the maximum possible useful information from the observed light curve applying a minimum of model assumptions. Both the first (see, e.g., [13–15]) and the second [3–6] approaches have been employed in various studies.

This paper is based on the second approach. It is well known [16] that, if considered on a compact set of functions, an inverse problem is well-posed in the classical sense, and can therefore be solved using standard methods. The problem can thus be formulated as follows: which minimum *a priori* assumptions about the unknown functions would make (1) and (2) well-posed in the classical sense? Goncharskiĭ *et al.* [6] and Tikhonov [16] showed that these assumptions can be very general. This minimum set of assumptions is the following.

(1) The problem is spherically symmetric. Note that, in principle, we can do without this assumption, and, e.g., consider elliptical configurations. However, assuming that the photosphere of the WN5 component is spherically symmetric drastically simplifies the algorithm. We consider this assumption to be justified in the optical continuum region (see above).

(2) The unknown functions are monotonic, non-increasing, and non-negative.

It is these assumptions that we used in [3, 4, 6]. The resulting approximation proved to be quite suitable for determining some important physical parameters of the WN5 star (e.g., its core radius or brightness temperature). However, it was not sufficient for reconstruction of the spatial structure of the photosphere of the WN5 star and the velocity distribution in the stellar wind, since the unknown function was "too" flexible. As a rule, the unknown functions reconstructed assuming fixed observational errors exhibited step-like behavior. At the same time, it follows from (2) that a horizontal step in $I_a(\xi)$ *increases* $\alpha(r)$ in the corresponding distance interval. In other words, such behavior implies that large-scale inhomogeneities should be present in the stellar wind of the WR star, in contradiction with observations. Of course, WR stellar winds are known for their clumpiness (see, e.g., [2, 10]); however, the scale lengths of wind irregularities are much smaller than the size of the extended atmosphere of the WR star ($\sim 20 R_\odot$). Moreover, in addition to the fact that the clumpy structure of the wind occur on small scales, it is nonstationary.

Imposing more stringent *a priori* constraints on the unknown functions makes the resulting algorithms much more complicated. Antokhin *et al.* [5] interpreted the light curve of V444 Cyg using a compromise model, in which $I_a(\xi)$ was assumed to be a concave[1] and monotonically non-increasing, non-negative function when $\xi > r_0$ and equal to unity when $\xi \le r_0$, with r_0 a free parameter of the problem. The function $I_c(\xi)$ was still considered to be monotonically non-increasing and non-negative. The *a priori* requirement that $I_a(\xi)$ be concave imposes more stringent constraints and prevents the appearance of step-like behavior in the approximate solution.

Figure 1 compares the results of solving the inverse problem of interpreting the $\lambda 4244$ Å light curve on the class of non-negative, monotonically non-increasing functions with the solutions obtained on the class of concave, non-negative, monotonically non-increasing functions (adopted from [5]), with fixed fractional luminosity of the WN5 component (see below). It is evident that the $I_c(\xi)$ and $I_a(\xi)$ functions reconstructed on the set of non-

[1] Here we correct the unfortunate typographical error in [5]: the set $\breve{M}\downarrow$ should be referred to as a set of concave and not of convex functions.

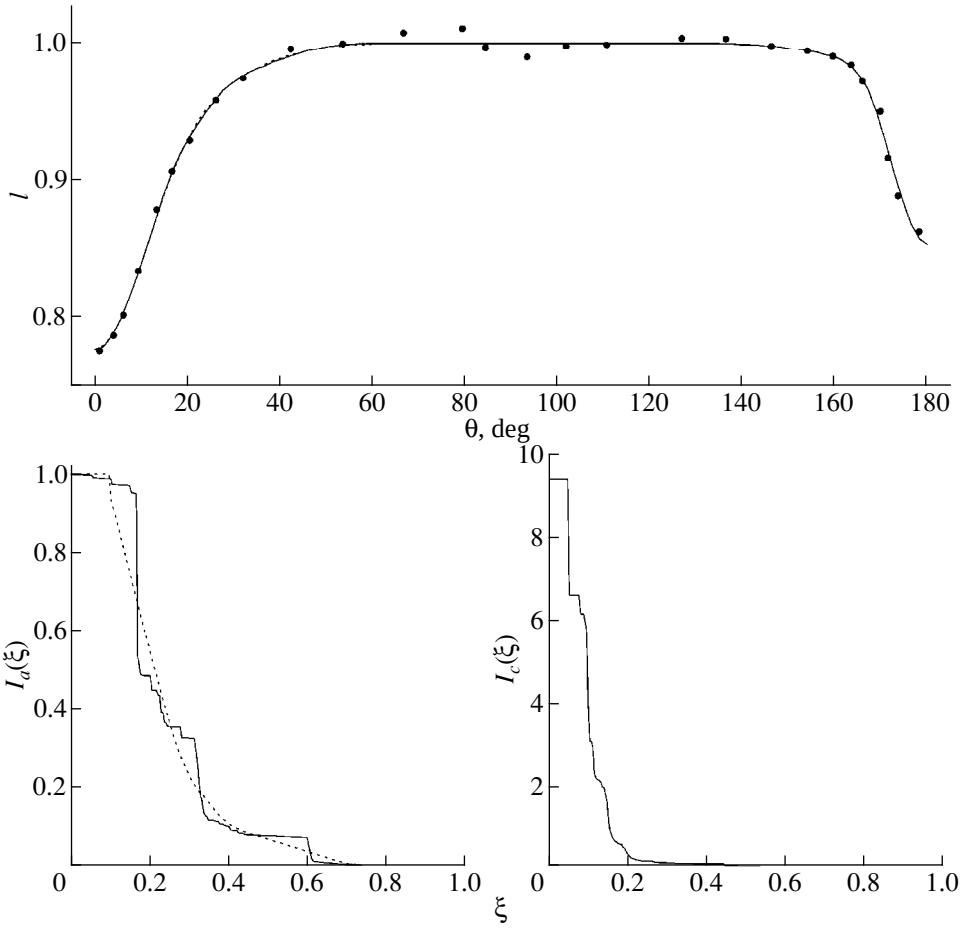

Fig. 1. Results of solving the inverse problem of interpreting the λ4244 Å light-curve on the set of non-negative, non-increasing functions (solid curve) and concave functions (for the primary minimum, dashed curve). The theoretical light curves are virtually indistinguishable. The data are taken from [5]. The observed light curve is given in relative intensities.

increasing, non-negative functions exhibit step-like behavior. Reconstructing $I_a(\xi)$ on the set of concave, non-increasing, non-negative functions yields better results. However, in this case, we impose a first derivative discontinuity at point r_0 on function $I_a(\xi)$.

Here, we interpret the light curve of V444 Cyg in a model in which both $I_c(\xi)$ and $I_a(\xi)$ are convexo-concave, monotonically non-increasing, non-negative functions. The convex parts of these functions correspond to the core of the WR star, which contains most of the star's mass, whereas the concave parts correspond to the star's extended photosphere and atmosphere. The position of the inflection point is a free parameter of the inverse problem. Using such *a priori* information makes it possible to more fully take into account specific features of the model of the WR star and its extended atmosphere. This enables reconstruction of the structure of the inner parts of the WR wind and, in particular, the velocity field of the radial mass outflow, via analysis of the eclipse light curve.

In addition to $I_c(\xi)$ and $I_a(\xi)$, the unknown parameters of the problem include r_{O6} and i. The parameter I_0 is derived from the normalization condition (1c). The presence of only two independent geometrical parameters in the problem allowed us to find a solution by simply running through possible values of these parameters. This ensures that our solution corresponds to the global and not a local minimum of the residual functional.

In a discrete approximation on an n-dimensional grid, the compact set of convexo-concave, monotonically non-increasing functions $\tilde{M}\downarrow$ is defined by the system of inequalities

$$\tilde{M}\downarrow = \left\{ z \in R^n: \begin{array}{l} z_1 \geq 0 \\ z_1 \geq z_2 \\ z_{i-1} - 2z_i + z_{i+1} \leq 0, \\ \quad i = 1, \ldots, k-1 \\ z_{i-1} - 2z_i + z_{i+1} \geq 0, \\ \quad i = k+1, \ldots, n-1 \\ z_{n-1} \geq z_n, \quad 1 < k < n \\ z_n \geq 0. \end{array} \right. \tag{7}$$

When solving (1a), we impose the additional constraint $z_1 = 1$ on z. For the sake of simplicity, we introduce operator notation for the right-hand sides of (1a) and (1b): $A_1\mathbf{z}$ and $A_2\mathbf{z}$, where $\mathbf{z}$ is a vector representing a discrete approximation of $I_a(\xi)$ or $I_c(\xi)$. Let us denote the set of observables $1 - l_{1,2}(\theta)$ for various orbital phases θ by the vectors $\mathbf{u}_1$ and $\mathbf{u}_2$. The solution algorithm for problem (1) can then be written as follows.

(1) We solve (1b) for each parameter pair (r_{O6}, i) by minimizing the residual functional $\Phi_2 = \|A_2\mathbf{z}_2 - \mathbf{u}_2\|^2_{l_2}$ for various values of k (the index of the inflection point). This yields the best-fit function $I_c(\xi)$ and value of k.

(2) We find I_0 from (1c) using the function $I_c(\xi)$ found in the previous step.

(3) Step 1 is repeated for the residual functional at the primary minimum $\Phi_1 = \|A_1\mathbf{z}_1 - \mathbf{u}_1\|^2_{l_2}$. Although, broadly speaking, the inflection-point index can be determined independently, here we have an obvious physical constraint on this parameter: the width of the section of $I_a(\xi)$ where this function is equal to unity (the opaque core) must correspond to the characteristic width of $I_c(\xi)$. We therefore based our inflection-point solution for the primary minimum on this constraint.

These computations yielded values of the residual functional on the two-dimensional grid of r_{O6} and i values, the corresponding best-fit functions $I_c(\xi)$ and $I_a(\xi)$, and the inflection-point indices.

In the metric l_2, the functionals Φ_1 and Φ_2 are equal to the sum of the squared differences between the theoretical and observed light curves. We introduced weighting factors to allow for the different accuracies of the normal points of the light curve. For convenience, we normalized the functionals to the sum of the weights, so that $\eta_{1,2} = \sqrt{\Phi_{1,2}}$ can be directly compared to the characteristic observational error of the normal point of the λ4244 Å light curve, which is equal to $\delta \approx 0.004$ in intensity units. The operators $A_{1,2}$ are linear, so that the functionals Φ_1 and Φ_2 are quadratic in the metric l_2 and therefore have easily computable derivatives. Such functionals can be minimized under the constraints (7) using the powerful technique of conjugate-gradient projection. A detailed description of this technique can be found, e.g., in [6]. We used a 200-point grid in ξ on the interval 0–1.

We solved problem (2) on the set of concave functions, in the same way as we did in [5].

4. RESULTS OF SOLVING THE INVERSE PROBLEM

We used the same rectified λ4244 Å continuum light curve of V444 Cyg as in our previous papers [3–5]. Figure 2 shows the surface of the sum of the residuals at the primary and secondary minima $\eta_1 + \eta_2$. The flat portion of the residual surface corresponds to the region $\cos i > r_{O6}$, where the O6-star disk does not overlap with the center of the disk of the WN5 star, so that the model is underdetermined. We therefore did not perform model computations in this domain. See [6] for a more detailed discussion of the limits of applicability of the adopted model. Note that the χ^2 test cannot be used for statistical estimation of the significance level of our model, since the interdependence of the parameters (7) makes

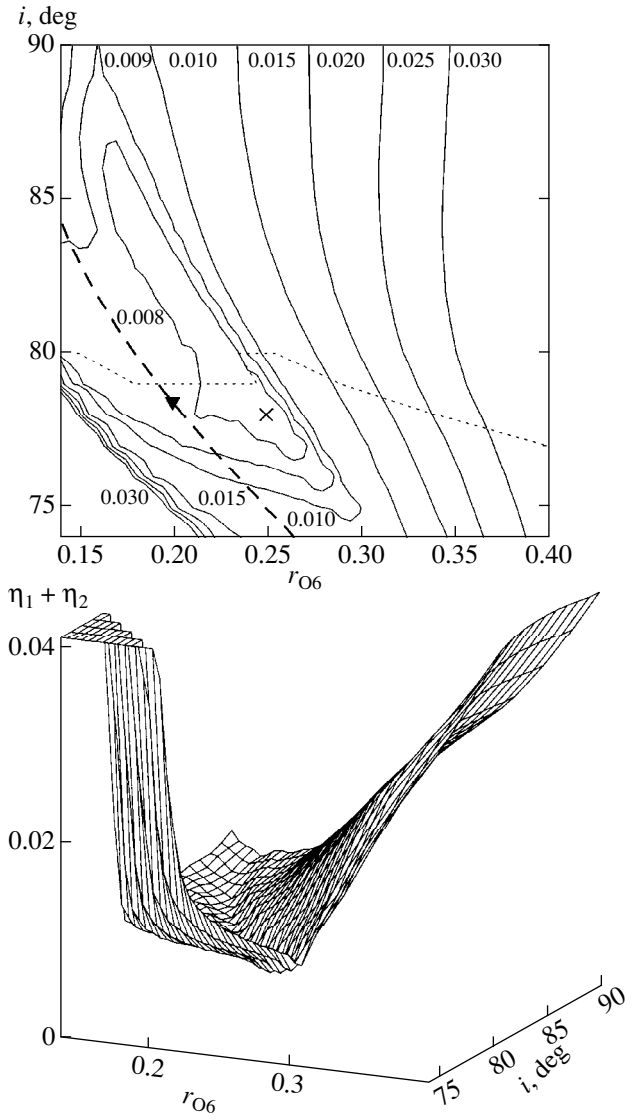

Fig. 2. Surface of the total residual $\eta_1 + \eta_2$ for the solution obtained on the set of convexo-concave functions. The upper panel shows contours of the surface. The cross shows the solution corresponding to the absolute minimum of the total residual. The thick dashed line in the upper panel corresponds to fixed relative luminosity of the WN5 component, $L_{WN5} = 0.38$. The triangle indicates the best-fit solution for this luminosity. The thin dashed line separates the region where the core of the WN5 component is opaque (below) from the region where it is semi-transparent (see text).

Parameters of V444 Cyg and the WN5 star reconstructed from solution of the rectified λ4244 Å continuum light curve

Parameter	Parameters corresponding to the fixed observed L_{WN5} = 0.38 Å	Parameters corresponding to the absolute minimum of the total residual $\eta_1 + \eta_2$
$\eta_1 + \eta_2$	0.0087	0.0067
L_{WN5}	0.38 (fixed)	0.20 (derived from light-curve solution)
r_{O6}	$0.20(7.6R_\odot)$	$0.25(9.5R_\odot)$
r_{WN5}^{core}	$\sim 4R_\odot$	$(2–3)R_\odot$
T_{br}^{core}	52000 K	230000 K (>70000 K)
n	0.94	1.45
β	1.82	1.58

r_{WN5}^{core} is the radius of the opaque core of the WR star; T_{br}^{core} is the brightness temperature of the core of the WN5 star computed assuming that the effective temperature of the O6 star is 40 000 K.

it impossible to reliably estimate the number of degrees of freedom. Agreement between the model and observations can therefore be assessed only indirectly, from the total residual. For a model to be (subjectively) considered feasible, this residual $\eta_1 + \eta_2$ must be about double the characteristic error of the light-curve normal point (i.e., 0.008).

The obvious way to identify the best-fit model is from the absolute minimum of the total residual. However, the corresponding solution proved to be inconsistent with the observed luminosity ratio for the components [12]. It is not entirely clear what gives rise to this discrepancy: defects of the adopted model or errors in the observed component luminosity ratio. In the total spectrum of the binary, the absorption lines of the O6 component are weak, and also overlap with emission lines of the WN5 star, making determination of the component luminosity ratio a very difficult problem. In view of this, we analyze two possible solutions: that determined by the absolute minimum of the residual and another based on the observed component luminosity ratio. The model parameters corresponding to these two solutions are summarized in the table. It is noteworthy that the two solutions yielded qualitatively similar reconstructed stellar-wind patterns and core parameters for the WR star.

4.1. Solution for the Absolute Minimum of the Total Residual

The total residual reaches its absolute minimum $(\eta_1 + \eta_2)_{min} = 0.0067$ when $r_{O6} = 0.25$ and $i = 78\overset{\circ}{.}0$ (indicated by the cross in Fig. 2). The corresponding relative luminosity of the WN5 component[2] is $L_{WN5} = 0.2$. The values of r_{O6} and i are close to those found in [3], confirming the results obtained in [4]. Note that, in these papers, the λ4244 Å light curve was interpreted assuming that $I_c(\xi)$ and $I_a(\xi)$ were monotonically non-increasing, non-negative functions. Thus, the geometrical parameters indicated by the absolute minimization of the total residual are the same when different types of *a priori* information about the unknown functions are adopted. We also wish to emphasize that the absolute minimum of the total residual yields not only r_{O6} and i, but also the relative luminosity of the WN5 star $L_{WN5} = 2\pi\int_0^1 I_c(\xi)\xi d\xi = 0.2$. Figure 3 shows the functions $I_c(\xi)$ and $I_a(\xi)$ found on the set of convexo-concave, monotonically non-increasing, non-negative functions and the corresponding absolute minimum of the total residual.

It is evident from the upper panel of Fig. 2 that the contour corresponding to a total residual of $h = 0.008$ encompasses a considerable portion of the plane of the geometrical parameters (r_{O6}, i). This implies fairly low accuracy for the values of these parameters found from the absolute minimum of the total residual alone. However, we can further restrict the allowable domain of r_{O6}, i by taking into account the fact that the WN5 component should have an opaque core. The *a priori* constraints (7) do not require the existence of a flat section $I_a(\xi) = 1$ at small ξ. It is nevertheless evident that $I_a(\xi)$ must be equal to unity when ξ is smaller than the opaque core's radius. It follows from the theory of the internal structure of massive hot stars (see, e.g., [17]) that the core radius of a WR star is about $2R_\odot$. The thin dashed line in Fig. 2 separates the region where $I_a(\xi) = 1$ at least for $\xi < 0.05$ ($\sim 2R_\odot$) from the region where the core of the WN5 component is semi-transparent (i.e., $I_a(\xi)$ becomes smaller than unity at a distance $\xi < 0.05$ from the center of the WN5-star disk). The core opacity condition is satisfied in the region *below* the dashed line, enabling us to further restrict the domain of possible r_{O6}, i.

[2] The ratio of its luminosity to the total luminosity of the system.

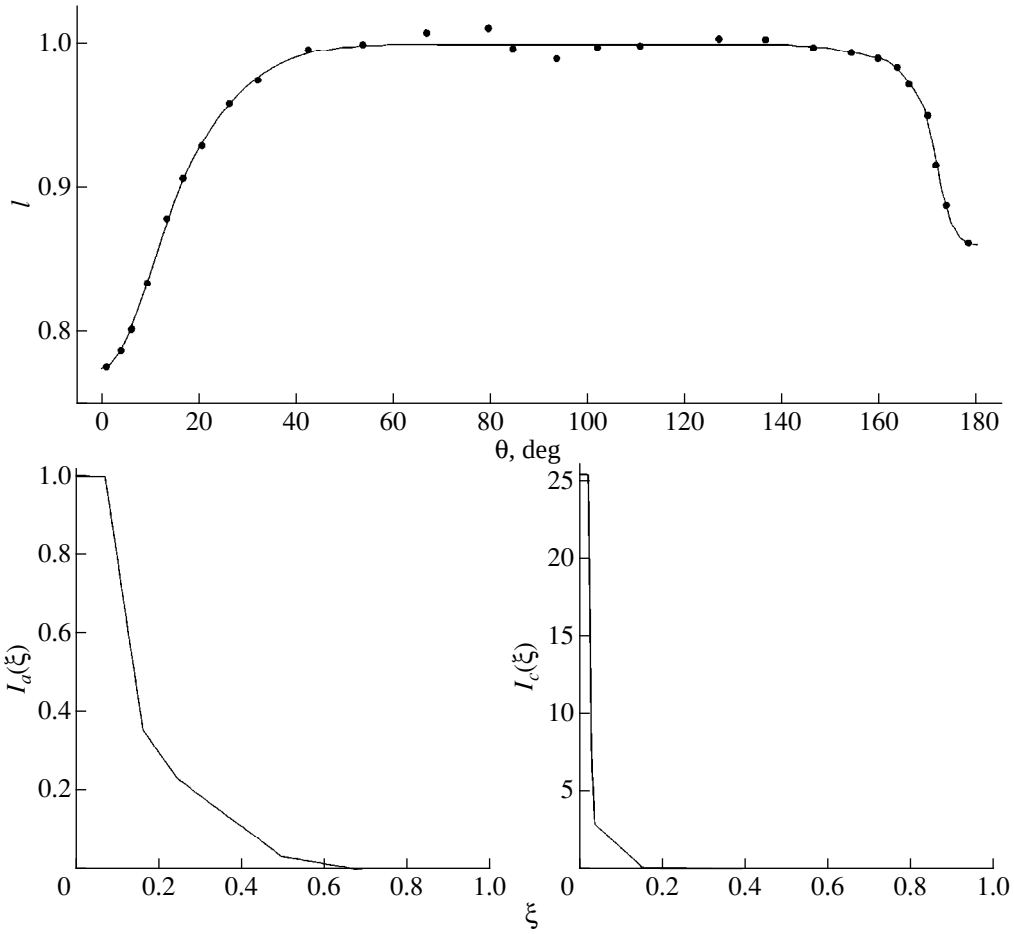

Fig. 3. Solution of inverse problem (1) on the set of convexo-concave, non-increasing, non-negative functions corresponding to the absolute minimum of the total residual. The upper panel shows the observed and theoretical λ4244 Å light curves.

4.2. Solution Corresponding to the Observed Relative Luminosity of the WN5 Component

Cherepashchuk *et al.* [12] determined the relative luminosity $L_{WN5} = 0.38$ of the WN5 component in the V444 Cyg system based on spectrophotometric observations of the binary. The solutions corresponding to this luminosity are shown in Fig. 2 by the bold dashed line. The minimum of the total residual $\eta_1 + \eta_2$ along this curve (indicated by a triangle) is equal to 0.0087, and corresponds to $r_{O6} = 0.20$ and $i = 78^\circ.43$. Figure 4 shows the functions $I_c(\xi)$ and $I_a(\xi)$ corresponding to this case.

Figure 2 shows clearly how important it is to use any independent information that can impose additional constraints on the choice of the possible solutions. The constraint imposed by requiring that the WN5 star possesses an opaque core appreciably reduces the domain of possible geometrical parameters. If known, the relative luminosity of the WN5 component can further constrain the values of these parameters.

4.3. Absolute Parameter Values

Given the absolute separations between the components and the mass-loss rate of the WN5 star, formulas (3)–(5) can be used to derive the absolute distributions $v(r)$ and $n_e(r)$. Here, we give the values of these functions at r_0. We assume that the separation between the components is $38R_\odot$ and that $\dot{M} = 0.7 \times 10^{-5} M_\odot$/yr [18, 19]. We have $r_0 = 0.076$ ($\sim 2.9R_\odot$), $n_e(r_0) = 1.1 \times 10^{13}$ cm^{-3}, $v(r_0) = 230$ km/s and $r_0 = 0.105$ ($\sim 4.0R_\odot$), $n_e(r_0) = 1.0 \times 10^{13}$ cm^{-3}, $v(r_0) = 132$ km/s for the first and second models, respectively. The radial optical depths at r_0 are $\tau^{rad}(r_0) = 0.68$ and $\tau^{rad}(r_0) = 0.84$ for the first and second models, respectively.

5. VELOCITY FIELD IN THE WN5 WIND

As was shown in Section 2, function $I_a(\xi)$ enables reconstruction of the spatial distribution of the absorption coefficient $\alpha(r)$ via solution of Eq. (2). We searched for $\alpha(r)$ on the set of concave, monotonically non-increasing, non-negative functions. We took the left-hand boundary of the ξ grid to be the first point

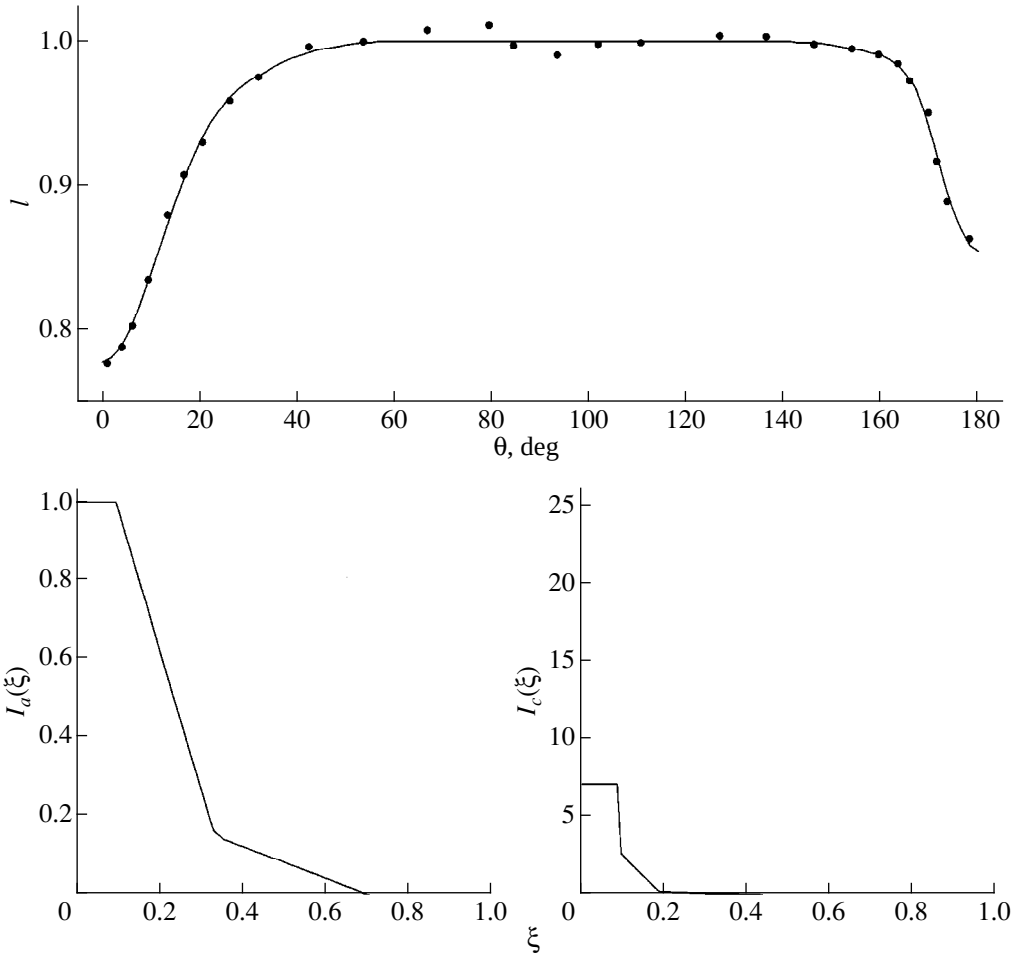

Fig. 4. Same as Fig. 3 for the solution for fixed relative luminosity of the WN5 component, $L_{\mathrm{WN5}} = 0.38$.

where $I_a(\xi)$ became less that unity. The same point determines the quantity r_0, which we adopt as our estimate for the radius of the WN5-star core, which is opaque in the optical continuum (when the disk is viewed face-on).

Figure 5 shows two solutions for this equation, corresponding to the two solutions of problem (1). We checked these solutions using (2) and (1a) and functions $\alpha(r)$ to compute the theoretical light curves, which are also shown in the figure. The residuals of the two solutions are $\eta_{1,\,\mathrm{Abel}} = 0.0043$ and $\eta'_{1,\,\mathrm{Abel}} = 0.0043$; i.e., they exceed only slightly the corresponding residuals obtained by solving equation (1a): $\eta_1 = 0.0036$ and $\eta'_1 = 0.0042$.

The dots in Fig. 6 show the functions $v(r)/v_0$ for the two solutions of (2). At very small $\tau(r)$, the error of $v(r)/v_0$ can exceed the velocity itself, and we therefore did not compare the velocity distribution at distances greater than that at which the *radial* optical depth becomes 0.08. The behavior of the reconstructed function $\tau_{\mathrm{rad}}(r)$ becomes irregular at smaller $v(r)/v_0$. It is clear that, in both cases, the WN5 wind absorbing in the continuum exhibits, on average, accelerated outflow, supporting our previous conclusion in [4]. The nonmonotonic behavior of the velocity distribution could be due to the errors of the observed light curve. The effect of these errors on the reconstructed velocity field can be rather important, since the function $\alpha(r)$ used to derive the velocity field is computed by solving two ill-posed problems in succession: the Fredholm integral equation (1a) and the Abelian integral equation (2).

Figure 6 shows the results of parametric rms approximations of the dimensionless functions using the Lamers law

$$v(r) = v_\infty\left(1 - \frac{r_c}{r}\right)^\beta \qquad (8)$$

(where r_c is the hydrostatic core radius of the WR star and v_∞ is the terminal wind velocity) and the power-law relation

$$v(r) = v_0\left(\frac{r}{r_0}\right)^n. \qquad (9)$$

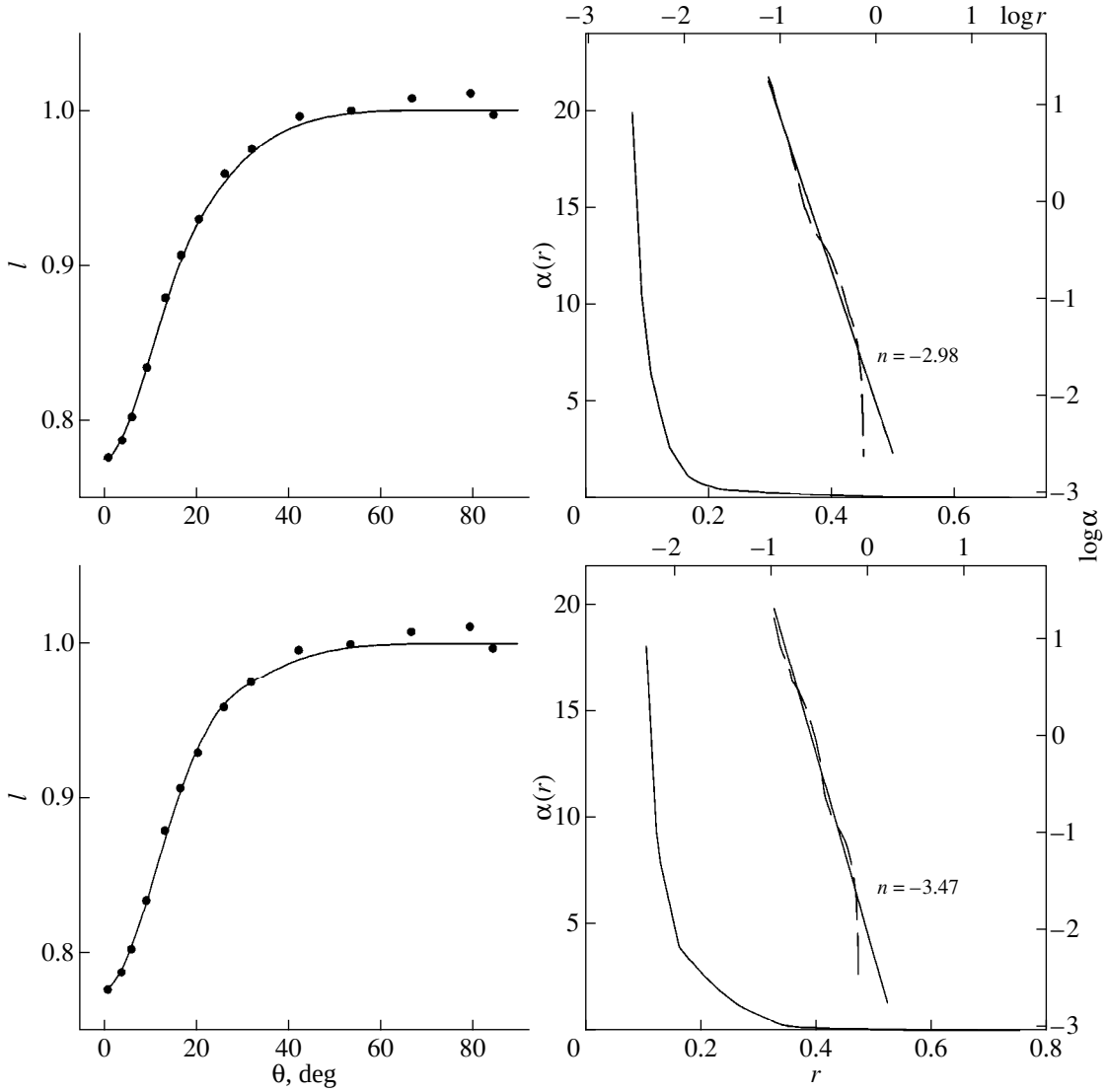

Fig. 5. Solution of Abelian equation (2) on the class of concave functions for the two solutions of problem (1). Above: solution corresponding to the absolute minimum of the residual. Below: solution corresponding to fixed relative luminosity of the WN5 component, $L_{WN5} = 0.38$. Also shown are the same solutions on a logarithmic scale and linear approximations. The parameter n is the index of the power law used to fit $\alpha(r)$. The corresponding theoretical light curves at the primary minimum are shown to the left of the solutions.

The hydrostatic core radius of the WR star cannot be determined in our model from the observations used here: optical continuum observations cannot penetrate into the WR wind beyond layers where the continuum optical depth $\tau(\xi)$ is of order unity, and the radii of these layers appreciably exceed the hydrostatic core radius. Therefore, when approximating the reconstructed velocity distribution using the Lamers law, we set $r_c = 0.05 \approx 2R_\odot$, which is a reasonable estimate [17]. Note that, since we actually fit the ratio of $v(r)$ to $v_0 = v_\infty(1 - r_c/r_0)^\beta$, v_∞ is not an approximation parameter.

It follows from Fig. 6 that, for both light-curve solutions, the parametric approximations of the velocity distribution yield $\beta = 1.58$–1.82 and $n = 0.94$–1.45.[3] This means that, on the whole, the acceleration of the WR wind is relatively slow compared to the acceleration expected for a Lamers law with $\beta \sim 1$ in the standard model [1]. In addition, our result indicates that the acceleration persists at comparatively large distance from the star, where the velocity is virtually constant for a Lamers law with $\beta = 1$. This result is in agreement with the conclusions of other studies that the acceleration in the stellar winds of WR stars is relatively slow

[3] The index n in the power-law approximation must be equal to the absolute value of the corresponding index n in Fig. 5 minus two. The small discrepancy in our case is due to the restriction on $\tau_{rad}(r)$ adopted during the approximation.

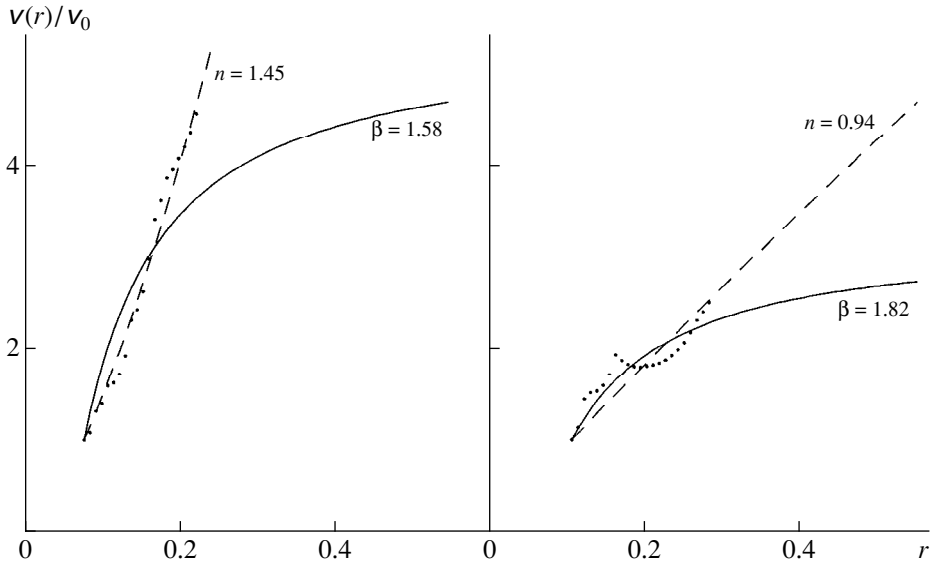

Fig. 6. Velocity distribution in the photosphere of the WN5 component for the two solutions of Abelian equation (2). The dots show $v(r)/v_0$ values at grid points. Left: solution corresponding to the absolute minimum of the residual $\eta_1 + \eta_2$. Right: solution corresponding to fixed relative luminosity of the WN5 component, $L_{WN5} = 0.38$. Also shown are Lamers-law (solid curves) and power-law (dashed lines) approximations of these solutions.

[20–22]. Note that both the Lamers law and the power-law approximations fail to satisfactorily describe the derived functions satisfactorily. If our reconstructions of the velocity distribution in the photosphere of the WN5 component in the V444 Cyg system are correct, this implies that the Lamers law is a poor approximation for the winds of WR stars. The significance of our conclusions can be checked by solving the inverse problems (2) and (1) using a parametric model for the WN5 wind. The results of this test will be published in a forthcoming paper [15].

6. CONCLUSIONS

We have solved the inverse problem of interpreting λ4244 Å optical continuum narrow-band observations of the eclipsing binary V444 Cyg. We imposed more specific *a priori* constraints on the unknown functions than those used in our previous studies [3, 5, 6]: namely, we assumed that the functions $I_c(\xi)$ and $I_a(\xi)$ describing the brightness distribution and absorption properties in the disk of the WN5 star are convexo-concave, monotonically non-increasing, and non-negative. The convex and concave parts of these functions correspond to the WR star core and its extended photosphere and atmosphere, respectively. The results of our analysis led us to the following conclusions.

(1) The shape of the surface of the total residual $\eta_1 + \eta_2$ is insensitive to the choice of *a priori* information. This result qualitatively confirms the choice of geometrical model parameters adopted in [3, 6]. It is nevertheless extremely important to use whatever independent information is available, such as the relative luminosity of the WN5 component, for example, if we wish to improve the reliability of the results obtained.

(2) Whatever *a priori* information is used, the core radius of the WN5 star, r_{WN5}^{core}, derived from the minimum of the total residual does not exceed $4R_\odot$. The brightness temperature of the core is very high ($T_{br}^{core} \geq 52000$ K [23]), in accordance with previous results obtained without invoking the spectrophotometrically estimated relative luminosity of the WN5 component.

(3) There is no doubt that the WN5 stellar wind exhibits acceleration, and there is every reason to believe that the radial dependence of this acceleration differs from that implied by the usual Lamers law with index $\beta = 1$. In the vicinity of the core of the WN5 star, the acceleration is slower than predicted by the Lamers law, while significant acceleration is observed at large distances, where the Lamers law predicts virtually constant outflow velocity. This is supported by other observational evidence, and must be taken into account when developing new, more refined stellar-wind models for WR stars.

ACKNOWLEDGMENTS

This work was supported by the Russian Foundation for Basic Research (project code 99-02-17589) and the Program for the Support of Leading Scientific Schools (grant no. 00-15-96553).

REFERENCES

1. W.-R. Hamann, L. Koesterke, and G. Grefener, in *Wolf–Rayet Phenomena in Massive Stars and Starburst Galaxies (IAU Symposium 193)*, Ed. by K. A. van der Hucht, G. Koenigsberger, and Ph. R. J. Eenens (Astronomical Society of the Pacific, 1999), p. 138.
2. D. J. Hillier and D. L. Miller, Astrophys. J. **519**, 354 (1999).
3. A. M. Cherepashchuk, Sov. Astron. **9**, 725 (1975).
4. A. M. Cherepashchuk, J. A. Eaton, and Kh. F. Khaliullin, Astrophys. J. **281**, 774 (1984).
5. I. I. Antokhin, A. M. Cherepashchuk, and A. G. Yagola, Astrophys. Space Sci. **254**, 111 (1997).
6. A. V. Goncharskiĭ, A. M. Cherepashchuk, and A. G. Yagola, *Ill-posed Problems in Astrophysics* [in Russian] (Nauka, Moscow, 1985).
7. Kh. F. Khaliullin, Astron. Zh. **57**, 195 (1974).
8. A. M. Cherepashchuk, in *Wolf–Rayet Stars: Binaries, Colliding Winds, Evolution (IAU Symposium 163)*, Ed. by K. A. van der Hucht and P. M. Williams (Kluwer, Dordrecht, 1995), p. 262.
9. N. St-Louis, A. F. J. Moffat, L. Lapointe, *et al.*, Astrophys. J. **410**, 342 (1993).
10. A. M. Cherepashchuk, Astron. Zh. **67**, 955 (1990), [Sov. Astron. **34**, 481 (1990)].
11. T. J. Harries, D. J. Hillier, and I. D. Howarth, Mon. Not. R. Astron. Soc. **296**, 1072 (1998).
12. A. M. Cherepashchuk, G. Koenigsberger, S. V. Marchenko, and A. F. J. Moffat, Astron. Astrophys. **293**, 142 (1995).
13. L. Hartmann, Astrophys. J. **221**, 193 (1978).
14. W.-R. Hamann and E. Schwarz, Astron. Astrophys. **261**, 523 (1992).
15. I. I. Antokhin and A. M. Cherepashchuk, Astron. Zh. **78** (4), 313 (2001) [Astron. Rep. **45**, 269 (2001)].
16. A. N. Tikhonov, Dokl. Akad. Nauk SSSR **39**, 195 (1943).
17. N. Langer, Astron. Astrophys. **252**, 669 (1991).
18. I. I. Antokhin, S. V. Marchenko, and A. F. J. Moffat, in *Wolf–Rayet Stars: Binaries, Colliding Winds, Evolution (IAU Symposium 163)*, Ed. by K. A. van der Hucht and P. M. Williams (Kluwer, Dordrecht, 1995), p. 520.
19. A. M. Cherepashchuk, in *Wolf–Rayet Stars in the Framework of Stellar Evolution (33rd Liège International Astrophysics Colloquium)*, Ed by J.-M. Vreux *et al.* (Liège, 1996), p. 155.
20. G. Koeningsberger, Astron. Astrophys. **235**, 282 (1990).
21. A. F. J. Moffat, in *Wolf–Rayet Stars in the Framework of Stellar Evolution (33rd Liège International Astrophysics Colloquium)*, Ed. by J.-M. Vreux *et al.*, (Liège, 1996), p. 199.
22. S. Lepine and A. F. J. Moffat, Astrophys. J. **514**, 909 (1999).
23. A. M. Cherepashchuk, in *Thermal and Ionization Aspects of Flows from Hot Stars: Observations and Theory*, Ed. by H. J. G. L. M. Lamers and A. Sapar, Astron. Soc. Pac. Conf. Ser. (2000) (in press).

Translated by A. Dambis

Astronomy Reports, Vol. 45, No. 5, 2001, pp. 382–388. Translated from Astronomicheskiĭ Zhurnal, Vol. 78, No. 5, 2001, pp. 444–451.

A Study of Rare Earth Elements in the Atmospheres of Chemically Peculiar Stars. Pr III and Nd III Lines

T. A. Ryabchikova[1, 2], I. S. Savanov[3, 4], V. P. Malanushenko[3, 4], and D. O. Kudryavtsev[5]

[1]*Institute of Astronomy, Pyatnitskaya ul. 48, Moscow, 109017 Russia*
[2]*Institute for Astronomy, University of Vienna, Türkenschanzstrasse 17, Vienna, A-1180 Austria*
[3]*Crimean Astrophysical Observatory, p/o Nauchnyĭ, Crimea, 334413 Ukraine*
[4]*Isaac Newton Institute, Chile, Crimean Branch*
[5]*Special Astrophysical Observatory, Nizhniĭ Arkhyz, 357147 Russia*

Received July 17, 2000

Abstract—We determine the abundances of Pr and Nd in the atmospheres of magnetic and non-magnetic chemically peculiar stars from the lines of rare earth elements in the first and second ionization states. The computations for the magnetic stars take into account the influence of the magnetic field on line formation. We studied the influence of errors in the stellar-atmosphere parameters and the atomic parameters of the spectral lines on the accuracy of abundance determinations. Within the derived accuracy, ionization equilibrium is satisfied in the atmospheres of non-pulsating magnetic and non-magnetic stars (so that abundances derived separately from lines of first and second ions agree). For all the pulsating magnetic (roAp) stars studied, the abundances derived from lines of second ions are 1.0 to 1.7 dex higher than those derived from first ions. The violation of ionization equilibrium in the atmospheres of pulsating stars is probably due to, first, considerable enrichment of Pr and Nd in the uppermost atmospheric layers, and second, a higher location for the layer of enhanced elemental abundance in roAp stars than in non-pulsating stars. Two objects from the list of non-pulsating magnetic stars, HD 62140 and HD 115708, exhibit anomalies of their Pr and Nd lines characteristic of roAp stars. The differences in the rare earth anomalies for the pulsating and non-pulsating peculiar stars can be used as a selection criterion for candidate roAp stars. © *2001 MAIK "Nauka/Interperiodica".*

1. INTRODUCTION

The presence of abnormally strong lines of rare earth elements (lanthanides) is characteristic of the spectra of chemically peculiar (Ap) stars. Analyses of lanthanide abundances in Ap stars have so far been limited to lines of elements in the first ionization state, though rare earths in the second ionization state dominate in Ap atmospheres over a wide range of effective temperatures. Lines of second ions of some elements have been identified in the spectra of several Ap stars, for example, Ce III [1–3], Pr III [1, 2, 4], Nd III [2, 5], Eu III [6], Er III [1], Tb III [7], and Dy III [8]. However, quantitative studies became possible only recently, when oscillator strengths for the corresponding lines were computed.

It was first noted in [5] that, in the spectrum of the pulsating Ap (roAp) star γEqu, the abundance of neodymium derived from Nd III lines was 1.5 dex higher than that derived from Nd II lines. It was also noted (V.P. Malanushenko, private communication) that the λ6706.7 line in the spectra of roAp stars, which is abnormally strong compared to the spectra of non-pulsating Ap stars, could be identified with the Pr III λ6706.71 line. A study of the rapid radial-velocity variability for one of the brightest roAp stars, γEqu, showed that precisely the Pr III and Nd III lines had the maximum amplitudes for radial-velocity variations with the period of the brightness variations [9].

We decided to study in detail the Pr and Nd abundances in the spectra of cool, magnetic, peculiar, pulsating and non-pulsating, stars based on first- and second-ionization lines. To check the accuracy of the computed oscillator strengths for the second-ionization lines, we also studied the spectra of peculiar stars on the non-magnetic sequence, namely Am and HgMn stars.

2. OBSERVATIONS AND REDUCTION OF SPECTRA

A list of our program stars is presented in Table 1. It includes the three non-magnetic peculiar stars HR 7775 (HgMn), 15 Vul, and 32 Aqr (Am stars), six magnetic non-pulsating stars, and six roAp stars. The magnetic, non-pulsating stars were selected from the list [10] of stars without pulsations found by several groups of astronomers in systematic studies. When selecting the non-pulsating and pulsating stars, we tried to have the effective temperatures of the two groups overlap. The main parameters of the program stars are given in the corresponding columns of Table 1. The last column of the Table contains references for the parameters, especially for the model-atmosphere and magnetic-field data.

For HR 4816, HR 7575, α Cir, and BI Mic, we used the same spectra as in [6]. The line equivalent widths in

1063-7729/01/4505-0382$21.00

Table 1. Main atmospheric parameters for the program stars (effective temperatures, gravities, surface magnetic fields, rotational velocities, and metallicities)

Star	HD	$T_{\rm eff}$, K	log g	B_s, kG	$v \cdot \sin i$, km/s	Metal abundance, dex	References
HgMn stars							
HR 7775	189849	10650	4.1	0.0		0.0	[11]
Am stars							
15 Vul	209625	7700	3.5	0.0	10	0.0	[12]
32 Aqr	193452	7700	3.65	0.0	5	0.0	[12]
Non-pulsating CP2 stars							
HR 4816	110066	9000	4.3	3.6	9	+1.0	[6]
HR 7575	188041	8500	4.5	3.6	2	+0.5	[6]
49 Cam	62140	7900	4.3	4.5	23	+0.5	[13]
β CrB	137909	7750	4.3	5.7	3.5	+0.5	[6]
	184471	7500	4.0	–	10	0.0	[14]
	115708	7510	4.0	3.5	13	0.0	[13, 15]
roAp stars							
	42659	8100	4.2	–	23	+0.2	[16]
α Cir	128898	7900	4.3	2.0	12.5	0	[6]
γEqu	201601	7700	4.2	4.0	0	+0.5	[6]
10 Aql	176232	7550	4.2	1.5	5.0	0.0	[17]
BI Mic	203932	7450	4.3	0.0	12.5	0.0	[6]
DO Eri	24712	7250	4.3	3.0	5.6	0.0	[6]

the spectrum of the HgMn star HR 7775 were taken from [11]. The spectra for the rest of the stars in the region of the strongest and least blended Pr III and Nd III lines were obtained using the 2.6-m telescope of the Crimean Astrophysical Observatory (CrAO) and the 1-m and 6-m telescopes of the Special Astrophysical Observatory (SAO), equipped with CCD cameras. Each CrAO spectrum covers about 70 Å; the spectral resolution was 30000, with signal-to-noise ratios of 200 to 300. Spectra of the fainter stars, HD 188441 and 10 Aql, were taken with the Main Stellar Spectrograph of the SAO 6-m telescope. These spectra cover the ranges 5000–5150 Å, 5103–5264 Å (resolution 18000), and 6270–6515 Å, 6561–6805 Å (resolution 12000). The total signal-to-noise ratio was about 200. Spectra of HD 62140 and HD 42659 were taken with the Coudé échelle spectrometer of the SAO 1-m telescope [18], with a spectral resolution of 36000 and signal-to-noise ratios of about 100–150. Table 2 presents a log of our observations; the third column contains the central wavelengths of the observed spectral ranges. The rare earth line intensities for DO Eri vary considerably with the rotational period [19]; observations of this star were obtained at phases close to those for the maximum rare earth line intensities.

The standard spectral reduction (subtraction of the sky background, flat-fielding, removal of cosmic-rays, wavelength calibration, determination of the continuum level) was performed in the SPE software package for spectral reduction (S. Sergeev, CrAO), the DECH20 package ([20], for the 1-m SAO telescope), and the "long" context of MIDAS (for the 6-m SAO telescope).

3. MODEL-ATMOSPHERE PARAMETERS AND SPECTRAL ANALYSIS TECHNIQUES

Parameters of the model atmospheres for most stars were determined in the cited papers from their photometric indices in the Geneva and/or Strömgrem system. For HR 7775 [11], 15 Vul and 32 Aqr [12], HR 4816, HR 7575, β CrB, γEqu [6], and 10 Aql [17], the model-atmosphere parameters were improved by comparing their spectral energy distributions with theoretical fluxes. For example, we refined the effective gravity of 49 Cam by comparing theoretical energy distributions computed for an effective temperature of 7900 K from [13] and a series of surface gravities to the observed spectral energy distribution from [21].

Our analyses of the elemental abundances in the atmospheres of the program stars were carried out using synthetic-spectrum computations. We used data from the Vienna database of atomic parameters for spectral lines, VALD [22], to identify the spectral lines and compute the synthetic spectra.

Table 2. Observation log

Star	HJD 2400000+	Spectral range, Å	Telescope	Star	HJD 2400000+	Spectral range, Å	Telescope
15 Vul	50414.251	6150	2.6 m	HD 62140	50829.606		1 m
	50797.182	6340	2.6 m	HD 115708	51336.288	6150	2.6 m
32 Aqr	50694.306	6150	2.6 m		51336.334	6340	2.6 m
HR 4816	50501.577	4921	2.6 m	HD 42659	50830.395		1 m
	50501.558	6150	2.6 m		50833.286		1 m
	50501.543	6340	2.6 m	γEqu	51046.268	4921	2.6 m
	50501.531	6645	2.6 m		51066.283	6150	2.6 m
HR 7575	50294.361	4921	2.6 m		51047.256	6340	2.6 m
	50294.338	6150	2.6 m		51054.370	6340	2.6 m
	50294.345	6340	2.6 m		51055.333	6340	2.6 m
	50294.353	6645	2.6 m		51027.364	6690	2.6 m
β CrB	50907.537	6160	2.6 m		51028.379	6690	2.6 m
	50907.542	6360	2.6 m	10 Aql	51084.223	6150	2.6 m
	50917.477	6645	2.6 m		51029.525	5100	6 m
	50917.486	6645	2.6 m		51029.338	5100	6 m
HD 184471	51030.346	5200	6 m		51029.363	5200	6 m
	51030.382	5200	6 m		51029.308	6400	6 m
	51030.418	5100	6 m		51029.280	6700	6 m
	51030.451	5100	6 m	DO Eri	51240.227	6090	2.6 m
	51030.493	6400	6 m		51240.165	6150	2.6 m
	51030.259	6700	6 m		51240.216	6340	2.6 m

3.1. Parameters of Spectral Lines

Since we are dealing with peculiar stars whose spectra are extremely blended due to the enhanced density of lines, the accuracy of abundance determinations depends primarily on the accuracy of the spectral-line parameters and the completeness of the allowance for all the lines forming the blends. In our range of effective temperatures, the main contribution to the line spectrum comes from iron-peak elements, both neutral and in the first ionization state, and rare earths in the first ionization state. Accuracy estimates for these elements' oscillator strengths presented in the VALD can be found in [22, 23]. Here, we describe in more detail the atomic data for Pr III and Nd III, the elements of principal interest for us.

We used the lists of laboratory wavelengths from [24] (Pr III) and [5] (Nd III) from 4700 to 7200 Å to identify these elements. Depending on the completeness of the spectra and the amount of blending, we analyzed from one to 11 lines of each ion in the stellar spectra. Table 3 gives the atomic parameters for several Pr III and Nd III lines present in most of the stars, along with the total numbers of lines used for the analysis of the atmospheric abundances of individual stars.

The oscillator strengths for the Nd III lines were taken from [5, 25]. The latter paper also presents computations of Landé factors, needed when considering atmospheres with magnetic fields. For transitions not including *p* electrons, the uncertainty of the oscillator strengths is ±0.15 dex. Since the core polarization skeleton was not taken into account, the computed oscillator strengths may be systematically high by 0.2 dex. The computational uncertainty of the Landé factors is about 5%.

Neodymium is an even-number element, and hyperfine splitting should be negligible. On the contrary, praseodymium is an odd-number element, and in fact, line broadening due to hyperfine structure was noted in [24]. However, experimental studies of the hyperfine structure of Pr III lines (G. Wahlgren, private communication) have shown that this effect is not strong for the lines considered in the present study. Since the data on the hyperfine structure of the Pr III lines are not yet published, we did not take this effect into account.

The oscillator strengths and Landé factors for the Pr III lines were computed by D. Bord (private communication) using the same scheme as for Nd III [25]. At our request, A.N. Ryabtsev (private communication) undertook independent computations including many atomic levels. The oscillator strengths computed by Ryabtsev are, on average, lower than Bord's values by 0.22 dex. Dolk *et al.* [26] studied Pr II and Pr III lines in high-

Table 3. Pr and Nd abundances from individual Pr III and Nd III lines (the total number of lines used to determine the final abundance listed in Table 4 is given)

λ, Å	E_i, eV	log[gf]	HR 4816	HR 7575	β CrB	HD 184471	HD 62140	HD 115708	HD 42959	α Cir	γEqu	10 Aql	BI Mic	DO Eri
Pr III														
6071.09	0.36	−2.09											−8.89	−8.35
6090.02	0.36	−0.69					−7.96		−7.86				−8.73	−7.77
6160.24	0.17	−0.83	−8.76	−8.96	−9.41		−8.36	−8.63	−8.06	−8.96	−8.41	−9.66	−9.07	−7.96
6161.22	1.55	−0.73		−8.86	−9.21			−8.93	−7.76		−8.48	−9.46		−8.06
6706.71	0.55	−1.28							−8.06		−8.51	−9.56	−9.03	
Total No. of lines			1	2	2	–	6	2	8	4	3	3	11	4
Nd III														
5102.42	0.63	−0.40				−9.56					−7.66	−7.46	−7.23	
5193.06	0.14	−0.77				−9.96					−7.66	−8.46	−7.44	
5286.76	0.63	−1.60			−8.26								−7.95	
6145.07	0.30	−1.33	−8.06	−7.76	−8.34		−6.48	−7.53	−7.63	−7.56	−7.13	−8.04	−7.93	−6.98
6327.24	0.14	−1.40	−8.06	−7.96	−8.36	−9.56	−6.66	−7.76	−7.56	−7.55	−7.16	−7.96	−7.56	−7.22
Total No. of lines			2	2	3	−3	3	2	3	4	5	4	10	2

resolution spectra of several HgMn stars and obtained a system of astrophysical oscillator strengths that is in very good agreement with Bord's computations. For this reason, we used these computations as the main source of oscillator strengths for the Pr III lines. The intrinsic scatter is ±0.15 dex, but the possible presence of the above-mentioned bias of the absolute oscillator strength scale should be kept in mind. The oscillator strengths for several Pr III lines are presented in Table 3.

3.2. Techniques for Computation of the Synthetic Spectrum

Since most of the program stars have strong magnetic fields, we computed the synthetic spectra taking into account the magnetic field in the transport equation. As in [6], we used the SYNTHMAG code written by Piskunov [27], which uses a simplified representation of the magnetic field as a vector with a constant magnitude and orientation with respect to the stellar surface. The visible surface of the star was divided into seven annular zones according to their angular distance from the center; in principle, we can adopt a different strength and direction of the field in each zone. However, for our goal—to find the influence of the magnetic field on determination of an element's abundance—it is sufficient to adopt a magnetic field with the same direction over the whole surface and with a constant magnitude, equal to the observed value tabulated in Table 1. For stars with resolved Zeeman components of Fe I, Fe II, Cr I, and Cr II lines in their spectra, we chose the magnetic-field direction by comparing their computed and observed profiles. For all the other stars, we computed synthetic spectra using a radial field. All our computations for the magnetic stars assumed zero microturbulence velocity; the microturbulence velocities for the Am and HgMn stars were taken from the papers cited in Table 1. For these non-magnetic stars, part of the elemental abundances were computed from the equivalent widths using the WIDTH9 code by Kurucz [28], modified by V. Tsimbal (cf. [19]).

The stars' rotational velocities, needed to compare the synthetic and observed spectra, were taken from the papers indicated in the last column of Table 1, with the exception of HD 184471 and HD 42659, whose rotational velocities we estimated as part of the study.

4. PRASEODYMIUM AND NEODYMIUM ATMOSPHERIC ABUNDANCES

This is the first large-scale quantitative study of praseodymium and neodymium based on Pr III and Nd III lines. In order to give an idea of the real uncertainties in the abundances of these elements in the spectra of the peculiar stars, Table 3 presents the results of our analysis for the magnetic stars for several individual lines present in most of the spectra. This table also gives, for each star, the total number of lines used to derive the final abundances presented in Table 4. The Pr and Nd abundances estimated from lines of first and second ions are given separately. We also tabulated Eu abundances, partly taken from [6, 12] and partly determined by us (for HD 184471, HD 62140, HD 115708, and HD 42659), as well as the abundances of Si, Cr, and Fe, whose lines could be blended with the Pr III and Nd III lines of interest to us. This is especially true of silicon, and we will discuss this element later. Except for Si and Eu, each abundance is accompanied by the rms deviation in units of 0.1 dex of the abundance in brackets.

Table 4. Si, Cr, Fe, Pr, Nd, and Eu atmospheric abundances for the program stars

Star	log(Si/H)	log(Cr/H)	log(Fe/H)	log(Pr/H)		log(Nd/H)		log(Eu/H)
				Pr II	Pr III	Nd II	Nd III	
HgMn stars								
HR 7775		−5.75(13)	−4.15(22)	−7.96(12)	−8.23:	−7.85(19)	−8.07(26)	–
Am stars								
15 Vul	−5.26	−6.33(29)	−4.80(23)	−10.06(25)	−10.60:	−10.07(26)	−9.92(22)	−9.74
32 Aqr	−4.91	−6.03(22)	−4.45(22)	−9.98(16)	−10.36:	−9.52(16)	−9.72:	−10.64
Non-pulsating CP2 stars								
HR 4816	−3.80	−3.61(10)	−3.46(10)	−8.70:	−8.76(30)	−7.90(30)	−8.06(20)	−8.36
HR 7575	−4.43	−4.21(10)	−3.98(10)	−9.00:	−8.91(30)	−8.15(30)	−7.86(20)	−7.66
β CrB	−4.80	−4.56(10)	−4.15(10)	−9.31(30)	−9.31(20)	−8.61(20)	−8.32(05)	−8.46
HD 184471	–	−4.66(20)	−4.26(20)	−10.10(40)	≤−9.50	−9.72(30)	−9.69(25)	−9.76
HD 62140	−5.16	−4.56(20)	−4.16(15)	−8.76(25)	−7.96(30)	−7.83(20)	−6.54(15)	−8.81
HD 115708	−4.96	−5.71 (10)	−4.91(10)	−10.16	−8.78(25)	−7.36(20)	−7.64(16)	−9.56
roAp stars								
HD 42659	−5.30	−5.15(30)	−4.56(30)	−9.10(30)	−7.76(24)	−8.65(30)	−7.58(10)	−9.56
α Cir	−4.60	−5.31(25)	−4.46(10)	−10.36(10)	−8.72(23)	−9.26(25)	−7.60(06)	−9.66
γEqu	−4.65	−5.31(30)	−4.31(25)	−9.80(24)	−8.47(05)	−8.91(22)	−7.46(28)	−9.86
10 Aql	−4.60	−5.06(20)	−4.34(11)	−10.46(30)	−9.56(10)	−9.61(35)	−7.98(41)	−10.06
BI Mic	−4.80	−5.50(20)	−1.46(15)	−10.05(37)	−8.76(23)	−9.46(27)	−7.54(26)	−9.96
DO Eri	−5.05	−5.81(20)	−5.06(15)	−9.70(30)	−8.04(24)	−8.56(27)	−7.10(20)	−9.36

A colon indicates that an element's abundance was derived from a single line.

Let us discuss the procedure used to determine the elemental abundances from the spectra of several stars in more detail. In the list of measured equivalent widths for the Hg Mn star HR 7775, courteously sent by S. Adelman, we could identify the Pr III λ4625.19 line and two Nd III lines, λλ4483.43, 4624.99. In [11], the λ4483.43 line was identified as an ionized sulphur line, but our computations show the contribution of sulphur to this blend to be negligible. We used the same lines as in [11] to compute the praseodymium and neodymium abundances from Pr II and Nd II lines. The slight difference between our abundances and those in [11], in particular for praseodymium, is due to the use of different oscillator strengths.

A single Pr III line, λ6160.24, was used to estimate the praseodymium abundances in the atmospheres of the metal-line stars 15 Vul and 32 Aqr. For neodymium, we used the Nd III λ6145.07 (15 Vul, 32 Aqr) and Nd III λ6327.24 (15 Vul) lines. The equivalent widths of the Pr II and Nd II lines for the abundance determinations were taken from [12, 29] for 15 Vul and from [12] for 32 Aqr. The Cr and Fe abundances from [12] coincide with our estimates based on small parts of the spectra used in our study.

The Cr, Fe, and Eu abundances in the atmospheres of the magnetic stars were compared to those from earlier studies in [6]. Here, we note the following. During the preparation of that paper, a detailed abundance study based on higher-resolution spectra in the 4700–7100 Å range was carried out for the roAp star 10 Aql [17]. The results of the two papers coincide within the errors for the two studies.

We present the Si abundances for stars with synthetic spectra in the range 6110–6177 Å, which includes the Pr III λ6160.24 and Nd III λ6145.07 lines. The first line is one of the best lines for abundance determinations, since it is almost unblended for stars with moderate rotation. The second line is one of the strongest lines of the second neodymium ion, but is blended with the Si I λ6145.02 line (multiplet 29), and the degree of blending increases as the star's effective temperature decreases. Several more lines of neutral silicon, of multiplets 29 and 30, are present in the same spectral range. Therefore, we first derived the silicon abundance, presented in Table 4, from these lines and then took into account the contribution of the Si I λ6145.02 line using this abundance. The computations of the corresponding Si lines in the solar spectrum show that the oscillator strengths in the VALD database have very good relative accuracy, ≈0.05 dex, but result in a silicon abundance that is 0.45 dex lower than the standard solar value. To compare our results for the silicon abundances with those of other studies that did not work with lines of

these multiplets, a correction of +0.45 dex should be applied to the Si abundances from Table 4.

In the previous section, we discussed possible uncertainties in the oscillator strengths used. Here, we consider uncertainties due to inaccuracies in the atmospheric parameters. The computations show that Pr III and Nd III lines with low excitation potentials reach their maximum intensities near an effective temperature of 7500 K. Though this is only 150 K lower than the mean temperature of our program stars, we computed the possible uncertainties in the abundances of Pr and Nd derived from lines of the first and second ions, relative to a model with $T_{\rm eff}$ = 7500 K and $\log g$ = 4.0. When the effective temperature is changed by ±500 K, much more than the usual 100 to 200 K uncertainty in the temperatures of cool peculiar stars, the praseodymium/neodymium abundances change by +0.38/–0.22 dex (first ions) and +0.08/+0.08 dex (second ions). The abundance changes corresponding to changes in $\log g$ by ±0.5 are +0.20/–0.10 (first ions) and +0.32/–0.27 (second ions). The computations also show that the uncertainties due to errors in the partition functions do not exceed 0.1 dex over the entire range of effective temperature.

The results of our studies of the Pr and Nd abundances in the atmospheres of peculiar stars for the various groups are the following.

(1) Within the abundance uncertainties indicated, the lines of first and second ions of the rare earth elements Pr and Nd give the same abundances for these elements in the atmospheres of non-magnetic peculiar stars. The slight (0.2 dex) deviation from ionization equilibrium is in agreement with estimates of the possible bias of our adopted absolute scale for the oscillator strengths of the Pr III and Nd III lines.

(2) Ionization equilibrium of praseodymium and neodymium is observed in the atmospheres of four of the six non-pulsating magnetic stars.

(3) In the atmospheres of all roAp stars, without exception, the Pr and Nd abundances derived from the lines of second ions are 1–1.7 dex higher than those derived from the lines of first ions. No uncertainties in the standard abundance analysis can explain this result.

(4) Two stars, HD 62140 and HD 115708, identified in the group of non-pulsating stars in Table 4, show abundance anomalies characteristic of roAp stars. This is especially clear for HD 115708, which resembles the roAp star BI Mic in all its observed features.

Let us discuss these two stars in more detail. Matthews and Wehlau [30] revealed variations in HD 62140 with a 62-min period from their time-resolved photometry during two of three nights. These variations were not confirmed by other observers, but neither can they be discounted. HD 115708 was studied to search for rapid variability by a single observing team [31], who found no pulsations. The same team obtained a similar negative result for HD 42659, but pulsations in this star were detected in subsequent observations [32]. Thus, there remains the possibility that pulsations will be detected in HD 115708 in future studies.

Though the number of stars studied by us is not large, we suggest that the non-pulsating and pulsating stars have different abundances; namely, the rare earths show a strong deviation from ionization equilibrium in the atmospheres of roAp stars and no such effect in the atmospheres of non-pulsating stars. The detection of pulsations in HD 115708 would be additional confirmation of this difference in rare earth anomalies between the pulsating and non-pulsating peculiar stars. Such analyses of rare earth abundances based on lines of the first and second ionization states could be used as a criterion when selecting roAp candidates.

5. DISCUSSION

Our principal results were already evident two years ago, at the beginning of our study. Since then, abundances were studied for three more roAp stars: HD 166473 [33], HD 101065 (Przybylski's star) [7], and HD 122970 [17]. Preliminary results presented at a workshop of the Working Group on Stellar Atmospheres in the CrAO (1999) and at the international conference "Magnetic Fields of Peculiar and Related Stars" (SAO, 1999) stimulated a more detailed study of rare earth abundances derived from the first and second ionization states. The same anomalies seen in our program roAp stars were found in the atmospheres of the three stars. Unfortunately, few non-pulsating stars have been studied in the relevant range of effective temperatures; however, the fact that β CrB and HD 184471 do not show rare earth anomalies characteristic of roAp stars leads us to conclude that there is some relation between such anomalies and pulsations. This is supported by the fact that in γEqu, whose pulsation amplitudes have been studied in detail using individual lines, the largest amplitudes are shown by the Pr III and Nd III lines [9].

Recall that our abundance determinations assumed uniform abundances throughout the stellar atmospheres. It is probable that the observed violation of ionization equilibrium for the rare earths in the atmospheres of roAp stars is due to the vertical stratification of elements in the atmospheres of magnetic stars. Preliminary computations of spectra with stratified atmospheres show that Pr and Nd in the second ionization state dominate in the deepest (temperature effect) and the uppermost (density effect) atmospheric layers. To simultaneously obtain ionization equilibrium and the appreciable observed line depths for the second ions of the rare earths, their concentration in the uppermost atmospheric layers ($\log(\tau_{5000}) < 6$) must be increased by 4 to 5 dex. Of course, non-LTE effects can already be significant for such layers, but these are unlikely to change the observed pattern of the anomalies considerably.

Since the main global parameters (temperature, magnetic field, rotational velocity) of the groups of pul-

sating and non-pulsating magnetic stars partially overlap, we cannot expect processes leading to stratification of elements to occur only in the pulsating stars. However, the distribution of elements could change in the course of stellar evolution. Based on recent HIPPARCOS data, it was concluded in [34] that the evolutionary statuses of pulsating and non-pulsating magnetic stars are different, and that pulsating stars, as a group, are less evolved objects. The preliminary computations taking into account the stratification of rare earths in the stellar atmospheres indicate that the intensities of lines of first and second rare earth ions depend considerably on the location of the boundary layer above which the abundances are enhanced by several dex.

We suggest that the thickness of the layer of anomalous rare earth abundances in the upper atmosphere could increase with the star's age, so that its lower edge could be deeper in the atmospheres of older, non-pulsating stars. In this case, the rare earth abundances determined from the lines of first and second ions would become comparable, approaching the abundance in this layer (ionization equilibrium defined in a uniform-atmosphere approximation would be satisfied). Qualitatively, this possibility is supported by the higher rare earth abundances derived for the non-pulsating stars. Theoretical computations of diffusion of rare earth elements in the atmospheres of peculiar magnetic stars are sorely needed to test this hypothesis.

ACKNOWLEDGMENTS

This study was supported by the Russian Foundation for Basic Research (project code 98-02-16734) and the Austrian Fonds zur Förderung der wissenschaftlichen Forschung (project S7303-AST). We are very grateful to D. Bord (USA), A. Ryabtsev (Russia), and G. Wahlgren (Sweden) for making their results available prior to publication.

REFERENCES

1. S. J. Adelman, Astrophys. J., Suppl. Ser. **28**, 51 (1974).
2. S. J. Adelman, W. P. Bidelman, and D. M. Pyper, Astrophys. J., Suppl. Ser. **40**, 371 (1979).
3. D. J. Bord, C. R. Cowley, and P. L. Norquist, Mon. Not. R. Astron. Soc. **284**, 869 (1997).
4. G. Mathys and C. R. Cowley, Astron. Astrophys. **253**, 199 (1992).
5. C. R. Cowley and D. J. Bord, in *The Scientific Impact of the Goddard High Resolution Spectrograph*, Ed. by J. C. Brandt, T. B. Ake, and C. C. Peterson, Astron. Soc. Pac. Conf. Ser. **143**, 346 (1998).
6. T. Ryabchikova, N. Piskunov, I. Savanov, *et al.*, Astron. Astrophys. **343**, 229 (1999).
7. C. R. Cowley, T. A. Ryabchikova, F. Kupka, *et al.*, Mon. Not. R. Astron. Soc. **317**, 299 (2000).
8. G. C. L. Aikman, C. R. Cowley, and H. M. Crosswhite, Astrophys. J. **232**, 812 (1979).
9. I. S. Savanov, V. P. Malanushenko, and T. A. Ryabchikova, Pis'ma Astron. Zh. **25**, 916 (1999).
10. P. Martínez and D. W. Kurtz, Mon. Not. R. Astron. Soc. **271**, 129 (1994).
11. S. J. Adelman, Mon. Not. R. Astron. Soc. **266**, 97 (1994).
12. S. J. Adelman, H. Caliskan, D. Kocer, and C. Bolcal, Mon. Not. R. Astron. Soc. **288**, 470 (1997).
13. G. A. Wade, Astron. Astrophys. **325**, 1063 (1997).
14. P. Renson, D. Kobi, and P. North, Astron. Astrophys., Suppl. Ser. **89**, 61 (1991).
15. G. A. Wade, E. Neagu, and J. D. Landstreet, Astron. Astrophys. **307**, 500 (1996).
16. G. Mathys, N. Kharchenko, and S. Hubrig, Astron. Astrophys. **311**, 901 (1996).
17. T. A. Ryabchikova, I. S. Savanov, A. P. Hatzes, *et al.*, Astron. Astrophys. **357**, 981 (2000).
18. F. A. Musaev, Pis'ma Astron. Zh. **19**, 776 (1993) [Astron. Lett. **19**, 315 (1993)].
19. T. A. Ryabchikova, J. D. Landstreet, M. J. Gelbmann, *et al.*, Astron. Astrophys. **327**, 1137 (1997).
20. G. A. Galazutdinov, Prep. Special Astrophysical Observatory (1992).
21. S. J. Adelman, Astron. Astrophys., Suppl. Ser. **49**, 663 (1982).
22. F. Kupka, N. Piskunov, T. A. Ryabchikova, *et al.*, Astron. Astrophys. **138**, 119 (1999).
23. T. Ryabchikova, N. Piskunov, H. C. Stempels, *et al.*, Phys. Scr. **83**, 162 (1999).
24. J. Sugar, J. Res. Natl. Bur. Stand., Sect. A **78**, 555 (1974).
25. D. J. Bord, Astron. Astrophys., Suppl. Ser. **144**, 517 (2000).
26. L. Dolk, G. M. Wahlgren, H. Lundberg, *et al.*, Astron. Astrophys. (2001) (in press).
27. N. E. Piskunov, in *Second International Workshop on Solar Polarization, Bangalore*, Ed. by K. Nagendra and J. Stenflo (Kluwer, Dordrecht, 1999), p. 515.
28. R. L. Kurucz, CDROM13 (SAO, Cambridge, 1993).
29. L. S. Lyubimkov and I. S. Savanov, Izv. Krym. Astrofiz. Obs. **69**, 50 (1984).
30. J. M. Matthews and W. H. Wehlau, Publ. Astron. Soc. Pac. **97**, 841 (1985).
31. M. J. Nelson and T. J. Kreidl, Astron. J. **105**, 1903 (1993).
32. P. Martínez and D. W. Kurtz, Mon. Not. R. Astron. Soc. **271**, 118 (1994).
33. M. Gelbmann, T. Ryabchikova, W. W. Weiss, *et al.*, Astron. Astrophys. **356**, 200 (2000).
34. S. Hubrig, N. Kharchenko, G. Mathys, and P. North, ESO Scientific Prep. No. 1361 (2000).

Translated by N. Samus'

Astronomy Reports, Vol. 45, No. 5, 2001, pp. 389–394. Translated from Astronomicheskiĭ Zhurnal, Vol. 78, No. 5, 2001, pp. 452–458.

Magnetic Fields and the $\dot{P}$–P Diagram for Radio Pulsars

I. F. Malov

Pushchino Radio Astronomy Observatory, Astro Space Center, Pushchino, Russia

Received May 24, 1999

Abstract—Various mechanisms for the loss of angular momentum of neutron stars are analyzed. Theoretical predictions about the evolution of the period are compared with the observed distribution of pulsars on the $\log\dot{P}\log(P)$ diagram. Pulsars with short periods ($P \le 0.1$ s) cannot be fit well by any of the models considered. Their braking index is $n = -1$, which requires the development of a new braking mechanism. The evolution of pulsars with $P > 1.25$ s is described by the law $\dot{P} \propto P^2$, probably due to processes internal to the neutron stars. The observational data for pulsars with $0.1 < P \le 1.25$ s can be fit with a hybrid model incorporating internal processes and magnetic-dipole losses. The magnetic fields in pulsar catalogs should be recomputed in accordance with the results obtained. For example, the magnetic fields obtained for two magnetars with $P = 5.16$ s and $P = 7.47$ s are $B_s = 1.7 \times 10^{13}$ and 2.9×10^{13} G, which are lower than the critical field $B_{cr} = 4.4 \times 10^{13}$ G.

For a substantial fraction of pulsars, their characteristic ages $\tau = P/2\dot{P}$ cannot serve as measures of their real ages. © *2001 MAIK "Nauka/Interperiodica".*

1. INTRODUCTION

Over the entire time that radio pulsars have been studied, the most important characteristic of these objects—their magnetic fields—has been estimated assuming that the only mechanism braking the neutron star is magnetic-dipole radiation at the rotational frequency Ω. It is assumed that the power of the magnetic-dipole radiation and the rate of rotational-energy loss are equal:

$$\frac{2B_0^2R_*^6\Omega^4\sin^2\beta}{3c^3} = I\Omega\dot{\Omega}. \quad (1)$$

Here, B_0 is the magnetic field at the surface of the neutron star, R_* is the star's radius, I its moment of inertia, and β the angle between the magnetic-moment vector and the rotational axis. All catalogs (see, for example, [1]) present the value $B_s = B_0\sin\beta$ derived from (1). However, other braking mechanisms are also known. Relativistic particles (the pulsar wind) can carry away a significant amount of angular momentum [2]. In [3], slowing of the pulsar's rotation is linked to ponderomotive forces that arise during the flow of currents on the neutron-star surface. A group of Chinese theoreticians [4, 5] have proposed that radiation in the inner layers of the neutron star leads to rapid braking of the rotation. The papers [6, 7] consider a pulsar model with a plasma disk around the neutron star, via which there is a loss of angular momentum from the star. Finally, the presence of currents and electric fields in the upper layers of the magnetosphere could lead to heating [8] and energy losses [9].

Including additional braking mechanisms leads to the appearance of new terms on the left-hand side of Eq. (1) describing the evolution of the pulsar's rotational period, $P = 2\pi/\Omega$. In this case, the tracks and distribution of pulsars in the $\dot{P}$–P diagram should be affected. The current paper analyzes these distributions and compares them with the predictions of various theoretical models.

2. MODELS

(1) We consider first the predictions of the traditional model for braking the neutron star via magnetic-dipole radiation. If B_0 and the angle β are constant in time, it follows from (1) that

$$P = \sqrt{P_0^2 + 2At}, \quad (2)$$

$$\dot{P} = \frac{A}{\sqrt{P_0^2 + 2At}}, \quad (3)$$

$$\tau = \frac{P}{2\dot{P}} = \frac{P_0^2}{2A} + t. \quad (4)$$

Here, P_0 is the pulsar's period at the time of its birth ($t = 0$), $A = 8\pi^2B_s^2R_*^6/3c^3I$, t is the pulsar's age, and τ is its characteristic age. The $\dot{P}$–P diagram should show the dependence

$$\dot{P} = A/P \quad (5)$$

with the scatter for individual objects being due to differences in their B_s, R_*, and I values.

(2) The evolution of the magnetic fields of pulsars remains an open question. There exist mechanisms that

could lead to decay of the field (ohmic losses in the neutron-star crust, for example). However, estimates of the characteristic time for such decay t_D vary from 10^6 yrs to values exceeding the Hubble time (>10^{10} yrs) [10]. At the same time, the generation of magnetic field over the pulsar's lifetime is possible (due to the motions of superconducting protons, for example [11]). If the magnetic field decays according to the relation

$$B_s = B_{s_0} e^{-t/t_D}, \tag{6}$$

we obtain from (1)

$$P = \sqrt{P_0^2 + At_D(1 - e^{-2t/t_D})}, \tag{7}$$

$$\dot{P} = \frac{Ae^{-2t/t_D}}{\sqrt{P_0^2 + At_D(1 - e^{-2t/t_D})}}, \tag{8}$$

$$\tau = \left(\frac{P_0^2}{2A} + \frac{t_D}{2}\right)e^{2t/t_D} - \frac{t_D}{2}. \tag{9}$$

These relations lead to a dependence $\dot{P}(P)$ of the form

$$\dot{P} = \frac{At_D + P_0^2 - P^2}{Pt_D}. \tag{10}$$

Below, we will assume that the magnetic field remains constant; i.e., we consider time intervals $t < t_D$.

(3) In the presence of circular motion of the neutrons inside the neutron star, neutrino–anti-neutrino pairs (ν, $\tilde{\nu}$) can be emitted due to the weak interaction of the neutral flow. At non-relativistic speeds, cyclotron neutrino radiation is emitted by the superfluid neutron vortices [4]. In this case, the rotational energy of normal neutrons is transferred to the superfluid vortices, which supports the latter but slows the rotation of the neutron star due to the interaction of the magnetic moments of the normal neutrons and electrons. Another process that brakes the neutron star is dipole radiation associated with the fact that a neutron moving in a circle has an anomalous magnetic moment [5]. Both these mechanisms are described by the relation [9]

$$\dot{P} = aP^2. \tag{11}$$

It follows from this equation that

$$P = \frac{P_0}{1 - aP_0t}, \tag{12}$$

$$\dot{P} = \frac{aP_0^2}{(1 - aP_0t)^2}, \tag{13}$$

$$\tau = \frac{1 - aP_0t}{2aP_0}, \tag{14}$$

where [5]

$$a = \frac{11}{12\pi}\frac{\gamma^4 m_n^2 R_p^3}{c^2\hbar^2}\frac{\overline{\Delta^2 B^2 n^{*3}}}{I n^*}. \tag{15}$$

Here, Δ is the energy gap associated with the Cooper pairs, n^* the circulation quantum number of a vortex, R_p the radius of the superfluid region $^3P_2$, B the internal magnetic field, γ the gyromagnetic ratio of a neutron, and m_n the neutron mass; an overline denotes averaging over all vortex lines.

(4) In the current-loss model of [3], the lost power is described by the expression [12]

$$W = b\frac{B_0^2\Omega^4 R_*^6}{c^3} i_0 \cos\beta, \tag{16}$$

where b is a numerical coefficient that takes on values from 0.33 to 0.48 as β varies from 0° to 90°, and i_0 is the dimensionless longitudinal current, which also depends on the angle β. This expression differs from the magnetic-dipole relation (1) by a numerical coefficient and in its different dependence on β. The dependence of the total power W on β remains unclear. In our analysis, this dependence is not of fundamental importance, since the main factors in the expression for W are B_0^2 and Ω^4. In particular, if we assume

$$B_s^2 = B_0^2 i_0 \cos\beta = B_{s_0}^2 e^{-2t/t_D}, \tag{17}$$

we arrive at the dependences (7)–(19), where the coefficient A is replaced by the coefficient $A_1 = \dfrac{4\pi b B_s^2 R_*^6}{c^3 I}$.

(5) In the disk model of [6], the energy-loss rate is equal to

$$I\Omega\dot{\Omega} = A_2\Omega^3, \tag{18}$$

where $A_2 = \pi B^2 R_*^6/3GM$. Here, G is the gravitational constant and M is the mass of the neutron star. In this model,

$$P = A_3 t + P_0, \tag{19}$$

$$\dot{P} = A_3, \tag{20}$$

$$\tau = \frac{A_3 t + P_0}{2A_3}, \tag{21}$$

$$A_3 = \frac{2\pi A_2}{I}. \tag{22}$$

(6) Energy losses in the outer layers of the magnetosphere lead to the dependence [9]

$$I\Omega\dot{\Omega} = \frac{kB^2 R_*^5 \Omega^2}{c^2}, \tag{23}$$

where k is a constant coefficient ($k < 1$). It follows from this equation that

$$P = P_0 e^{A_4 t}, \quad (24)$$

$$\dot{P} = P_0 A_4 e^{A_4 t}, \quad (25)$$

$$\tau = \frac{1}{2A_4}, \quad (26)$$

$$A_4 = k\frac{B^2 R_*^5}{Ic^2}. \quad (27)$$

3. MAGNETIC FIELDS CHARACTERIZING THE AGES AND BRAKING INDICES IN DIFFERENT MODELS

We will now analyze the magnitudes of the magnetic fields characterizing the ages and braking indices obtained for the various models.

(1) In the magnetic-dipole model, the magnetic field is calculated using the well known formula [13]

$$B_s = \left(\frac{3c^3 IP\dot{P}}{8\pi^2 R_*^6}\right)^{1/2}. \quad (28)$$

Adopting here and below $I = 10^{45}$ g cm^2 and $R_* = 10^6$ cm, we obtain

$$B_{s_{12}} \approx \sqrt{P\dot{P}_{-15}}, \quad (29)$$

where $B_{s_{12}} = B_s/10^{12}$ and $\dot{P}_{-15} = \dot{P}/10^{-15}$. The characteristic age during the interval $t \ll t_D$ is related to the real age of the pulsar by the linear dependence (5).

One parameter characterizing the evolution of the pulsar is the braking index n, which is given by the relation

$$\dot{\Omega} = \alpha\Omega^n \quad (30)$$

or by the observed values

$$n = \Omega\ddot{\Omega}/\dot{\Omega}^2. \quad (31)$$

For the magnetic-dipole model, $n = 3$, as follows from (1).

(2) Substituting $B = B_s$ in (15), we can present (11) in the form

$$\dot{P} = a_1 AP^2 = b_1 P^2 B_s^2, \quad (32)$$

where

$$a_1 = a/A, \quad (33)$$

$$b_1 = a/\overline{B^2}. \quad (34)$$

In this braking mechanism, the magnetic field is related to P and $\dot{P}$ by a functional dependence that differs from (29):

$$B_s^2 = \frac{\dot{P}}{b_1 P^2}, \quad (35)$$

and, in accordance with (14), the characteristic age decreases in time, and cannot serve as a measure of the real age. Moreover, at time $t = 1/aP_0\tau$ vanishes, and further becomes negative. In this case, as follows from (11), the braking index is $n = 0$.

(3) For the disk model (18), $n = 2$, τ grows linearly with time, and the magnetic field is independent of the period and is given by the expression

$$B_s = \left(\frac{3GMI}{2\pi^2 R_*^6}\right)^{1/2}\sqrt{\dot{P}}. \quad (36)$$

(4) In the case of heating of upper magnetospheric layers [9], $n = 1$. The characteristic age remains constant if the magnetic field is also constant in time. In the case of exponential decay of the field, τ increases as e^{2t/t_D}.

The magnetic field in this model is proportional to $\sqrt{1/\tau}$:

$$B_s = \left(\frac{Ic^2}{kR_*^5}\right)^{1/2}\sqrt{\frac{\dot{P}}{P}}. \quad (37)$$

Thus, our analysis shows that the braking index takes on values from zero to three in the models considered. The characteristic age has meaning only in the magnetic-dipole and disk braking models. The magnetic field depends differently on P and $\dot{P}$, and is described by the widely used relation (29) only in the magnetic-dipole model.

In early stages of the pulsar's evolution (when the period is very short), one of the main mechanisms for angular-momentum loss could be quadrupole gravitational radiation, for which $n = 5$ [14] and $\dot{P} \propto P^{-3}$.

4. THE OBSERVED $\dot{P}$–P DIAGRAM

Figure presents a $\log\dot{P}$ ($\log P$) diagram constructed for the data from [1]. The diagram is divided into three sections. The first contains 46 objects with $P \le 0.1$ s, for which the $\dot{P}(P)$ dependence differs from that for most pulsars [15]. We will discuss this section of the diagram below. The second region, $0.1 < P \le 1.25$ s, encompasses a large fraction of the pulsars ($N = 410$), for which magnetic-dipole braking appears to play an appreciable role. Finally, the right part of the diagram is occupied by pulsars with $P > 1.25$ s. In these objects, the braking

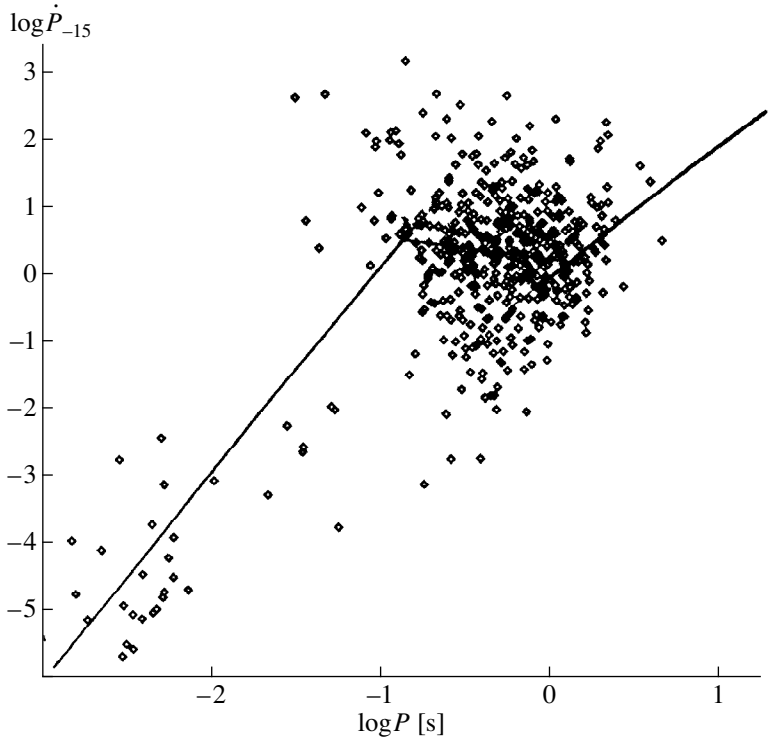

$\log \dot{P} \log(P)$ diagram for the data of the catalog [1]. The approximating linear fits are described by (38)–(40).

is probably associated primarily with internal radiation mechanisms [16]. Formal linear least-squares fits yield the following dependences for these three sections:

$$\begin{gathered}\log \dot{P}_{-15} = (3.10 \pm 0.54)\log P_{(c)} + (3.14 \pm 1.13),\\ \rho = 0.65 \pm 0.11,\\ N = 46,\\ P \le 0.1 \text{ s},\end{gathered} \tag{38}$$

$$\begin{gathered}\log \dot{P}_{-15} = (-0.34 \pm 0.18)\log P_{(c)} + (0.19 \pm 0.07),\\ \rho = -0.09 \pm 0.05,\\ N = 410,\\ 0.1 < P \le 1.25 \text{ s},\end{gathered} \tag{39}$$

$$\begin{gathered}\log \dot{P}_{-15} = (1.75 \pm 0.56)\log P_{(c)} - (0.01 \pm 0.15),\\ \rho = 0.32 \pm 0.10,\\ N = 87,\\ P > 1.25 \text{ s}.\end{gathered} \tag{40}$$

A formal description of the $\log \dot{P}(\log P)$ diagram using a single magnetic-dipole relation gives a sum of the squared deviations (residuals) of 1776, which exceeds the sum of the squared residuals for the three sections considered separately (481) by a factor of 3.7. Thus, it is not possible to describe the entire data set using a single magnetic-dipole model. The division of the data set into the three sections indicated yields the lowest sum of the squared residuals that we were able to obtain. Comparison of the resulting three relations with the predictions of the models considered in Section 2 shows that the braking in pulsars with the longest periods is determined primarily by processes internal to the neutron stars. For the bulk of the pulsar population ($0.1 < P \le 1.25$ s), we must consider the joint action of the magnetic-dipole model and the Chinese model [4, 5]. In such joint braking, it follows from (5) and (32) that

$$\dot{P} = \frac{A}{P}(1 + a_1 P^3). \tag{41}$$

The slope of this dependence for $a_1 P^3 \ll 1$ in the $\log \dot{P}(\log P)$ diagram has a tangent angle $\alpha_1 = -1$. In the region where $a_1 P^3 \gg 1$, $\alpha_2 = 2$. When $P_m = \left(\frac{1}{2a_1}\right)^{1/3}$ $\frac{d\dot{P}}{dP} = \frac{d\log \dot{P}}{d\log P} = 0$. The slope corresponding to a fit to the observational data depends on a_1. The numerical value of a_1 can be taken to be five [17], in which case $P_m = 0.46$ s and the $\log \dot{P}(\log P)$ dependence is non-monotonic. A formal linear fit yields a slope that is close to that for (39).

Integrating (41) leads to the following relation describing the evolution of the period [17, 18]:

$$t = -\frac{A}{3\times 5^{2/3}}\left\{\frac{1}{2}\ln\frac{(P+5^{-1/3})^2}{P^2-5^{-1/3}P+5^{-2/3}} - \sqrt{3}\left(\arctan\frac{2P-5^{-1/3}}{5^{-1/3}\sqrt{3}}+\frac{\pi}{6}\right)\right\}. \quad (42)$$

This expression is valid for small initial periods, and determines the pulsar's true age.

As noted above, when $P > 1.25$ s, the $\dot{P}(P)$ dependence (41) is close to that predicted by the internal braking model. In this case, when $a_1 = 5$, the pulsar's magnetic field is given by (35):

$$B_{12} = \sqrt{\frac{\dot{P}_{-15}}{5P^2}} \quad (43)$$

and differs from the tabulated values by a factor of $\sqrt{5P^3}$. For most pulsars, this difference is given by the factor $\sqrt{(1+5P^3)}$. It is especially important to use (43) when computing the magnetic fields of magnetars—sources of impulsive soft gamma-ray emission [19, 20]. In this case, tabulated values for B_s are erroneous, since they have been estimated assuming magnetic-dipole braking. Using (43) and the P and $\dot{P}$ values from [19, 20] yields $B_s = 1.7\times 10^{13}$ G for SGR 1806-20 ($P = 7.47$ s, $\dot{P} = 8.3\times 10^{-11}$) and $B_s = 2.9\times 10^{13}$ G for SGR 1900 + 14 ($P = 5.16$ s, $\dot{P} = 1.1\times 10^{-10}$). These magnetar magnetic fields are, indeed, very high, but do not exceed the critical field $B_{cr} = m^2c^3e\hbar = 4.4\times 10^{13}$ G.

It was shown in [21] that the process of pair formation

$$\gamma \longrightarrow e^+ + e^- \quad (44)$$

is suppressed when $B_s > B_{cr}$. Instead, there are decays of gamma-rays into two photons with lower energies:

$$\gamma \longrightarrow \gamma' + \gamma''. \quad (45)$$

If electron–positron pairs are not formed, the main mechanisms for the generation of radio emission do not operate, and magnetars should be radio-silent objects. However, an appreciable pulsing radio signal has been detected from SGR 1900 + 14 at 100 MHz [22]. Our corrected magnetar magnetic fields remove difficulties with the formation of pairs and the associated generation of radio emission.

Finally, we return to the left part of the $\dot{P}(P)$ diagram. The observed dependence (38) cannot be described by any of the models considered in Section 2. One possibility is that this is associated with the presence in this sample of a large number of pulsars in binary systems, and the influence of the orbital motion on the rapid braking of the neutron star. In this case, the disk model should have fit best, since the effect of orbital motion of material is taken into account to some extent. However, it follows from (20) that $\dot{P}$ is completely independent of the period in this model. If we consider only single pulsars with $P \le 0.1$ s, relation (39) is obeyed within the errors:

$$\log\dot{P}_{-15} = (2.75\pm 0.88)\log P_{(c)} + (2.80\pm 1.64), \quad \rho = 0.64\pm 0.20. \quad (46)$$

This means that some currently unidentified braking mechanism is acting in short-period pulsars. It follows approximately from (38) and (46) that $\dot{P}_{-15} = 10^3P^3$, or the braking index is negative ($n = -1$).[1] Such a $\dot{P}(P)$ relation indicates that the evolution of the pulsar parameters is described by the relations

$$P = \left(\frac{1}{P_0^2} - 2\times 10^3 t\right)^{-1/2}, \quad (47)$$

$$\dot{P} = 10^3\left(\frac{1}{P_0^2} - 2\times 10^3 t\right)^{-3/2}, \quad (48)$$

$$\tau = \frac{5\times 10^{-4}}{P_0^2} - t. \quad (49)$$

As in the Chinese model [4, 5], τ vanishes at time $t = 5\times 10^{-4}/P_0^2$, and further becomes negative; i.e., the "characteristic ages" of these pulsars do not reflect their real ages.

Due to the appreciable deviations in the $\dot{P}(P)$ dependence for this group of objects from the predictions of the magnetic-dipole model, the magnetic fields tabulated in catalogs are inaccurate, and should be recalculated after development of an adequate theory for the braking mechanism.

5. CONCLUSIONS

(1) We have analyzed the predictions of various models for braking of the rotation of a neutron star with regard to the evolution of the pulsar period P, the surface magnetic field B_s, and the characteristic age τ.

(2) The braking index n can take on values from zero to three in the various models considered.

(3) In most models, the characteristic age is not a measure of the real age. For example, in the hot-upper-magnetosphere model, τ does not depend on age, and in the Chinese model [4, 5], τ vanishes at some time t and further becomes negative.

[1] More precisely, $n = -0.75 \pm 0.88$, and negative values of n are most probable.

(4) The observed distribution of pulsars on the $\dot{P}(P)$ diagram can be divided into three regions ($P \le 0.1$ s, $0.1 < P \le 1.25$ s, and $P > 1.25$ s), for which the slopes of linear fits for $\log\dot{P}(\log P)$ differ.

(5) Short-period pulsars ($P \le 0.1$ s) cannot be described by any of the known rotation-braking mechanisms. Their braking index is $n \approx -1$, necessitating a search for braking processes that can explain this behavior. The magnetic fields calculated for these pulsars on the basis of magnetic-dipole models and tabulated in published catalogs are inaccurate, and must be recalculated after the development of an adequate theory for the braking mechanism. The observations show that, for this group of pulsars, as in the Chinese model [4, 5], τ vanishes at some time and then becomes negative, so that it cannot serve as even a crude estimate of the real age of the object.

(6) The behavior of pulsars with $P > 0.1$ s can be described using a composite model unifying braking due to magnetic-dipole losses and due to processes internal to the neutron star. As the period increases, the braking index smoothly varies from $n = 3$ to $n = 0$; in magnetic-field calculations, the corrective factor $(1 + 5P^3)^{-1/2}$ must be introduced.

(7) The magnetic fields for sources of impulsive soft gamma-ray emission—magnetars—calculated using the most suitable internal model were equal to $(1.7–2.9) \times 10^{13}$ G; i.e., they do not exceed the critical magnetic field $B_{cr} = m^2c^3e\hbar = 4.4 \times 10^{13}$ G.

ACKNOWLEDGMENTS

This work was supported by the Russian Foundation for Basic Research (project code 97-02-17372) and the international program INTAS (grant no. 96-0154). The author would like to thank S.A. Suleĭmanova and V.D. Pugachev for help with the computations, L.B. Potapova for help in preparing the manuscript for publication, and an unpublished work referee for useful comments.

REFERENCES

1. J. H. Taylor, R. N. Manchester, A. G. Lyne, and F. Camilo, private communication (1995).
2. P. Goldreich and W. H. Julian, Astrophys. J. **157**, 869 (1969).
3. V. S. Beskin, A. V. Gurevich, and Ya. N. Istomin, Zh. Éksp. Teor. Fiz. **85**, 401 (1983) [Sov. Phys. JETP **58**, 235 (1983)].
4. Q. H. Peng, K. L. Huang, and J. H. Huang, Astron. Astrophys. **107**, 258 (1982).
5. L. H. Huang, R. E. Lingefelter, Q. H. Peng, and K. L. Huang, Astron. Astrophys. **113**, 9 (1982).
6. F. C. Michel and A. J. Dessler, Astrophys. J. **251**, 654 (1981).
7. F. C. Michel, Astrophys. J. **266**, 188 (1983).
8. R. N. Henriksen and D. R. Rayburn, Mon. Not. R. Astron. Soc. **166**, 409 (1974).
9. O. C. De Jager and H. J. Net, Astron. Astrophys. **190**, 87 (1988).
10. Y. Sang and G. Chanmugam, Astrophys. J. Lett. **323**, L61 (1987).
11. D. M. Sedrakyan and A. G. Movsisyan, Astrofizika **24**, 279 (1986).
12. V. S. Beskin, A. V. Gurevich, and Ya. N. Istomin, Usp. Fiz. Nauk **150**, 257 (1986) [Sov. Phys. Usp. **29**, 946 (1986)].
13. R. N. Manchester and J. H. Taylor, *Pulsars* (Freeman, San Francisco, 1977; Mir, Moscow, 1980).
14. L. D. Landau and E. M. Lifshitz, *The Classical Theory of Fields* (Fizmatgiz, Moscow, 1962; Pergamon, Oxford, 1975).
15. I. F. Malov, Astron. Zh. **75**, 281 (1998) [Astron. Rep. **42**, 246 (1998)].
16. J.-H. Huang, K.-L. Huang, and Q. H. Peng, Astron. Astrophys. **117**, 205 (1983).
17. Z.-G. Deng, J.-H. Huang, and X.-Y. Xia, Astrophys. Space Sci. **129**, 53 (1987).
18. I. S. Gradshteyn and I. M. Ryzhik, *Table of Integrals, Series, and Products* (Nauka, Moscow, 1971; Academic, New York, 1980).
19. C. Kouveliotou, S. Dieters, T. Strohmayer, *et al.*, Nature **393**, 235 (1998).
20. C. Kouveliotou, T. Strohmayer, K. Hurley, *et al.*, Astrophys. J. Lett. **510**, L115 (1999).
21. M. G. Baring and A. K. Harding, Astrophys. J. Lett. **507**, L55 (1998).
22. Yu. P. Shitov, *Physics of Neutron Stars* (St. Petersburg, 1999), p. 33.

Translated by D. Gabuzda

Astronomy Reports, Vol. 45, No. 5, 2001, pp. 395–408. Translated from Astronomicheskiĭ Zhurnal, Vol. 78, No. 5, 2001, pp. 459–473.

Measurement of the Turbulence in the Free Atmosphere above Mt. Maĭdanak

V. G. Kornilov and A. A. Tokovinin

Sternberg Astronomical Institute, Universitetskiĭ pr. 13, Moscow, 119899 Russia

Received February 10, 2000

Abstract—Stellar scintillations were measured at Mt. Maĭdanak during 42 nights in 1998–1999 in order to estimate the contribution of the free atmosphere to the seeing. The atmosphere above 1–2 km provides a median seeing of 0.″39, which is about one-third of the total seeing (0.″70). The characteristic altitudes of turbulent layers are from 3 to 11 km above the summit, and the appearance of layers at altitudes of 3–4 km is accompanied by a degradation of the free-atmosphere seeing. The median isoplanatic angle is $\theta_0 = 2.''30$ ($\lambda = 500$ nm, at the zenith). This is the first time that such data have been obtained for Maĭdanak.

The instruments used for these measurements—a modified four-channel photometer and a prototype of a double-aperture scintillation sensor—are described in detail. The data reduction was based on accurate corrections for photon-counting statistics and the use of theoretical weighting functions relating scintillation indices to the altitudes and intensities of turbulent layers. Simultaneous or quasi-simultaneous measurements of scintillation indices using apertures of different sizes having significantly different weighting functions enable estimation of the altitude and intensity of the equivalent turbulent layer. Despite the simplicity of this one-layer model, it provides fairly robust estimates of the integrated parameters of the real free atmosphere. © *2001 MAIK "Nauka/Interperiodica".*

1. INTRODUCTION

Studies of the optical parameters of the atmosphere have gained special importance in the context of the recent vigorous progress in the development of techniques for astronomical observations with high angular resolution, such as adaptive optics and interferometry. In addition to traditional seeing measurements, knowledge of the outer turbulence scale [1], the vertical profile of the turbulence, and the wind-velocity profile is required. These additional parameters of the atmosphere have begun to be measured at observatories with better-than-average seeing.

Mt. Maĭdanak in the Uzbekistan Republic (2600 m above sea level) provides an example of such an observatory site. Basic information about this site and results of previous astro-climatic studies can be found, for example, in [2]. A new stage in the study of the astroclimate at Mt. Maĭdanak began when a differential blurring monitor was mounted, and a continuous set of seeing measurements was obtained over more than a year [3]. The median seeing (0.″70) at Mt. Maĭdanak proved to be competitive with that at Serro Paranal in Chile (0.″66 [4]) or Rogue de los Muchachos in the Canary Islands (0.″64 [5]). It is natural that interest in the site was expressed by the European Southern Observatory, which organized a campaign to measure the seeing, outer turbulence scale, and other parameters in 1998. The measurements were carried out using the ESO Differential Image Motion Monitor (DIMM) [3] and the GSM instrument developed at the University of Nice [1, 6]. During the program, we measured stellar scintillations using apertures with various shapes, in order to obtain supplementary data on the properties of the atmospheric turbulence.

Here, we describe a technique for studying turbulence in the free atmosphere based on stellar-scintillation measurements and some of the results obtained. In particular, we present estimates for the characteristic altitudes and integrated intensities of turbulent layers, which, together with other data, provide tentative estimates for the relative contribution of the free atmosphere to the total seeing. Statistical data on the isoplanatic angle, which determines the field of view of an adaptive telescope, have been obtained for Maĭdanak for the first time.

2. THEORY

Turbulence in the upper layers of the atmosphere can be studied using measurements of stellar scintillations. For example, the vertical profile of the structure coefficient of the refraction index $C_n^2(h)$ can be determined from scintillations of binary stars using SCIDAR [7]. Given this profile, it is easy to derive the total contribution of the free atmosphere:

$$E_f = \int C_n^2(h)dh, \quad (1)$$

where the integration limits for the altitude are from about 1 km to the maximum altitude of the turbulence,

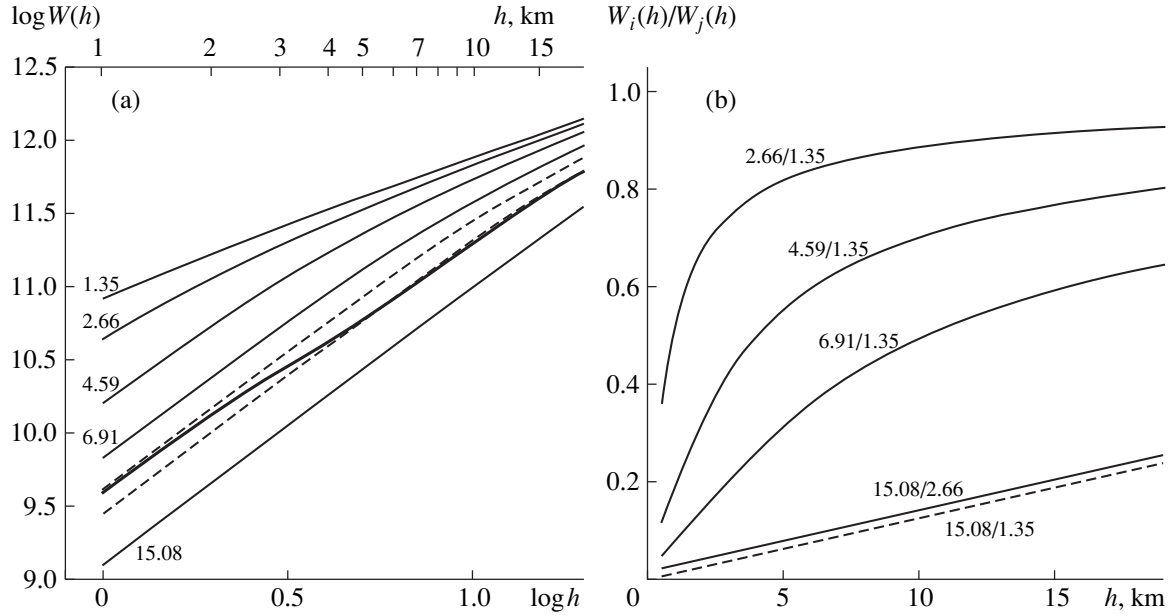

Fig. 1. (a) Weighting functions $W(h)$ for the set of entrance apertures used. The thick curve denotes the weighting function for the "isoplanatic" aperture and the dashed curve denotes that for apertures 5 and 6, which were used only in the summer of 1998. The diameters of the other apertures in cm are indicated. (b) Ratios of weighting functions for some pairs of apertures as a function of altitude h. The same functions can be understood as ratios of corresponding indices in a model with a single turbulent layer.

which is around 20 km. Comparison of E_f and the integral over the entire depth of the atmosphere $E = E_f + E_b$ provides quantitative estimates for the contributions to the total distortion of images from the free atmosphere and the boundary layer. Recall that, for a long exposure using a large telescope, the half-width of a stellar image β is related to the integral E and the wavelength λ by the expression [8]

$$\beta = 5.31\lambda^{-1/5}E^{3/5}. \quad (2)$$

The methods for estimating the influence of the free atmosphere considered below involve direct determination of the integrated turbulence E_f from stellar scintillations, rather than derivation of the vertical profile of the turbulence.

The scintillation index s^2, which is the dispersion of the natural logarithm of the intensity averaged over the aperture and measured for a fairly short exposure time, is also fully determined by the vertical profile $C_n^2(h)$. It is obviously equal to the dispersion of the flux fluctuations normalized to the mean-square flux. The theory of light propagation in weakly turbulent media (see [8–10] for more details) can be used to calculate s^2 as the integral of the vertical turbulence profile $C_n^2(h)$ with some weighting factor $W(h)$:

$$s^2 = \int_0^\infty C_n^2(h)W(h)dh, \quad (3)$$

where the weighting function is

$$W(h) = 5.21k^2\int_0^\infty f^{8/3}\sin^2(f^2h/2k)A(f)df. \quad (4)$$

Here, $k = 2\pi/\lambda$, f is the modulus of the spatial frequency, and the function $A(f)$ describes the shape of the entrance aperture. For example, for a circular aperture with diameter D, we obtain $A(f) = [2J_1(fD/2)/(fD/2)]^2$, where J_1 is a first-order Bessel function. In the case of non-monochromatic radiation, we must average over the corresponding spectral band, since the weighting function is wavelength-dependent.

Figure 1a presents weighting functions $W(h)$ calculated using (4) for various diameters of our aperture (see Table 1). These functions have been calculated for the V photometric band and the spectral energy distribution of an A0 star. We can see that the dependences in Fig. 1a are close to linear on a logarithmic scale. In the two limiting cases of infinitely small and infinitely large apertures, $W(h)$ is an exact power-law function of the altitude, with indices 5/6 and 2, respectively [8]. For real apertures in the considered altitude interval (from 1 to 20 km), $W(h)$ can be adequately approximated by power laws with indices between 5/6 and 2. An aperture is considered small or large compared to the size of the Fresnel zone, which in our case is about 7 cm. For small apertures, this index is roughly equal to unity, while it is about two for large apertures. It is the substantial difference between the weighting functions for apertures of

Table 1. Characteristics of differential weighting functions

Aperture number	1	2	3	4	7	8	9	0
Physical size, mm	0.30	0.59	1.01	1.52	1.91	2.29	3.32	2.16
Equivalent entrance aperture, cm	1.35	2.66	4.59	6.91	8.68	10.41	15.08	9.82
Approximating exponent α	0.89	0.99	1.16	1.38	1.54	1.67	1.85	1.67

different sizes that makes it possible to estimate the vertical distribution of $C_n^2(h)$.

The variable h in formulas (1), (2), and (3) has the meaning of distance along the line of sight, and coincides with altitude only for measurements at zenith. Scintillation indices or derived parameters obtained at various zenith distances z must be reduced to values at zenith ($z = 0$). This is straightforward, provided the weighting functions have power-law dependences on the altitude and the dependence on the zenith distance can be taken outside the integral. In practice, power-law approximations of the real weighting functions can be used (Table 1). In this case, the error does not exceed 2% for $z < 35°$ for medium-size apertures; for the smallest and the largest apertures, it is much smaller.

The isoplanatic angle of the atmosphere θ_0 describes the size of the field of view of an adaptive telescope [11]. It can also be determined using the integral $C_n^2(h)$, but with the weighting factor $h^{5/3}$:

$$\theta_0^{-5/3} = 2.91k^2\int_0^\infty C_n^2(h)h^{5/3}dh. \quad (5)$$

It was noted some time ago [12] that the weighting function $W(h)$ for a 10-cm aperture is rather close to $h^{5/3}$. Consequently, the scintillation index for this aperture can be used to estimate the isoplanatic angle. The 10-cm aperture with central screening of 0.4, for which the weighting function is closer to $h^{5/3}$, provides even better results. The isoplanatic angle θ_0 at the zenith is calculated using the scintillation index $s_{\rm iso}^2$ measured for such an "isoplanatic" aperture at a zenith distance z:

$$\theta_0 = A'(\sec z)^{8/5}(s_{\rm iso}^2)^{-3/5}, \quad (6)$$

where the coefficient A' is determined from the condition that the proximity of $W(h)$ to an $h^{5/3}$ dependence be uniform in the altitude interval from 1 to 20 km. This relation provides estimates for the isoplanatic angle with accuracy $\pm 2\%$, even for the most unfavorable vertical turbulence distribution. Since θ_0 depends on the wavelength [see (5)], the coefficient A' contains a factor to translate the isoplanatic angle to a wavelength of 500 nm; its values are 0.206, 0.197, and 0.188 for the B, V and R scintillation indices, respectively.

The effective altitude of turbulence, which is naturally defined to be

$$h_{\rm eff} = \int_0^\infty C_n^2(h)hdh/\int_0^\infty C_n^2(h)dh, \quad (7)$$

is a supplementary integrated parameter of the atmospheric turbulence. In addition to being very important for the description of the global properties of a given site, it also provides a relation between the scintillation index in a small aperture, for which the weighting function is roughly proportional to the altitude, and the integral $C_n^2(h)$ over the entire depth of the atmosphere E. Indeed, for such an aperture, $W(h_{\rm eff})h \approx W(h)h_{\rm eff}$, and it follows from (7) that

$$s^2 \approx W(h_{\rm eff})E. \quad (8)$$

The effective altitude of turbulence can also be specified in another way: from the ratio of the scintillation indices for two different apertures, using, for example, a power-law approximation for the weighting functions $W_1(h) \sim h^{\alpha_1}$ and $W_2(h) \sim h^{\alpha_2}$:

$$(h_{\rm eff}^*)^{\alpha_2-\alpha_1} \sim \int_0^\infty C_n^2(h)W_2(h)dh/\int_0^\infty C_n^2(h)W_1(h)dh, \quad (9)$$

where, for the sake of definiteness, $\alpha_2 > \alpha_1$; i.e., the first aperture is smaller then the second.

These two values for the effective altitude of turbulence can differ substantially, depending on the behavior of the function $C_n^2(h)$ in the boundary layer. However, if we consider them only in the free atmosphere by setting a lower integration limit in (7) and (9) above the depth of the boundary layer (≈1 km), these heights become similar. In addition, their difference can be shown to decrease with decrease of $\alpha_2 - \alpha_1$. They coincide with each other and with the geometrical height h, provided there is only one turbulent layer. In any case, $h_{\rm eff}^*$ provides an upper limit for $h_{\rm eff}$.

Figure 1b presents ratios of the weighting functions for various pairs of apertures. Despite the fact that these are equal to the ratios of the corresponding scintillation indices only in the case of a single turbulent layer, the dependences in Fig. 1b can be used to determine the effective altitude in the sense of (9). The easiest way is to use a large and small aperture pair, for which the

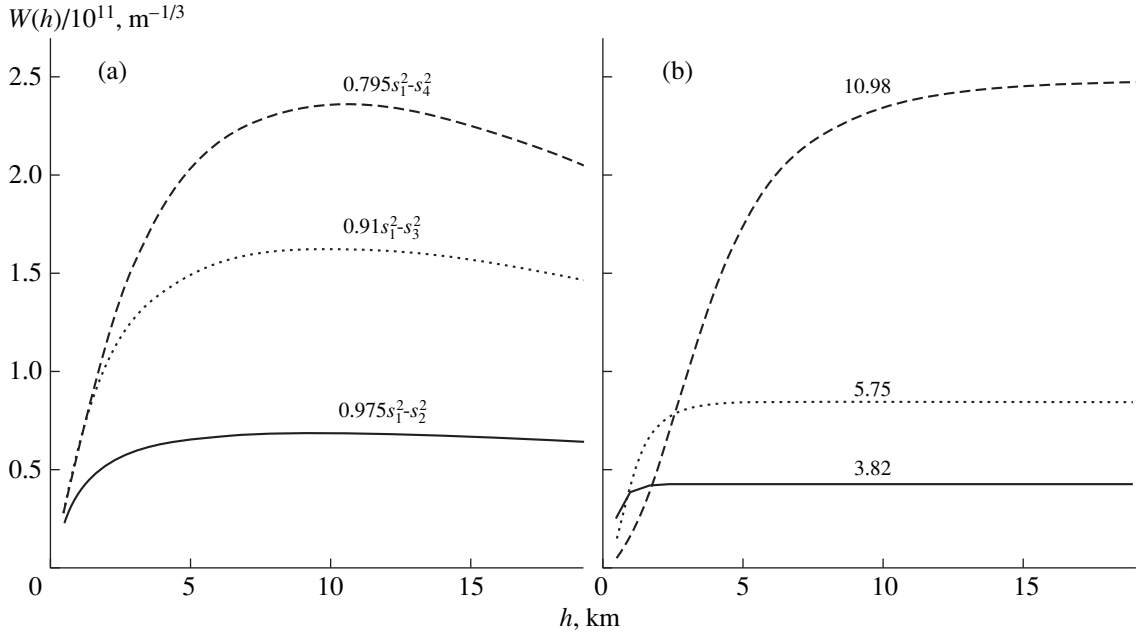

Fig. 2. (a) Differential weighting functions for some pairs of apertures as a function of altitude h. The coefficients were selected so that the functions were constant within the altitude interval considered. (b) Weighting functions for three apertures of the DASS as a function of altitude h. The outer diameters for the apertures in cm are indicated.

ratio of the weighting functions depends on the altitude essentially linearly. This is natural, since the weighting function for a small aperture is roughly proportional to the altitude, while that for a large aperture is proportional to the square of the altitude. In the case of 15.08- and 1.35-cm apertures, for our calculated weighting functions, we obtain the following calibration relation:

$$h^*_{\rm eff} = 80.2(s^2_{15.08}/s^2_{1.35}) - 0.2 \text{ km}. \quad (10a)$$

For 6.91- and 1.35-cm apertures, we obtain in a linear approximation

$$(h^*_{\rm eff})^{0.5} = 5.46(s^2_{6.91}/s^2_{1.35}) + 0.8 \text{ km}, \quad (10b)$$

with accuracy better than 10% (a cubic approximation $(h^*_{\rm eff})^{0.5}$ provides accuracy better than 2%).

Having thus determined $h^*_{\rm eff}$ and assuming that $h_{\rm eff}$ coincides with $h^*_{\rm eff}$ in the free atmosphere, we can derive from (8) the integrated intensity of the turbulence in the free atmosphere $E_f = s^2/W(h^*_{\rm eff})$.

Table 2. Characteristics of DASS apertures and their weighting functions

Apertures	B'	Altitude $h_{0.5}$, km	$W^s/10^{11}$, m$^{-1/3}$	$W_d(3\,\text{km})/W^s$
1–2	0.975	0.84	0.68	0.86
1–3	0.910	1.41	1.60	0.78
1–4	0.795	2.05	2.30	0.66

The uncertainty in this approach is that the altitude of the lower boundary of the free atmosphere is not specified, and depends on the real vertical distribution of the turbulence. Its advantage—stability to noise—is manifest in the case of a large and small aperture pair.

An estimate of the integrated turbulence in the free atmosphere can also be made with another method, using only small apertures. Figure 2a presents simple linear combinations of the weighting functions for pairs of apertures of the form $W_{12}(h) = B'W_1(h) - W_2(h)$. For each pair, coefficient B' is selected so that the difference remains essentially constant (±5%) in the considered altitude interval. Its behavior above 20 km is insignificant. The differential weighting function depends on the sizes of the apertures, and is described by the saturation W^s and altitude $h_{0.5}$ corresponding to 0.5 of the saturation value. The actual values for three pairs of apertures are presented in Table 2.

The differences in the weighting functions correspond to the same differences in the scintillation indices, without any limitations on the vertical distribution of the turbulence. Consequently, the integrated intensity in the free atmosphere (starting approximately from the altitude $h_{0.5}$), for example, for 1.35- and 2.66-cm apertures, is calculated as

$$E_f = (0.975s^2_{1.35} - s^2_{2.66})/W^s_{12}. \quad (11)$$

Although this method yields more definite results than the effective-altitude method, it is obviously more sensitive to noise.

The double-aperture scintillation sensor (DASS) [13] makes it possible to determinate the integrated turbulence in the free atmosphere with even higher accuracy. This technique is based on measurement of the differential scintillation index s_d^2; i.e., the dispersion of the natural logarithm of the ratio of the fluxes I_2 and I_1 for two concentric apertures, one circular and one annular: $s_d^2 = \langle(\Delta \ln(I_1/I_2))^2\rangle$.

The corresponding weighting function $W_d(h)$ is essentially constant starting from some altitude. Figure 2b presents these functions calculated for three of the apertures used. We can see that, compared to the differential weighting functions (Fig. 2a), they initially increase more sharply and are substantially more constant for other altitudes. Table 3 presents the values characterizing these functions indicated above, together with the outer diameters of the apertures.

The integrated turbulence in the free atmosphere is determined from the expression

$$E_f = s_d^2/W^s. \quad (12)$$

The ordinary scintillation indices in each aperture are measured along with the differential scintillation index. The weighting function for a small, central aperture is roughly proportional to the altitude, so that relation (8) for the effective height of the turbulence h_{eff} can be applied.

Using the generalized SCIDAR principle [7], we can also determine the total integral of distortions E over the entire depth of the atmosphere. To this end, it is sufficient to place an annular aperture at some distance from the exit pupil of the telescope, rather than at the pupil, which corresponds to a sort of additional propagation of the light along a turbulence-free path. In other words, the "lens + telescope" optical system will form an image (in this instance, imaginary) of the exit aperture a substantial distance behind the telescope. If the path length exceeds the initial distance interval where the weighting functions increase, the entire atmospheric turbulence falls within the interval with constant weight, which is required to measure the total integral.

The seeing β_{free} determined by distortions in the free atmosphere is a convenient parameter for estimating the contribution of these distortions to the total seeing, generally measured using standard astro-climatic techniques. The seeing reduced to the standard wavelength of 0.5 μm and expressed in arcseconds is calculated using the formula

$$\beta_{\text{free}} = 1.99 \times 10^7 E_f^{3/5}. \quad (13)$$

The exact meanings of E_f, h_{eff}^*, and β_{free} depend on the chosen measurement method, which specifies the corresponding weighting functions. Nonetheless, these quantities are useful for comparative analyses of the roles of the boundary layer and the free atmosphere in astronomical image distortion.

3. INSTRUMENTATION AND TECHNIQUE

Scintillations were measured with a 60-cm Cassegrain telescope (focal length of about 7.5 m) of the Maĭdanak Observatory in 1998 and 1999 using a four-channel *WBVR* photometer. To experimentally verify the ideas presented above, a prototype of a double-aperture scintillation sensor was used during three nights in 1998. In this Section, we will briefly describe these instruments and the observations and data reduction.

A four-channel *WBVR* photometer [14, 15] with beam splitting between the channels provided by dichroic mirrors was chosen for our study of stellar scintillations for the following reasons: (1) it is permanently mounted on the 60-cm telescope and could be used for these measurements over a long period of time; (2) it provides flux detections with accumulation times of 1 ms and shorter; (3) it provides simultaneous flux measurements in the four spectral bands; and (4) it is equipped with a computer-controlled mechanism for rapid changing of the field diaphragms. A detailed optical schematic of the photometer is given in [15].

We modified the four-channel photometer for the stellar scintillation measurements. The focal plane was shifted about 170 mm towards the telescope. In the new focal plane, we mounted a 2-mm field diaphragm (with an angular size of about 1′) and, directly behind it, an additional lens with a focal length of 160 mm, which forms an image of the entrance pupil in the former focal plane. In this way, field diaphragms with a step motor with an accuracy of about 10 μm placed in this plane and on the optical axis become pupil diaphragms (apertures). Since the additional lens was displaced from the optical axis by about 4 mm, the image of the non-obscured segment of the main telescope mirror fell into the pupil diaphragms, and further on the beam-splitting elements. The focal length of this lens was chosen to provide the necessary interval for the effective entrance apertures.

Another additional lens was introduced on the optical axis, together with a wide-field monitoring mirror. Its purpose was to form an enlarged image of the field diaphragm in the focal plane of the eyepiece, in order to center the measured star accurately.

Resetting of the diaphragms is computer controlled, and takes, on average, 0.11 s. Damping of vibrations in the disk after it has stopped lasts another 0.02 s. Table 1 presents the linear sizes of the diaphragms and equivalent entrance apertures. The central screening of the last aperture, used to measure the isoplanatic angle, is 0.4 of its size. The errors in the sizes do not exceed 5% for small and 2% for large diaphragms.

An operational prototype of the Double-Aperture Scintillation Sensor (DASS) was quickly assembled (May–June, 1998) on the basis of the available blocks for the four-channel photometer. The DASS includes only two photomultipliers: one measures the flux I_1 in the annular diaphragm while the other measure the flux I_2 in the inner circular diaphragm.

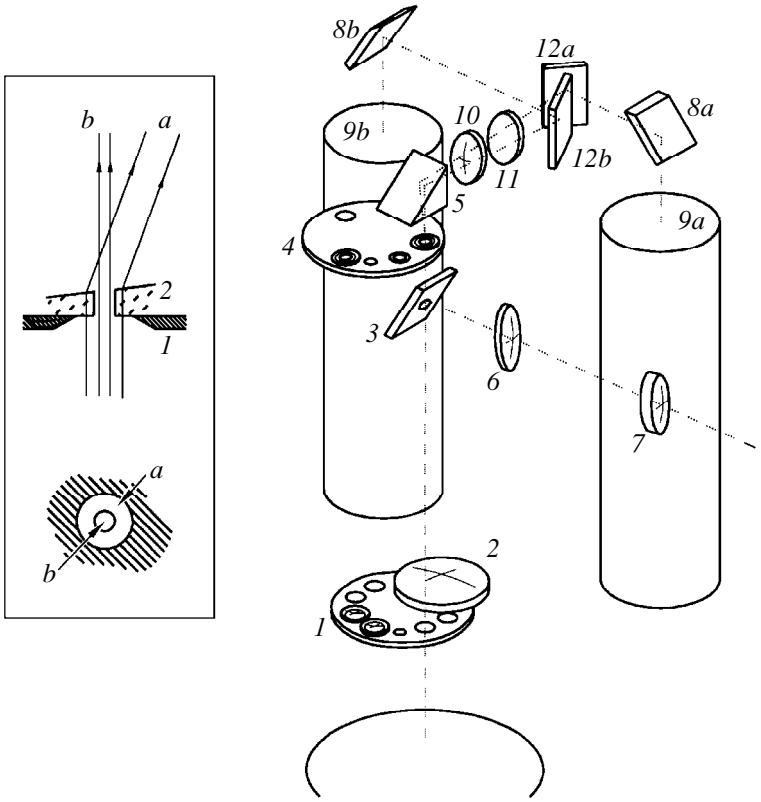

Fig. 3. Simplified optical schematic for the prototype of the differential scintillation sensor. See text for details.

Figure 3 presents a simplified optical schematic for the instrument. The focused light of a star passes through one of the focal diaphragms on disk *1* and lens *2* with focal length 160 mm. The image of the pupil is formed on a second disk with exchangeable diaphragms *4*, three of which contain microprisms with a central hole, which determine the parameters of the double aperture. As shown in the inlay in Fig. 3, the central portion of beam *b* passes through the hole without deviation, while the annular zone *a* is deflected slightly by the microprism. Both beams are deflected by the auxiliary prism *5*, and lens *10* again forms an image of the focal plane near the splitting mirrors *12a* and *12b*; a *V*-band filter *11* is located in front of these.

In this way, the annular and central apertures form two separate images of the entrance diaphragm near mirror *12ab*. Further, both beams are deflected by mirrors *8a* and *8b* toward the photocathodes of photomultipliers *9a* and *9b*, which measure the fluxes in the annular and inner circular apertures. To measure the isoplanatic angle, there is a diaphragm with central screening 0.4 in disk *4*, similar to that in the four-channel photometer. Naturally, in this case, light falls on only one photomultiplier.

Only part of the image of the telescope pupil passes through the hole in mirror *3*; the remainder serves as an observation of the image of the star, which is formed by lens *6* with eyepiece *7* for the purpose of guiding.

We used three double apertures of different sizes with the ratio of the inner to the outer diameters equal to 0.5. Table 3 presents the outer diameters of the annular apertures projected onto the entrance pupil of the telescope, together with the parameters of the corresponding weighting functions.

Two diaphragms with positive lenses are available for the realization of the generalized SCIDAR mode in the disk with the focal diaphragms. The focal lengths of these lenses are 30 and 15 mm, which corresponds to "shifts" of the entrance aperture to –2 and –4 km. In this case, the weighting functions corresponding to diaphragms *1* and *3* are already close to saturation (Fig. 2b), and the measurements correspond to the integrated effect of the entire atmosphere. However, the total range of sight measured in this way was between 1″ and 1″.5, which is systematically higher than simultaneous DIMM and

Table 3. Characteristics of the photometer aperture set

Apertures	Diameter, cm	Altitude $h_{0.5}$, km	$W^s/10^{11}$, $m^{-1/3}$	$W_d(3\,km)/W^s$
1	3.82	0.4	0.43	1.00
2	10.98	3.5	2.45	0.41
3	5.75	1.0	0.85	0.91

GSM estimates. The reason for these discrepancies is probably the presence of strong dome turbulence. Intense and slow distortions were seen on the 60-cm telescope with a Foucault blade. Similar effects also occurred on the 1.5-m telescope; in both cases, the seeing improved toward the morning. We will not consider the results of the integrated seeing measurements obtained with the DASS prototype further here.

The real-time detection of the signal and reduction of the measurements were essentially the same for the DASS and four-channel photometer. Both instruments work in a photon-counting regime and have the same type of high-speed impulse amplifiers. We used electronic instrumentation from the four-channel photometer for the DASS, in particular, counters with a response rate of 100 MHz in a specially-designed interface in a personal computer.

The duration of an individual signal accumulation (microexposure) obviously affects the measured scintillation index, since the power of the flux fluctuations is partially lost on timescales shorter than the accumulation time. Figure 4 presents the results of specialized measurements with various accumulation times for diaphragm *3* of the DASS (equivalent entrance aperture 5.75 cm). We can see that, for 1-ms microexposures, the loss for the central and annular apertures does not exceed 0.03, and is ≈0.1 for the differential scintillation index. This is due to the fact that low-frequency fluctuations are suppressed in the differential signal. On the other hand, if a microexposure is too short, the statistical noise dominates in the signal, even for bright stars, and the corresponding errors can also distort the measured values. In our opinion, microexposures of 1 ms (0.99 ms for accumulation, 0.01 ms for a pause between microexposures) represent a reasonable compromise.

A correction for the finite accumulation time can be found by extrapolating the indices obtained with 1-ms and 2-ms accumulations. In this case, a series with 2-ms microexposures is formed from two-element combinations (binning) of the initial 1-ms series. We plan to apply this procedure in future scintillation measurements.

For the measurements with the photometer and double-aperture scintillation sensor, we used a slightly modified version of the standard OPERA-VI code, which controls the photometer and measurement process during ordinary photometric observations. A program block was added to calculate the required statistical parameters of the light flux and (during operation of the four-channel photometer) periodically change the aperture diaphragms.

Let us first consider a measurement cycle with the photometer. We measured the scintillation indices quasi-simultaneously in eight (six, in 1999) apertures and in the *B*, *V* and *R* channels. The data from the *W* channel were not used due to their insufficient statistical accuracy, even for bright stars. In our case, "quasi-simultaneous" means that the cycle of consecutive estimations of the scintillation indices in all three apertures

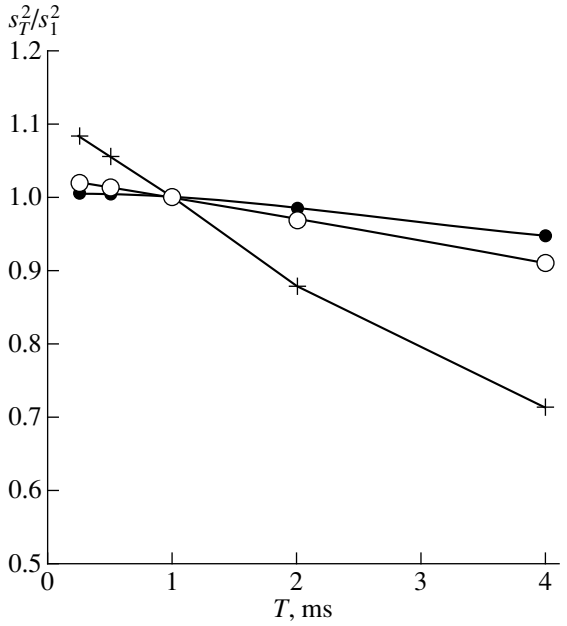

Fig. 4. Detected intensity as a function of accumulation time *T*, normalized to the intensity for a 1-ms accumulation. The measurements were made with the DASS and aperture 3. The crosses show the differential index, the circles the central index, and the dots the scintillation index for the annular aperture.

was much shorter than the time to complete an individual measurement of these values. The time for a complete measurement is limited from above by the characteristic time over which scintillation can be considered a steady-state process. On the other hand, replacement of an aperture should not occupy a considerable fraction of the total time, which imposes restrictions on the minimum time for estimation of the indices with the current aperture.

Based on these considerations, we chose to use a measurement cycle in which 1000 counts with 1-ms exposures were accumulated with each aperture. About 15% of the total time was lost due to aperture switching. A series of measurements with all eight apertures takes roughly 9 s. This series is repeated 26 times (33 times for the measurements with six apertures), so that the total time to obtain one estimate of the scintillation indices is 4 min. The total time for measurements with the scintillation sensor was usually 50 s.

The real-time reduction procedure for the measurements consisted of the following.

(1) For a series of 1000 counts obtained simultaneously in the three channels, we calculated the mean $\bar{n}'_B$, $\bar{n}'_V$, and $\bar{n}'_R$ values; dispersions $\sigma_B^{2'}$, $\sigma_V^{2'}$, and $\sigma_R^{2'}$; and covariances cov'_{BV}, cov'_{BR}, and cov'_{VR} in the usual way (for the DASS measurements, $\bar{n}'_1$, $\bar{n}'_2$, $\sigma_1^{2'}$, $\sigma_2^{2'}$, and cov'_{12} were calculated).

(2) We corrected the calculated statistical parameters for the non-linearity of the detectors, which is essential for measurements with large entrance apertures (for aperture 9 of the photometer and the star α Lyr, the flux of impulses reached 2×10^6 pulse/s). In a linear approximation, which works well for fluxes below $\sim 3 \times 10^6$ pulse/s, we determined the true means and second moments from the formulas

$$\begin{aligned} \bar{n}_i &= \bar{n}_i'(1 + \bar{n}_i'\tau_i), \\ \sigma_i^2 &= \sigma_i^{2'}/(1 - 2\bar{n}_i'\tau_i)^2, \\ \mathrm{cov}_{ij} &= \mathrm{cov}_{ij}'/((1 - 2\bar{n}_i'\tau_i)(1 - 2\bar{n}_j'\tau_j)), \end{aligned} \tag{14}$$

where a prime denotes values obtained in step 1 and τ is a non-linearity parameter specific to each photometric channel.

(3) Next, we determine the statistical parameters of the scintillations—the indices s_B^2, s_V^2, and s_R^2 and the differential indices s_{BV}^2, s_{BR}^2, and s_{VR}^2 (for the DASS measurements, s_1^2, s_2^2, and s_d^2)—using the relations

$$\begin{aligned} s_i^2 &= (\sigma_i^2 - p_i\bar{n}_i)/(\bar{n}_i - \bar{b}_i)^2, \\ s_{i-j}^2 &= s_i^2 + s_j^2 - 2\mathrm{cov}_{ij}/((\bar{n}_i - \bar{b}_i)(\bar{n}_i - \bar{b}_i)), \end{aligned} \tag{15}$$

where *i* and *j* are the *B*, *V* and *R* channels for the photometer and *1* or *2* for the scintillation sensor. The quantity $\bar{b}_i$ is the sky background in a given channel, and p_i is the so-called non-Poisson coefficient, which is close to unity.

(4) The resulting values were summed (six indices and three means for each of eight or six apertures for the measurements with the four-channel photometer, or three indices and two means for measurements with the DASS). At the end of the entire process, averages with their rms errors were calculated, displayed on a monitor, and stored in a data file.

Since the average was used for each 1 s estimate of the second moments, this rather effectively filtered out the influence of slow variations of the signal due to the motion of the star in the field diaphragm (which was 1′ for the telescope used), low-frequency scintillations, and variations in opacity. Since the real sky background is much lower than the flux from the stars, even on moonlit nights, a crude estimate for this background can be used in (15).

We can see from (14) and (15) that the resulting scintillation indices are affected by two instrumental parameters for each photometric channel. The first, τ, must be determined with a relative accuracy of ≈0.1 if we wish to achieve a ≈3% accuracy in the indices for measurements at the maximum fluxes. The non-linearity of photometric channels for both instruments was periodically studied using a method based on the influence of the non-linearity on the measured statistical parameters of Poisson-type fluxes [16]. The slope of the dependence between the ratio $p = \sigma^2/\bar{n}$ and the flux is related to the non-linearity parameter τ (sometimes called the dead time). This method estimates the non-linearity parameter with an accuracy better than 5%. Within these limits, τ is constant and, depending on the channel, equal to 28–31 ns. The impact of τ on measurements of indices with small apertures is obviously negligible.

The same auxiliary measurements make it possible to determine the second parameter, the non-Poisson coefficient *p* for small fluxes. Ideally, this should be unity; in reality, however, it differs slightly from unity for a number of reasons (after-pulses of the photomultiplier, "ringing," noise pick-up, etc.). It follows from (15) that the error Δ*p* gives rise to an error in the scintillation index $\Delta p/\bar{n}$, and correct reduction of the measurements for small fluxes (with diaphragms *1* and *2*) requires that the accuracy in *p* be no worse than 0.01. For example, the coefficients *p* determined from measurements in July 1998 in the *B*, *V*, and *R* channels were 0.997, 0.994, and 1.002, respectively, with the error Δ*p* roughly equal to 0.003. We determined the parameters of the photometric channels in each season of stellar scintillation measurements. In addition, we verified the correctness of the instrumentation and data reduction using measurements of a constant light source (light-emitting diode) with a flux corresponding to the stellar fluxes. We also measured the extremely weak scintillation displayed by Jupiter.

Based on the above considerations, we used bright stars: α Lyr, α Cyg, α And, and α Aur. For the faintest of these, α And, $V = 2\overset{m}{.}05$. The data indicate that, for this star, there begins to be a deficit of light in the smallest aperture. However, since the weighting functions and, accordingly, the scintillation indices are only weakly sensitive to variations of the spectral band, we can move $\approx 0\overset{m}{.}5$ toward fainter stars by removing the photometric filters from the photometric channels [15].

4. RESULTS

General information. A complete summary of the scintillation measurements made with the instrumentation described here is presented in INTAS Reports [17, 18]; electronic versions can be obtained from the authors. Table 4 presents the general statistical data for the measurements that have been made thus far. The following data are presented for each series of observations: the dates of the beginning and end of the measurements, the total duration of the measurements in hours, the number of complete measurements (separately for the DASS, and with the number of isoplanatic-angle measurements in brackets), the instrument used, and the observers.

We stress again that our observations with the DASS prototype were carried out to verify the new technique for measuring the seeing, while the observations with the four-channel photometer were intended for a long-

Table 4. General information about the scintillation measurements

Season	Beginning and end dates	Number of hours	Number of measurements	Instrument	Observers
1	July 17–19, 1998	19	183(409)	DASS	O. Vozyakova, V. Kornilov, A. Tokovinin
	July 20–25, 1998	30	377	Photometer	
2	July 24–August 8, 1999	97	1288	Photometer	O. Vozyakova, V. Kornilov
3	September 26–October 12, 1999	132	1765	Photometer	S. Il'yasov, T. Sadibekova

term study of the scintillations aimed at obtaining supplementary data on the atmospheric turbulence at Maĭdanak.

The 1998 measurements were carried out with the complete set of apertures. Our analysis indicates that apertures 7 and 8 (Table 3) can be excluded from further measurements. Figure 1a also confirms that these apertures essentially reproduce the measurements with the "isoplanatic" aperture.

Table 5 presents characteristic values for the scintillation indices and their relative errors calculated assuming that consecutive estimates are statistically independent. These values are medians of the distributions for four-minute measurements of α Cyg in the *V* channel obtained during season 2. The data presented show that the measurement errors are determined primarily by the scintillation process rather than by quantum statistics.

We used the *V*-channel scintillation indices for further analysis, while the data in the *B* and *R* channels were used to check the results. Further, we plan to use the entire data set to reconstruct the vertical distribution of the turbulence.

Isoplanatic angle. Figure 5 presents a histogram of all estimates of the isoplanatic angle derived from the scintillation indices in the "isoplanatic" aperture in the *V* band. The θ_0 values determined from the *B*, *V*, and *R* data coincide to better than 2%. In addition, an appreciable part of the small deviations can be explained as a result of the effective height of the turbulent layer, providing evidence for the reliability of our measurements and the validity of the theoretical models used. Table 6 presents numerical values for the levels of the cumulative distribution θ_0.

The median isoplanatic angle is $2\farcs30$, which is typical for good observatory sites. For example, the study [19] gives isoplanatic angles from $1\farcs3$ to $3\farcs0$ for Mauna Kea; the few available data on vertical atmospheric sounding above Paranal yield $\theta_0 = 3\farcs0$ [4]. Season-to-season variations are small, and the cumulative distributions for the isoplanatic-angle estimates are similar to each other. These are the first such data to be obtained for Maĭdanak.

The effective altitude of the turbulence and the integrated turbulence in the free atmosphere are related via the scintillation index in a small aperture, as shown in Section 2. Therefore, these parameters were determined simultaneously both from the ratio of the scintillation indices for large and small apertures ($h^*_{\rm eff}$) and from differences in the indices for small apertures ($h_{\rm eff}$). Figure 6a presents a comparison between the altitude $h^*_{\rm eff}$ calculated from the ratio of the indices for the 1.35- and 6.91-cm apertures [see (10b), cubic approximation] and $h_{\rm eff}$, obtained from (8) using estimates for the integrated turbulence E_f. Here, E_f is determined from the difference of the indices for 1.35- and 4.59-cm apertures [see (11)].

The average behavior of this dependence can be understood as follows: (1) below 4 km, the differential method underestimates the integrated turbulence and, hence, overestimates $h_{\rm eff}$; (2) from 4 to 10 km, there are usually two (or more) turbulent layers present, which results in overestimation of the altitude $h^*_{\rm eff}$; (3) above 10 km, only turbulence in the tropopause is important, and the two heights coincide; (4) $h_{\rm eff}$ values are overestimated above 12 km due to their appreciably non-normal error distribution (the difference of the indices is of the order of the errors). Similar dependences are found when the effective heights are determined from measurements in other apertures.

The errors in the effective heights were estimated based on the measured errors for the scintillation indices and formulas (8), (11), and (10). Typical relative errors for $h^*_{\rm eff}$ are 0.04 and 0.06 using (10a) and (10b), respectively. The relative errors do not depend on altitude. The relative errors in $h_{\rm eff}$ increase with altitude, and their characteristic values at 10 km are 0.20, 0.13, and 0.11 for the index differences (1–2), (1–3), and (1–4), respectively. In this case, the absolute errors increase faster than the altitude (roughly as $h^{1.5}$), as can be seen in Fig. 6a. Taking this into account, we will specify the effective height $h^*_{\rm eff}$ based on the index ratio $s^2_{6.91}/s^2_{1.35}$ (10b).

Table 5. Characteristic scintillation indices and their relative errors

Aperture number	1	2	3	4	0	9
Scintillation indices	0.108	0.091	0.064	0.041	0.021	0.011
Relative errors	0.05	0.04	0.04	0.04	0.04	0.04

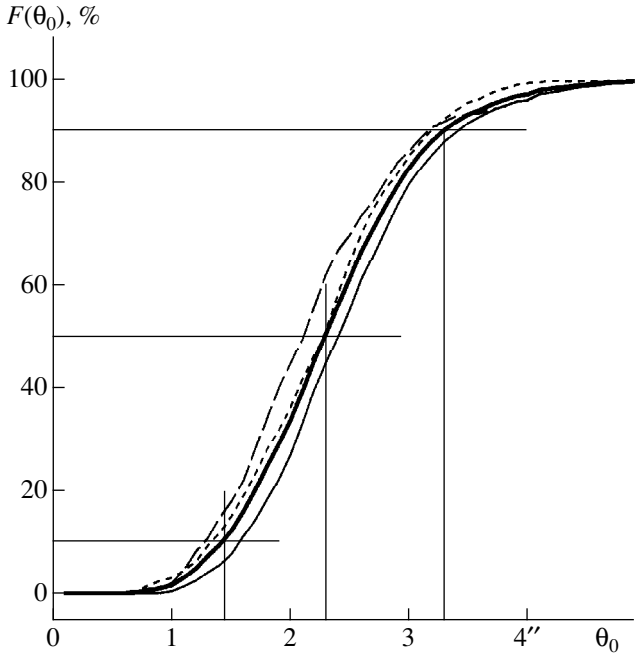

Fig. 5. Cumulative distribution for the isoplanatic angles for three measurement seasons (summer 1998—long dashes; summer 1999—short dashes; autumn 1999—thin solid curve) and their integrated distribution (thick solid curve).

Figure 6b presents distributions for $h^*_{\rm eff}$ for three measurement seasons. The distributions for seasons 2 and 3 are appreciably different: in season 2, effective heights from 3 to 6 km dominated, while the dominant effective heights in season 3 were from 6 to 10 km. It appears that, in the latter case, there was usually a single turbulent layer in the tropopause, whereas, in the former case, an additional low layer of intense turbulence dominated. The altitude distribution for season 1 includes both features. Note that the first two seasons fell in periods of unstable weather conditions associated with passing atmospheric fronts. The third season (autumn 1999) was characterized by stable, good weather.

Analyzing the measurements for individual nights, we can see that, as a rule, the effective height of the turbulent layer sharply decreased during characteristic bursts of scintillations lasting 15–30 min. This provides evidence for the passage of a low layer (area) of increased turbulence several kilometers in size across the line of sight.

Table 6. Characteristics of cumulative distribution for isoplanatic angle

Levels	Season 1	Season 2	Season 3	All measurements
$F(\theta_0) = 10\%$	1.″29	1.″33	1.″57	1.″44
$F(\theta_0) = 50\%$	2.12	2.28	2.40	2.30
$F(\theta_0) = 90\%$	3.19	3.20	3.43	3.32

The integrated turbulence in the free atmosphere E_f is presented below as the contribution of the free atmosphere to the seeing (the half-width of the turbulent image of a star in a large telescope) $\beta_{\rm free}$ [see (13)]. We determined the seeing from both our DASS and photometer measurements. It follows from Section 2 that the DASS provides the most reliable seeing estimates; however, the small number of measurements with the DASS prototype prevented a complete statistical analysis of the data.

Figure 7 presents a comparison between the seeing for the entire atmosphere (estimated using GSM and DIMM data) and the contribution of the free atmosphere $\beta_{\rm free}$ (estimated using the DASS data for two of three observational nights when this instrument was used). On July 18, we used apertures 1 and 2, while aperture 3 was used on July 19; strictly speaking, the meanings of $\beta_{\rm free}$ for these three apertures are somewhat different. However, a comparison between the results obtained with the different apertures shows that they are virtually indistinguishable. The effective height of the turbulence on July 18 was, on average, 7–8 km, while it was 4–5 km on July 19; i.e., in all cases, the turbulent layers were in the area of saturation for the weighting functions of the corresponding apertures (Fig. 2b).

Figure 7 also show a good agreement between the estimates of the total β obtained with different astro-climatic instruments. On July 18, when the seeing was close to its median value, the dominant contribution was made by the boundary layer. On July 19, when the image quality was better, the situation was similar; toward morning, however, the turbulence in the free atmosphere increased and the image quality deteriorated.

As a more dramatic example, Fig. 7 presents data for two nights of season 1 (photometer measurements). The denser series of estimates of $\beta_{\rm free}$ clearly indicate that, on these nights, not only did the total seeing vary substantially during a single night, but the contribution of the free atmosphere also varied from ≈15% (July 23, $18^{\rm h} - 19^{\rm h}$ UT) to ≈60% (during the bursts of July 22 around $17^{\rm h}$, $18^{\rm h}30^{\rm m}$, and $22^{\rm h}$ UT).

For the photometer data, we determined $\beta_{\rm free}$ using two methods, as was done for the effective heights: using the effective height $h^*_{\rm eff}$ (10b) and formula (8) (further, we denote this value $\beta^*_{\rm free}$), and using differences of scintillation indices in small apertures (11). The resulting E_f were then transformed into the seeing using (13).

We estimated the errors in $\beta_{\rm free}$ in the same way as those for the effective heights. For example, the relative errors in $\beta^*_{\rm free}$ are essentially independent of this parameter; their median value is 0.032. Accordingly, the absolute

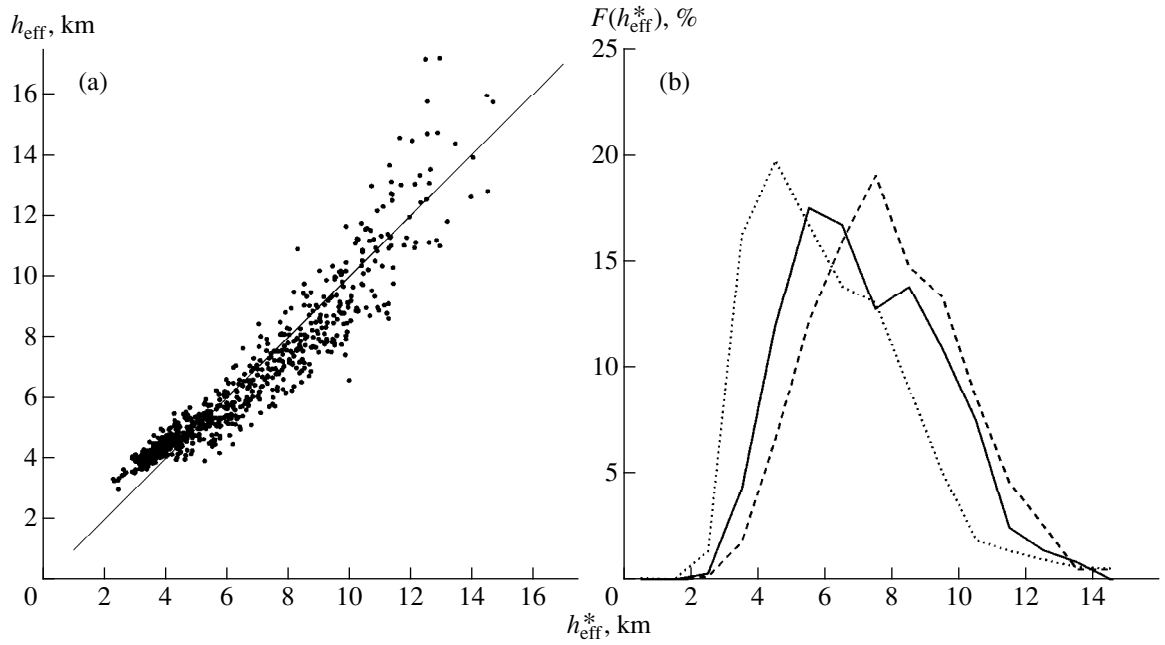

Fig. 6. (a) Relation between the altitudes h^*_{eff} calculated using formula (10b) and h_{eff} derived from the difference of the indices for 1.35- and 4.59-cm apertures using (11) and (8), from the data for seven selected nights. The line corresponding to coincidence of the altitudes is indicated. (b) Frequency distribution of the effective heights h^*_{eff} for three measurement seasons (summer 1998—solid curve; summer 1999—dotted curve; autumn 1999—dashed curve).

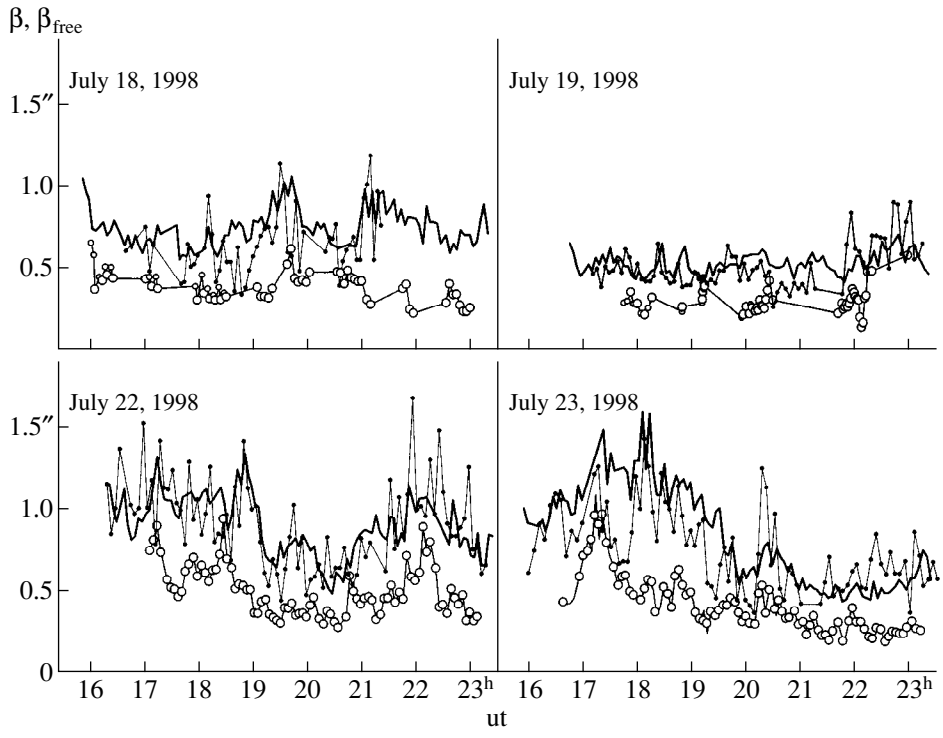

Fig. 7. Evolution of free-atmosphere contribution to seeing β_{free} (circles with curve) during the nights of July 18 and 19, 1998, for measurements with the DASS prototype, and during the nights of July 22 and 23, 1998, for measurements with the photometer. The β_{free} values for the photometer were calculated from the ratios $s^2_{6.91}/s^2_{1.35}$. For comparison, the total seeing β derived from GSM (curve) and DIMM (dots with curve) measurements is plotted.

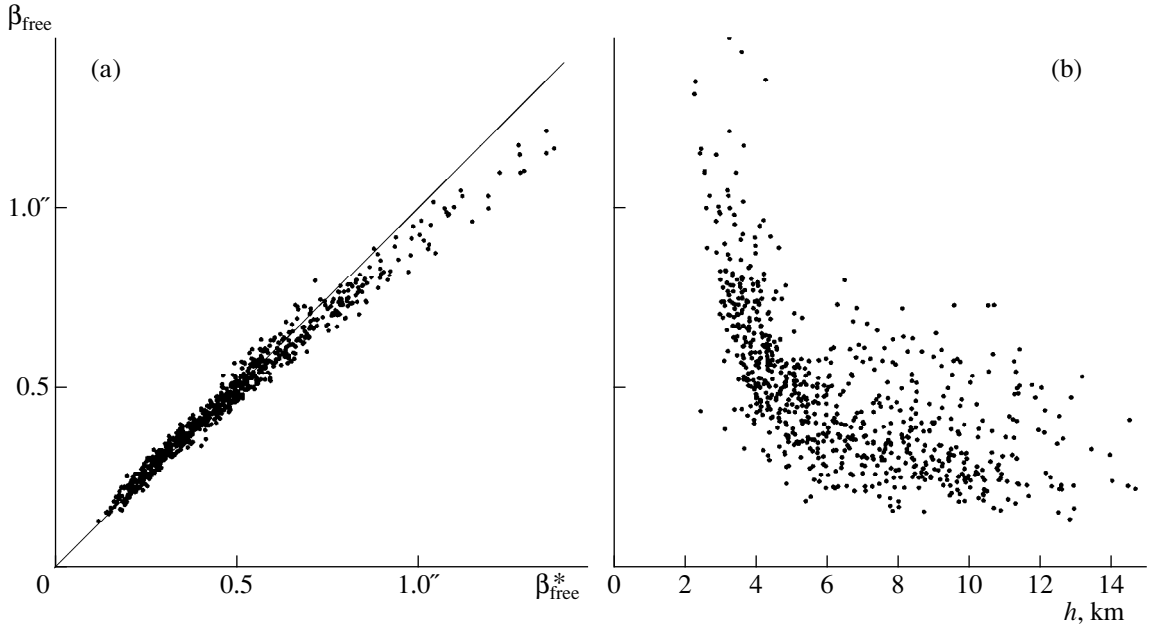

Fig. 8. (a) Comparison of β_{free} obtained from differences of the scintillation indices in apertures 1 and 3 and β^*_{free} derived from the effective height h^*_{eff} and (b) dependence of β_{free} on the effective height h^*_{eff} for seven selected nights. The curve $\beta^*_{free} = \beta_{free}$ is indicated.

errors are nearly proportional to β^*_{free} (for $\beta^*_{free} = 0\farcs3$, they are $\approx 0\farcs01$). For the β_{free} values derived from differences of the scintillation indices, another situation is realized. The absolute errors in this parameter are virtually independent of its value, and their median values are $0\farcs035$, $0\farcs022$, and $0\farcs019$ for the index differences (1–2), (1–3), and (1–4), respectively.

Figure 8a presents a comparison between β^*_{free} and β_{free}, calculated from the difference of the scintillation indices in apertures 1 and 3. We can see that the agreement is good for small values of β_{free}, while β_{free} is systematically less than β^*_{free} when $\beta_{free} > 0\farcs5$. This can be understood as a consequence of the fact that, as a rule, large values of β_{free} occur for low altitudes of the dominating turbulence (Fig. 8b), where the contribution of the turbulence in E_f is underestimated (see the weighting function for the pair 1–3 in Fig. 2a). When the pair 1–2 is used, the analogous relation indicates better average agreement; however, the scatter of the points is appreciably larger. The situation is opposite for the pair 1–4.

Table 7. Characteristics of cumulative distribution for β_{free} and R_{free}

Levels	Season 1	Season 2	Season 3	All measurements
$F(\beta_{free}) = 10\%$	$0\farcs29$	$0\farcs32$	$0\farcs22$	$0\farcs25$
$F(\beta_{free}) = 50\%$	0.43	0.49	0.34	0.39
$F(\beta_{free}) = 90\%$	0.68	0.87	0.52	0.72
$F(R_{free}) = 10\%$	0.26	0.29	0.19	0.22
$F(R_{free}) = 50\%$	0.41	0.45	0.34	0.38
$F(R_{free}) = 90\%$	0.74	0.67	0.50	0.58

We used the parameter β^*_{free} for statistical studies of the contribution of the free atmosphere to the total image distortion. Figure 9a presents individual cumulative distributions for three seasons together with the total cumulative distribution. Table 7 presents numerical levels for these distributions. The distributions for β_{free} (derived from the difference between apertures 1 and 3) differ only in the area of "poor" images, as follows from the above considerations.

The median value for β^*_{free} for all three seasons is $0\farcs39$. Comparing this value to the median seeing for Maĭdanak, which is $0\farcs70$ [3], indicates the relative contribution R_{free} of the free atmosphere to be 37%. This estimate can be refined using the simultaneously made DIMM measurements.

Since the scintillation and DIMM measurements were not synchronized, the instruments were located at different points of the Maĭdanak Observatory and different stars were used for each set of measurements; the hourly-averaged values of β^*_{free} and β were compared. Figure 9b presents distributions for R_{free}, and Table 7

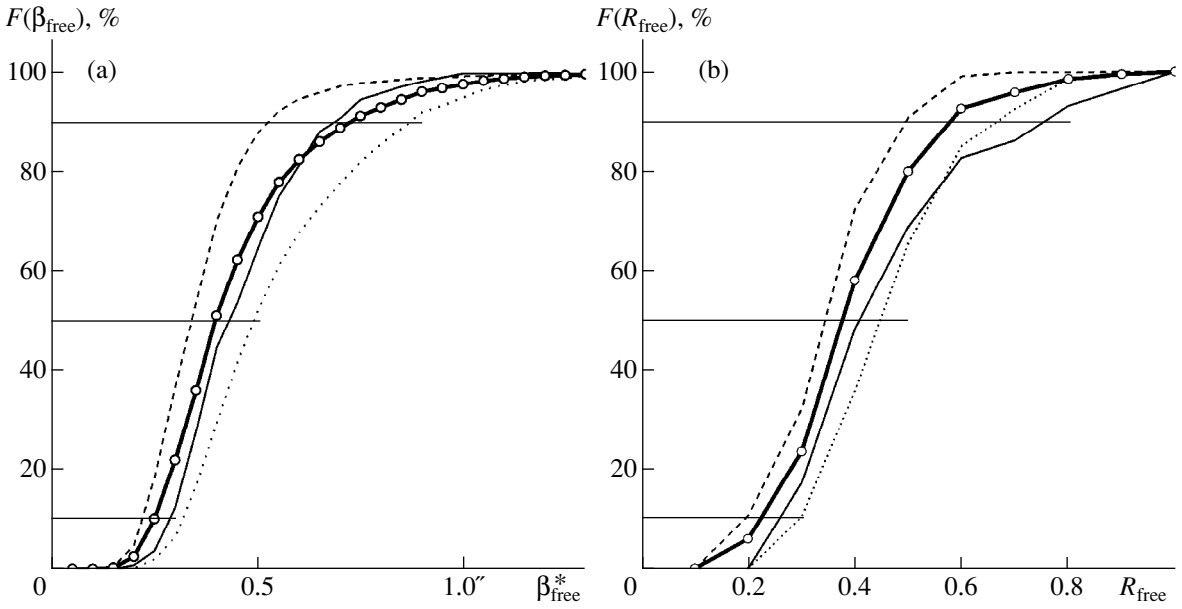

Fig. 9. Cumulative distributions $F(\beta)$ of (a) the free-atmosphere contribution to the image β^*_{free} and (b) the relative contribution R_{free} for three measurement season (summer 1998—solid curve; summer 1999—dotted curve; autumn 1999—dashed curve) and the total cumulative distribution (circles with thick curve). The 10, 50, and 90% levels are indicated.

the numerical parameters for these distributions. The median value for all the estimates is 38%. We can see that, in the best season (autumn 1999), the relative contribution of R_{free} is systematically smaller (34%), while the opposite is true in the worst season (summer 1999, 45%). This also provides evidence that the main reason for deterioration of the seeing is the state of the free atmosphere. Note also that the correlation between the integrated turbulence in the boundary layer E_b and that in the free atmosphere E_f estimated from the same data is relatively small, and equal to 0.3 to 0.5, depending on the season.

Our simplified model of the free atmosphere above Mt. Maĭdanak is based on two assumptions. In the case of minimum observed turbulence, all the free atmosphere is concentrated in the tropopause at a height of 10 km above the mountain (Fig. 6b). The intensity and altitude of this layer are constant. Increases in the integrated turbulence are due to the appearance of an additional layer at a height of 3 km. As noted above, this can clearly be seen when the effective heights and integrated turbulences for individual nights are compared. The fact that this layer is isolated from the turbulence boundary layer is confirmed by the low correlation between E_b and E_f estimated above.

The only free parameter in this model is the ratio of the integrated turbulence in the lower and upper layers E_L/E_H. The relations presented in Figs. 6a, 8a, and 8b, as well as the relation between the E_f values derived using (11) for aperture pairs (1–3) and (1–4), impose restrictions on the heights of both the upper and lower layers. The model dependences between β^*_{free}, β_{free}, h^*_{eff}, and h_{eff} are completely consistent with the observed relations plotted in the corresponding figures. The entire observed ranges of these values can be provided by variations of the free model parameter from 0 to ≈50 for $E_H = 10^{-13}$ m$^{1/3}$.

This simplified, mean-statistical model apparently reflects the regional role of the Pamirs massif, located to the east from Mt. Maĭdanak and having a characteristic height of about 6 km above sea level.

5. CONCLUSIONS

The first thing we would like to stress is the real possibility of determining supplementary integrated parameters describing turbulence in the free atmosphere (at altitudes from 1 to 20 km) on the basis of relatively simple measurements of stellar scintillations. These parameters include the isoplanatic angle θ_0, the effective height of the turbulence h_{eff}, and the integrated turbulence in the free atmosphere E_f or its contribution to the seeing β_{free}.

The most accurate values for these parameters can be derived using the differential-scintillation method. Full realization of the double-aperture scintillation sensor will undoubtedly make it possible to obtain much more information about turbulence in the Earth's atmosphere than is provided by the prototype we tested with these observations. However, an ordinary photoelectric photometer with the ability to detect fluxes on timescales of about 1 ms and at least two rapidly switching apertures is also able to provide fairly reliable data on

turbulence in the free atmosphere. The fact that even using only part of the data yielded a clear picture of the turbulence structure provides hope for a mathematically correct determination of the $C_n^2(h)$ profile via solution of the inverse problem.

Another important conclusion concerns the astroclimate of the Maĭdanak Observatory. This site features not only good median seeing, but also relatively weak turbulence in the free atmosphere, as indicated by its rather large median isoplanatic angle.

A comparison of the total seeing obtained using traditional methods and our estimates for the free atmosphere contribution to the seeing indicates that, as a rule, the contribution of the free atmosphere does not dominate. As is true of many other contemporary observatories, a considerable fraction of distortions (on average, around 60%) originates in the boundary layer immediately above the summit. However, the role of the free atmosphere increases when the images degrade. Periods of appreciable amplification of the turbulence in the free atmosphere can be reliably identified with the appearance of a low, intense, turbulent layer at a height of about 3 km.

ACKNOWLEDGMENTS

This study was partially supported by INTAS (grant INTAS-96-0367). We are grateful to our colleagues from the Sternberg Institute and Tashkent Astronomical Institute O. Vozyakova, S. Il'yasov, and T. Sadibekova, who carried out a substantial fraction of the observations, Yu. Tillaev and Kh. Sultanov, who kindly presented data from their DIMM observations; and A. Aliev, S. Ponomarenko, and A. Zaĭtsev, who helped with some technical problems.

REFERENCES

1. F. Martin, A. Tokovinin, A. Ziad, *et al.*, Astron. Astrophys. **336**, L49 (1998).
2. P. V. Shcheglov, *Problems in Optical Astronomy* [in Russian] (Nauka, Moscow, 1980).
3. S. P. Il'yasov, A. K. Baĭdzhumanov, M. Sarazin, *et al.*, Pis'ma Astron. Zh. **25**, 156 (1999) [Astron. Lett. **25**, 122 (1999)].
4. M. Sarazin, http://www.eso.org/gen-fac/pubs/astclim/paranal.
5. C. Munoz-Tunon, J. Vernin, and A. M. Varela, Astron. Astrophys., Suppl. Ser. **125**, 183 (1997).
6. A. Ziad, R. Conan, A. Tokovinin, *et al.*, Appl. Opt. (2000) (in press).
7. R. Avila, J. Vernin, and E. Masciadri, Appl. Opt. **36**, 7898 (1997).
8. F. Roddier, in *Progress in Optics*, Ed. by E. Wolf (North-Holland, Amsterdam, 1981), Vol. 19, p. 281.
9. V. I. Tatarskiĭ, *Wave Propagation in a Turbulent Medium* (Nauka, Moscow, 1967; McGraw-Hill, New York, 1961).
10. J. Krause-Polstroff, E. A. Murphy, and D. L. Walters, Appl. Opt. **32**, 4051 (1993).
11. D. L. Fried, J. Opt. Soc. Am. **72**, 52 (1982).
12. G. Loos and C. Hogge, Appl. Opt. **18**, 2654 (1979).
13. A. A. Tokovinin, Pis'ma Astron. Zh. **24**, 768 (1998) [Astron. Lett. **24**, 662 (1998)].
14. V. G. Kornilov and A. V. Krylov, Astron. Zh. **67**, 173 (1990) [Sov. Astron. **34**, 90 (1990)].
15. V. G. Kornilov, Balt. Astron. **7**, 513 (1998).
16. V. G. Kornilov and T. M. Pogrosheva, Astron. Zh. **66**, 424 (1989) [Sov. Astron. **33**, 213 (1989)].
17. A. Tokovinin, V. Kornilov, R. Conan, *et al.*, INTAS 96-0367 Progress Report, 1998, No. 1, Part II.
18. V. Kornilov, A. Tokovinin, O. Vozyakova, *et al.*, INTAS 96-0367 Final Report, 1999, No. 2, Part III.
19. D. G. Sandler, S. Stahl, J. R. P. Angel, *et al.*, J. Opt. Soc. Am. A **11**, 925 (1994).

Translated by K. Maslennikov

Astronomy Reports, Vol. 45, No. 5, 2001, pp. 409–414. Translated from Astronomicheskiĭ Zhurnal, Vol. 78, No. 5, 2001, pp. 474–480.

The Structure of the Photospheric Velocity Field near Hα Filaments

B. A. Ioshpa and V. N. Obridko

Institute of Terrestrial Magnetism, Ionosphere and Radio Propagation, Troitsk, Moscow region, 142190 Russia

Received July 21, 2000

Abstract—The velocity field of the plasma in the solar photosphere beneath chromospheric Hα filaments is studied. Observations were conducted in 1999–2000 using the magnetograph and tachometer of the tower telescope of the Institute of Terrestrial Magnetism, Ionosphere, and Radio Propagation, recently upgraded to improve both its sensitivity and spatial resolution. The results confirm that, as noted earlier, filaments are frequently found near velocity-inversion lines between regions of upward and downward motion of solar material, and lie predominantly above regions with upward motion of photospheric material. This tendency is characteristic of both the stable filaments of active regions and quiescent filaments far from active regions, though it is more distinct for the former case. The upward motion of photospheric material beneath filaments may play an important role in supporting the filaments against gravity. © *2001 MAIK "Nauka/Interperiodica"*.

1. INTRODUCTION

Studying the velocity fields near solar filaments can help our understanding of the origin and stability of filaments, as well as the associated mechanism of energy storage. Although filaments are situated in the corona—the upper portion of the solar atmosphere—lower layers can have a significant effect on their behavior. Since the density of photospheric material is much greater than that of both the corona and prominences, even weak photospheric movements should lead to effects in the corona that can influence the creation and destruction of filaments. For this reason, many recent works have been devoted to studies of the velocity fields in the vicinity of filaments. Detailed reviews can be found in [1], and also in [2–10]. However, primarily, only the velocities in the chromosphere beneath filaments (in the Hα line) or transition regions between the corona and prominences (in the CIV line) [1, 5, 10] have been studied. The photospheric velocity distribution was studied only in [3, 4] and [6–9]. The recent work of Magara and Kitai [11] examines transverse velocities in the photosphere beneath filaments using the technique of local correlation tracing proposed earlier.

Various investigations of the velocity field in the chromosphere beneath filaments have led to similar conclusions: filaments situated near a velocity-inversion line separating upward and downward motions of chromospheric material lie, as a rule, above regions of upward motion. On the contrary, studies of the velocity field in the photosphere have given rather contradictory results. Possible explanations for this include the lower velocities in the photosphere compared to the chromosphere, insufficient spatial resolution of the observations, and appreciable errors in radial-velocity measurements made with Babcock magnetographs (fluctuations of the wavelength in the exit slit of the spectrograph can give rise to errors of the order of 50–100 m/s).

In their study of photospheric velocities in the vicinity of a quiescent filament, Ioshpa *et al.* [6] showed that the distribution of upward and downward motions of the photospheric material was rather inhomogeneous compared to the chromospheric velocity distribution for the same filament [12]. However, the results of [6] were obtained using the radial-velocity channel of a solar magnetograph, and suffered from the errors indicated above. Subsequently, Ioshpa and Kulikova [2] determined the velocity fields beneath two quiescent filaments in an active region using a tachometer mounted on the tower telescope of the Institute of Terrestrial Magnetism, Ionosphere, and Radio Propagation (IZMIRAN), whose sensitivity and accuracy appreciably exceed those for the magnetograph radial-velocity channel. They concluded that the velocity distribution near these filaments was well-ordered and that stable portions of filaments were situated near a boundary between upward and downward motions.

After an upgrade of the instrument providing additional improvement in its spatial resolution and sensitivity, we obtained new measurements in June–August 1999 and June 2000, analyzed below.

2. INSTRUMENTS AND OBSERVATIONAL TECHNIQUES

We performed all measurements with the IZMIRAN tower telescope using a scanning Babcock longitudinal-field magnetograph and an integrating-interference spectrometer (tachometer) [13] operating simultaneously in two lines: the magnetograph in the Fe I λ5253 Å line (Landé factor $g = 1.25$) and the tachome-

1063-7729/01/4505-0409$21.00 © 2001 MAIK "Nauka/Interperiodica"

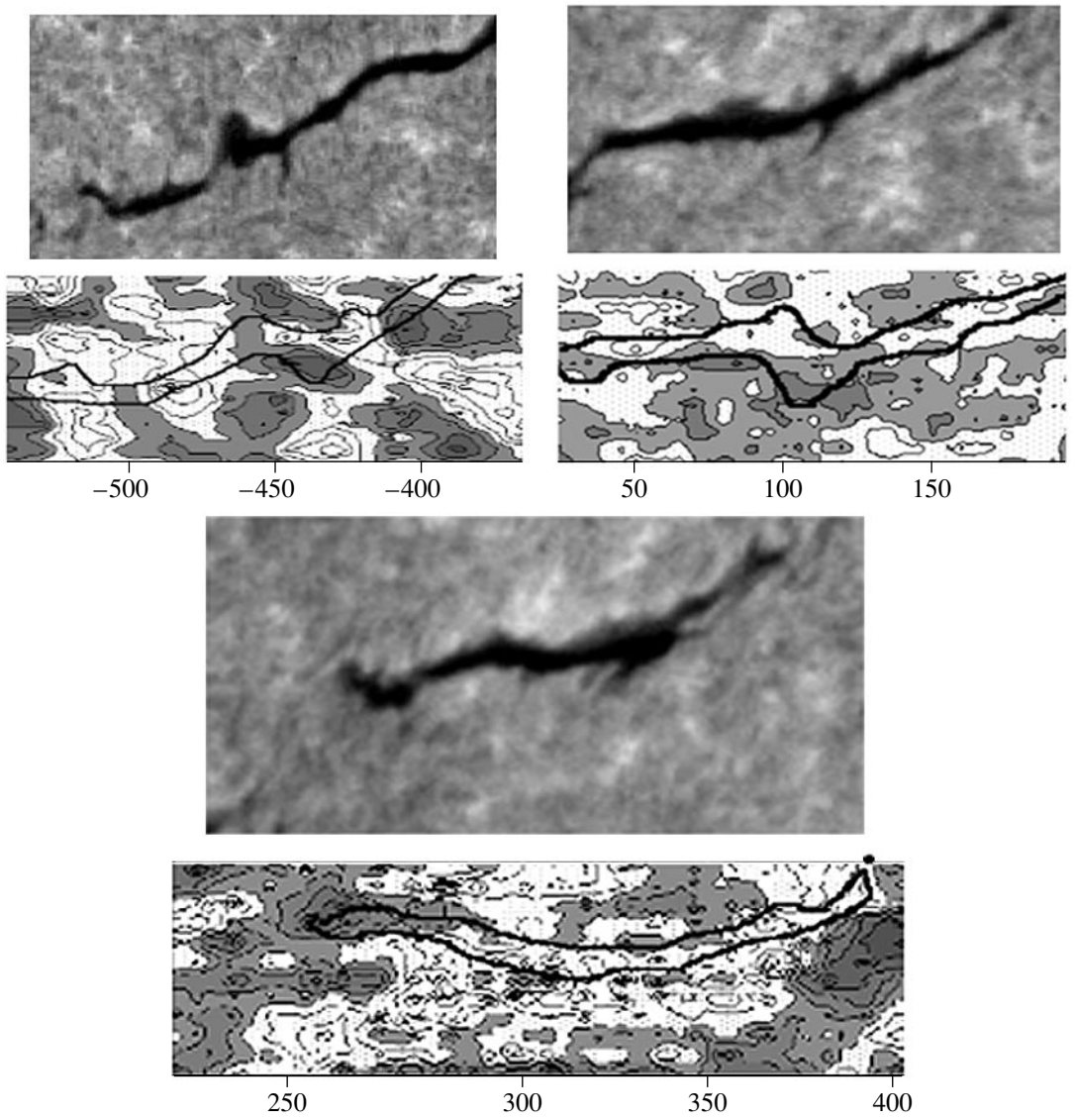

Fig. 1. The Hα filtergrams (courtesy of Big Bear Observatory) and velocity maps for the photosphere near the first filament on June 11, 13, and 14, 1999. The position of the filament is schematically shown by the bold contours in the velocity maps. The slight discrepancy between the Big Bear filtergrams and our drawn contour constructed from the light reflected from the spectrograph slit during the radial-velocity measurements is most likely due to the different quality of the images obtained in the different observations. The white areas with dots correspond to regions of upward motion. Dark areas show regions of downward motion. The velocity contours are drawn every 100 m/s (50 m/s for June 14). The scales (in angular seconds) are the same for both coordinates.

ter in the Fe I λ5576 Å line, which is not magnetoactive. The spectrometer is based on a Fabry–Perot interferometer stabilized by a quantum frequency standard. The spatial resolution of the observations was 4″–5″. We used the telescope's diffractional spectrograph operating in the second order with a linear dispersion of 0.9 Å/mm for preliminary filtering of the spectral lines. The sensitivity of the magnetic-field measurements was 5–10 G. The tachometer sensitivity for the radial-velocity measurements was about 10 m/s. Simultaneous with the radial-velocity and magnetic-field measurements, we obtained Hα filtergrams from light reflected from the mirror surface of the spectrograph entrance slit and passed through a Halley Hα filter. The data were recorded using a CCD camera. We used these measurements to find the relative position of the entrance slit with respect to objects on the solar surface, with the corresponding accuracy determined by the spatial resolution.

As noted in Section 1, our instrument has recently been subject to a series of modifications improving the quality of the measurements.

(1) We have developed a technique to compensate for jitter of the image of the solar disk, enabling the jitter to be decreased to 1″ [14].

(2) The erroneous Doppler shifts of spectral lines due to jitter of the spectrum in the spectrograph distort

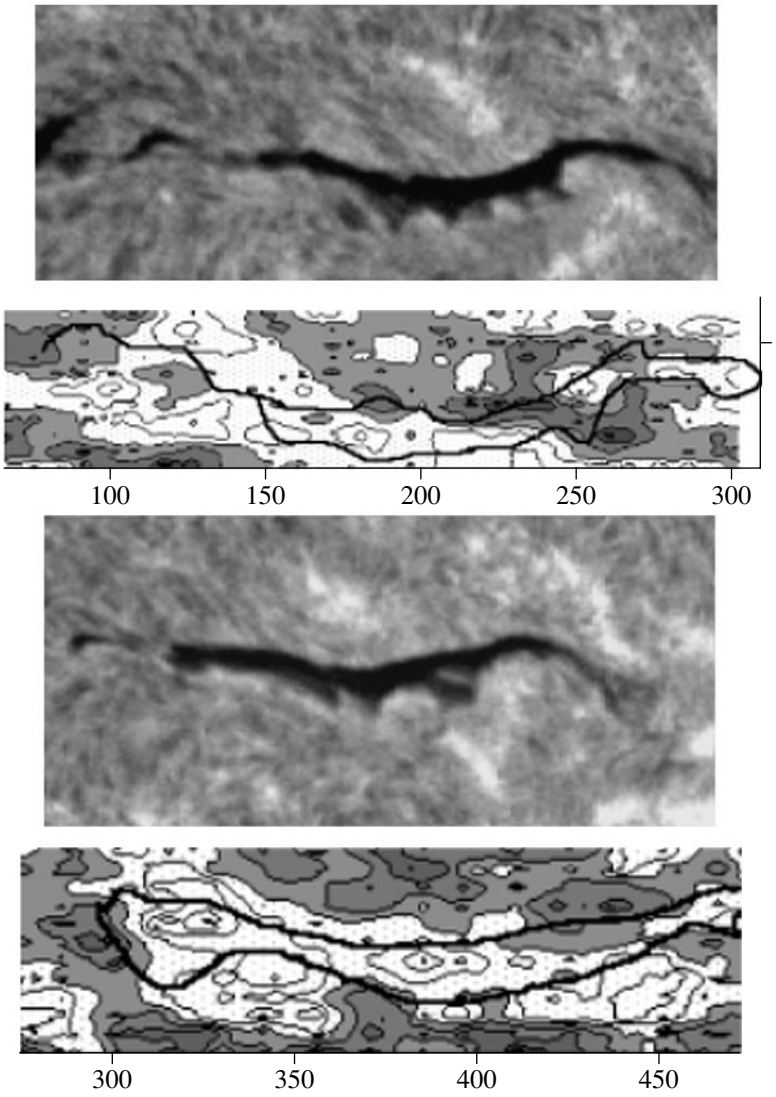

Fig. 2. Same as Fig. 1 for the second filament, of July 1 and 2, 1999.

the radial-velocity signal measured by the magnetograph; for the spectrograph of the IZMIRAN solar tower telescope, these shifts contributed about 100 m/s, comparable to the radial velocities in the photosphere. In 1998, we diminished these fluctuations of the spectral lines by an order of magnitude using interferometric methods [15]. This improved the accuracy of the scanning magnetograph's velocity measurements by an order of magnitude, bringing it to the accuracy of the tachometer (10 m/s). Our calculations show that the heights of formation of both spectral lines studied differ by no more than by 100 km. Therefore, the observed similarity of the radial-velocity distributions obtained simultaneously for the two different spectral lines and two different instruments lends additional confidence in the results.

(3) Similar to previous observations, we obtain maps of the magnetic fields and radial velocities by scanning the region in question. In previous observations, to diminish the effect of the five-minute oscillations, we used a scanning rate and interval providing a temporal shift of about 150 s between scans [2]. We constructed the maps via a sliding average of adjacent scans, which halved the spatial resolution. In our 1999–2000 observations, we used another scanning technique. Every 150 s, the solar image at the spectrograph entrance slit is reset to the initial point and the measurement cycle repeated [16]. Thus, the measured parameters are fixed twice at every point with an interval of 150 s. Using this method, we avoid a decrease in spatial resolution (of course, at the expense of temporal resolution). The time required for complete construction of one map is doubled, and is about 25–30 min. We eliminate a possible instrumental trend using an analogous procedure. We assume the velocity averaged over the entire data array is zero radial velocity.

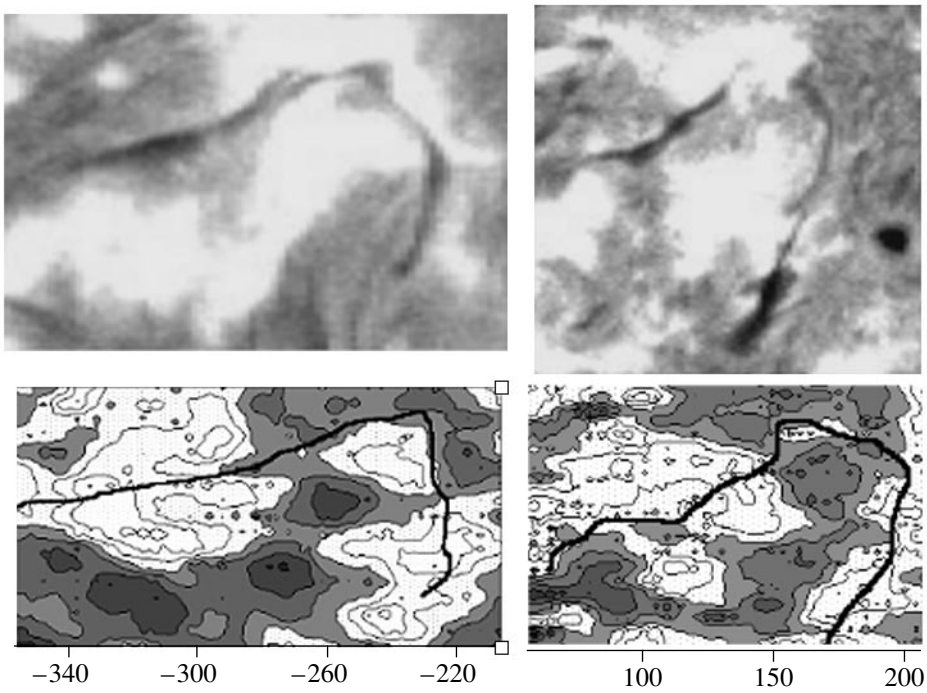

Fig. 3. Same as Fig. 1 for the third filament, of June 24 and 26, 1999.

3. OBSERVATIONS AND DATA ANALYSIS

We present here the photospheric velocities around four filaments observed in 1999 and 2000. Two filaments were situated in old flocculus regions, whereas two others were near active regions with high sunspot activity.

The first filament (of the two in old flocculus regions) extended for nearly 400″ at a small angle to latitude 25° S. We studied the photospheric magnetic and velocity fields beneath this filament during six days, from June 11 to 16, 1999. Figure 1 presents Hα filtergrams (obtained at the Big Bear Observatory and retrieved via the Internet) and velocity maps for June 11, 13, and 14, 1999. The position of the filament derived from the filtergrams obtained simultaneously by us is shown schematically on the velocity maps. We have drawn contours of the radial velocity every 50 m/s. The white areas with dots show regions of upward motion, whereas dark areas show regions of downward motion of solar material. The longitude of the middle portion of the filament on June 11, 1999 was about 30° E. We can see that most of the filament was situated above regions of upward motion. At the same time, the so-called feet of the filament and its eastern end were directed toward regions of downward motion, and are nearly adjacent to them. On June 13, 1999, the same filament was situated above a narrow region of upward motion of solar material forming a corridor surrounded on both sides by downward motion. The eastern portion of the filament disappeared on June 14, 1999 (unfortunately, we did not obtain any velocity maps for this event), while the western portion was still above the region of upward motion, near the radial-velocity inversion line. Similar behavior was observed over the next two days.

The second filament was also situated in a flocculus field and was strongly elongated along 25° N. We observed it during several days, from June 29 to July 3, 1999. The middle portion of the filament was situated near the central meridian on July 1, 1999. Figure 2 shows the Big Bear Observatory Hα filtergrams and the velocity maps for July 1 and 2, 1999. We can see that the tendency noted above is also characteristic of this filament. Namely, most of the filament is above a region of upward motion of photospheric material, while its feet and ends are either above or near regions of downward motion. For example, the narrow eastern portion of the filament is above a region of upward motion, while its flocculent western portion with multiple feet is near a region of downward motion.

The third filament was located to the west of the active region AR 8598 (23° N). This filament had the form of an arch, with active processes periodically destroying its peak. The branches of the arch were relatively stable over all the days of observations (June 24, 26–28, 1999). The behavior of the magnetic field and radial velocities was also stable during our observations: the branches of the arch were situated above regions of upward motion in the photosphere, while its peak was in a region of downward motion (Fig. 3).

We observed the fourth filament on July 13–14, 2000 in the active region AR 9043 (25° N). This filament also had the form of an arch stretched in the east–

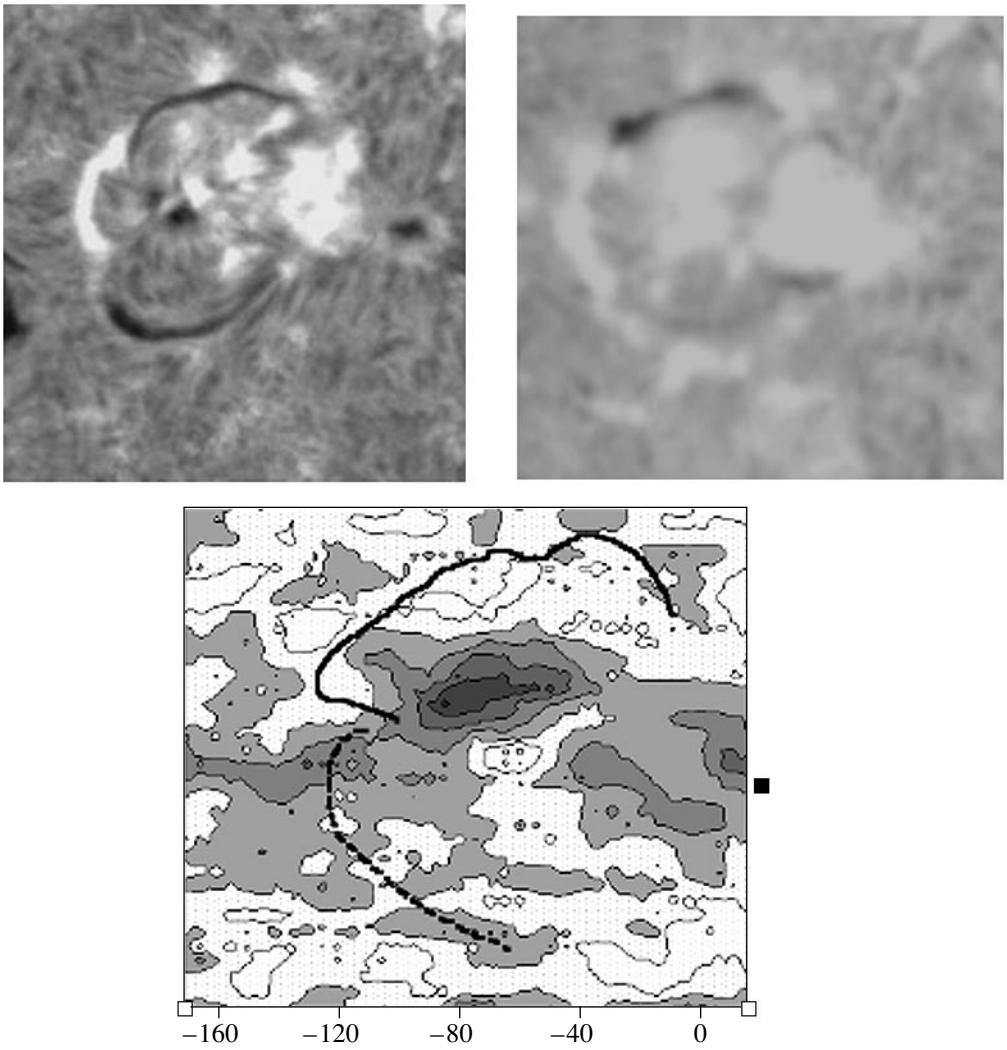

Fig. 4. Same as Fig. 1 for the fourth filament, of June 14, 2000.

west direction. As in the previous case, the peak of the arch was above a flocculus, and was not visible in the Hα filtergram due to active processes. In addition, only the upper (northern) branch of the arch was stable, whereas the lower (southern) branch alternately appeared and disappeared. Figure 4 presents the two Hα filtergrams and velocity maps for June 14, 2000, when the filament was near the central solar meridian. The stable northern branch was above a region of upward motion of photospheric material, while the peak and part of the unstable lower (southern) branch were above a region of downward motion.

4. CONCLUSIONS

Analysis of the observations discussed above, as well as those presented earlier in [2], leads to the following conclusions.

(1) Both the structure of the photospheric magnetic field (which is well known) and the structure of the velocity field are closely related to the position and structure of Hα filaments.

(2) The filaments tend to be situated above regions of upward motion of photospheric material, sometimes close to a radial-velocity inversion line. This tendency is characteristic of both the relatively stable filaments of active regions and quiescent filaments in old flocculus regions, though it is more distinct for active-region filaments. It can be manifest less clearly for quiescent old filaments, due to the presence of a large number of feet, which presumably connect the filament with lower layers of the solar atmosphere [17]. As a rule, these feet are situated above or near regions of downward motion of photospheric material. In addition, the ends of filaments are frequently situated in regions of downward motion of photospheric material.

(3) Filaments are frequently situated above "corridors" of upward motion, which are sometimes rather narrow (see the velocity maps for June 13 and 14, 1999), with downward motion on either side.

(4) The flow of photospheric material in the flocculi surrounding a filament is directed downward, in accordance with [18].

Our findings are similar to those obtained in studies of chromospheric velocities (the Hα line) and velocities in the transition region between a filament and the corona (CIV line) [5, 10]. This may indicate a flow of material moving from the photosphere to the chromosphere and then to the corona. If this is indeed the case, this raises the question of the role of this photospheric flow in the replenishment of prominence material.

In addition, the existence of this flow may be an important factor in supporting the filaments against gravity. Note that the presence of photospheric transverse motions directed toward a filament from both sides (a convergence of material beneath the filament) was demonstrated in [19].

ACKNOWLEDGMENT

This work was supported by the Russian Foundation for Basic Research (project code 98-02-17128a).

REFERENCES

1. B. Schmieder, in *Dynamics and Structure of Quiescent Solar Prominences*, Ed. by E. R. Priest (Kluwer, Dordrecht, 1989), Vol. 150, p. 15.
2. B. A. Ioshpa and E. Kh. Kulikova, Astron. Zh. **72**, 932 (1995) [Astron. Rep. **39**, 833 (1995)].
3. M.-J. Martres, J. Rayrole, and I. Soru-Escaut, Sol. Phys. **46**, 137 (1976).
4. M.-J. Martres, P. Mein, B. Schmieder, and I. Soru-Escaut, Sol. Phys. **69**, 301 (1981).
5. O. Engvold, E. Tandberg-Hanssen, and E. Reichman, Sol. Phys. **96**, 35 (1985).
6. B. A. Ioshpa, I. E. Kozhevatov, E. Kh. Kulikova, and É. I. Mogilevskiĭ, Soln. Dannye **5**, 68 (1986).
7. B. A. Ioshpa and E. Kh. Kulikova, *Physics of Solar Activity* [in Russian] (Nauka, Moscow, 1988), p. 168.
8. B. Ioshpa, I. Kogevatov, and E. Kulikova, in *Solar Polarimetry* (Sac. Peak Observatory, Sunspot, 1991), p. 280.
9. B. Ioshpa and E. Kulikova, in *Solar Magnetic Fields*, Ed. by M. Schuessler and W. Schmidt (Cambridge Univ. Press, Cambridge, 1994), p. 378.
10. T. A. Kucera, G. Aulanier, B. Schmieder, *et al.*, Sol. Phys. **186**, 259 (1999).
11. T. Magara and R. Kitai, Astrophys. J. **524**, 469 (1999).
12. V. Utrobin and N. Shilova, Soln. Dannye **4**, 75 (1985).
13. B. Ioshpa and I. Kogevatov, in *Solar Polarimetry* (Sac. Peak Observatory, Sunspot, 1991), p. 59.
14. I. E. Kozhevatov *et al.*, Prib. Tekh. Éksp., No. 1, 125 (2000).
15. B. A. Ioshpa, I. E. Kozhevatov, and E. Kh. Kulikova, in *Proceedings of an International Scientific Conference on Solar Physics Dedicated to the Memory of G. M. Nikol'skiĭ*, 1999, p. 253.
16. I. E. Kozhevatov *et al.*, Prib. Tekh. Éksp., No. 1, 120 (2000).
17. J. Kubota and A. Uesugi, Publ. Astron. Soc. Jpn. **38**, 903 (1986).
18. V. M. Grigor'ev and V. E. Stepanov, Issled. Geomagn., Aéron. Fiz. Solntsa **2**, 77 (1971).
19. S. F. Martin, S. H. B. Livi, and J. Wang, Aust. J. Phys. **38**, 929 (1985).

Translated by V. Badin